In situ Characterization of Phase Evolution in LiFePO$_4$

Von der Fakultät Chemie der Universität Stuttgart

zur Erlangung der Würde eines

Doktors der Naturwissenschaften (Dr. rer. nat.)

genehmigte Abhandlung

Vorgelegt von

Nils Ohmer

aus Cuxhaven

Hauptberichter:	Prof. Dr. Joachim Maier
Mitberichter:	Prof. Dr. Guido Schmitz
Prüfungsvorsitzender:	Prof. Dr. Rainer Niewa

Tag der Einreichung: 11.06.2015

Tag der mündlichen Prüfung: 24.09.2015

Besonderer Dank gilt
meiner Frau Kathrin
und meinen Eltern.

Ein neuer Land in neuer Zeit,
wo Geist verweilt in Ewigkeit,
wo Herz ist Ruf und Handeln weise,
da führ' mich hin auf meiner Reise.

Erklärung

Die vorliegende Doktorarbeit wurde vom Autor selbst in der Abteilung von Prof. J. Maier am Max-Planck-Institut für Festkörperforschung, im Zeitraum von April 2010 bis Juni 2015 angefertigt. Der Inhalt ist die eigene Arbeit des Autors, Ausnahmen sind gekennzeichnet, und wurde noch nicht zur Erlangung einer Qualifizierung oder eines Titels an einer akademischen Institution eingereicht.

Stuttgart, 10. Juni 2015   Nils Ohmer

Declaration

The work described in this thesis was carried out by the author in the Department of Prof. J. Maier at the Max Planck Institute for Solid State Research from April 2010 to June 2015. The contents are the original work of the author except where indicated otherwise and have not been previously submitted for any other degree or qualification at any academic institution.

Stuttgart, June 10, 2015   Nils Ohmer

Content

Kurzfassung

Eines der wichtigsten und am häufigsten untersuchten Elektrodenmaterialien für zukünftige Lithium-basierte Batterien ist $LiFePO_4$ (LFP), welches im Rahmen der Delithiierung eine Phasentransformation hin zu $FePO_4$ (FP) vollzieht. Trotz des hohen wissenschaftlichen und praktischen Interesses an dem Material ist noch immer eine intensive Diskussion über den genauen Mechanismus und die zugrunde liegenden Einflussfaktoren dieser Phasentransformation im Gange.

Im Rahmen dieser Arbeit sind erste Untersuchungen *ex situ* an elektrochemisch zyklisierten Elektroden, bestehend aus einem LFP Pulver, Kohlenstoff coating und einem Binder, so wie sie in ihrem prinzipiellen Aufbau auch bereits kommerzielle Verbreitung finden, mit einer Kombination aus örtlich hochauflösenden Methoden (Hochauflösende Transmissionselektronenmikroskopie und Elektro-nenenenergieverlustspektroskopie) und mit über einen großen Bereich integrierenden Messtechniken (Röntgenbeugung und Röntgen-Nahkanten-Absorptions-Spektroskopie), bei unterschiedlichen Ladungszuständen vorgenommen worden. Die Kombination dieser verschiedenen Charakterisierungstechniken erlaubt es, zwischen dem Zyklisierungsverhalten unterschiedlich großer Kristallite innerhalb der gleichen Elektrode zu unterscheiden. Für unter hydrothermalen Bedingungen hergestelltes LFP-Kathodenmaterial stellt sich heraus, dass ein partikelgrößenabhängiges Zyklisierungsverhalten existiert, bei welchem nanoskalige Partikel anscheinend nicht am Ladevorgang teilnehmen. Innerhalb dieser kleinen Partikel wurde eine turbostratische Stapelung von Schichten gefunden und als Ursache für den verminderten Lithiumaustausch identifiziert. Diese höherdimensionalen Defekte in den nanoskaligen Partikeln hindern diese daran am Ladevorgang teilzunehmen indem sie die Lithiumdiffusion entlang der 1-dimensionalen Kanäle stören, sowie den Trans-

port entlang der anderen Richtungen des LFP Gitters verschlechtern und damit den Lithiumtransport blockieren, was zu einer Verminderung der elektrochemisch zugänglichen Kapazität führt.

Um den Mechanismus des Lithiumaustausches einer LFP-Dünnschichtkathode während des Ladevorganges zu untersuchen, ist eine Dünnschichtbatterie spezieller Bauweise entwickelt und mittels gepulster Laserdeposition und thermischen Verdampfungstechniken hergestellt worden. Mit Hilfe von Schattenmasken wurden Dünnschichten der LFP Kathode, des Li_2O-V_2O_5-SiO_2 (LVSO) Elektrolyten und der LiAl Anode nacheinander abgeschieden, so dass der Lithiumtransportweg innerhalb der entstehenden Batterie entlang der Substratoberfläche der röntgentransparenten Si_3N_4 Membran verläuft. Die entstandene Anordnung ermöglicht die Nutzung von Synchrotron-basierter energieaufgelöster Rastertransmissionsröntgenmikroskopie mit entsprechend hoher chemischer und örtlicher Auflösung, zur Durchführung von *in situ* Röntgenabsorptionsmessungen an der Eisen L_3 Kante. Eine Verschiebung des vornehmlichen Absorptionscharakteristikums von 708 auf etwa 710 eV während der Delithiierung wird genutzt, um die Änderung des lokalen Ladezustands bzw. des Verhältnisses von Fe^{2+} (lithiiert) zu Fe^{3+} (delithiiert) zu beobachten. Auf diese Weise wird der anfängliche Lithiierungsprozess einer LFP Dünnschichtkathode mittels *in situ* Rastertransmissionsröntgenmikroskopie und einer lateralen Auflösung von 30 nm, verfolgt. Der beobachtete Lithiierungsmechanismus entspricht nicht dem klassischen Mechanismus bei welchem ein Teilchen nach dem anderen lithiiert wird, so wie es für Vielteilchen LFP Kathodenmaterialien typisch ist, sondern stattdessen findet die Lithiierung des Dünnschichtkathodenmaterials weitestgehend gleichzeitig statt. Der Grund für den im Vergleich zur Vielteilchen-Pulverelektrode veränderten Lithiierungsmechanismus liegt in mechanischen Wechselwirkungen innerhalb der Dünnschicht während der Lithiierung, d.h. in der entsprechenden Volumenausdehnung und Bildung von neuen Hochenergiegrenzflächen, welche letztendlich die Form des Einteilchen chemischen Potentials dahingehend verändert, dass ein monotoner Verlauf entsteht. Das hat weitreichende Konsequenzen: so wandelt sich nicht nur der Vielteilchen-Mechanismus hin zu einer gleichzeitigen Lithiierung, sondern auch der Einteilchen-Mechanismus ändert sich von einem 2-Phasen- zu einem 1-Phasen-Mechanismus während der Lithiierung.

Desweiteren wird das Verschwinden der Hysterese-Schleife, sowie des Memory-Effektes vorhergesagt. Diese Ergebnisse sind von allgemeingültiger Natur und anwendbar auf alle Dünnschichten phasenseparierender Interkalationsmaterialien welche einer Volumenänderung während des Lithiumaustausches unterliegen.

Um die Lücke in der Literatur bezüglich *in-situ*-Beobachtungen der Phasentransformation in einzelnen (L)FP Partikeln mit guter räumlicher und zeitlicher Auflösung zu schließen, wurde eine Mikrometer-kleine Dünnschichtbatterie mit einem orientierten LFP Einkristall definierter Defektchemie als Kathodenmaterial und Abmessungen von 16x1x0.2 µm gebaut. Mittels Rastertransmissionsröntgenmikroskopie wird die Phasentransformation entlang der schnellen (010) Richtung im Mikrometerbereich mit einer räumlichen Auflösung von 30 nm und einer zeitlichen Auflösung von einigen Minuten während der elektrochemischen (De)lithiierung *in situ* verfolgt. Desweiteren sind diese Rastertransmissionsröntgenmikroskopie-Messungen einige der wenigen Untersuchungen, die je an einem LFP Material mit definierter Defektchemie vorgenommen worden sind, obwohl diese für ein allumfassendes Verständnis des Materialverhaltens unerlässlich ist. Diese Messungen offenbaren nicht nur den Mechanismus der Phasentransformation innerhalb eines einzelnen Partikels, sondern auch die Bedeutung elastischer Effekte auf den (De)lithiierungsprozess. Es wird gezeigt, dass die Startposition der Phasentransformation durch den konkret vorliegenden defektchemischen Zustand bestimmt ist, während das Phasenwachstum sowohl von LFP, als auch von FP von elastischen Effekten dominiert wird.

Abstract

Among the candidates for electrodes in future Li-based batteries, $LiFePO_4$ (LFP) is one of the most important and most frequently studied materials, undergoing a phase transformation upon delithiation to $FePO_4$ (FP). In spite of the great scientific and practical interest in this material, there is still an extensive debate on the mechanism of this phase transformation and the underlying factors of influence.

Within the framework of this thesis, first studies are carried out *ex situ* on multi-particle, full electrode LFP materials, being electrochemically cycled and analyzed at various states of charge by a combination of highly spatially resolved methods (high-resolution transmission electron microscopy and electron energy loss spectroscopy (HRTEM, EELS)) and integral measurement techniques (analyzing the X-ray diffraction and X-ray absorption near edge structure (XRD, XANES)). This combination of characterization techniques allows one to distinguish between the cycling behaviour of differently sized crystallites within the same electrode. It is found that for electrodes with hydrothermally grown LFP as active material, a particle size dependent cycling behaviour exists, with nanosized particles apparently not participating in the charging process at all. A turbostratic stacking of layers in these nanosized particles is found and identified to be responsible for sluggish lithium insertion and extraction. These higher dimensional defects prevent the small particles from participating in the charging process, most likely by disturbing the lithium diffusion along the 1-dimensional channels, as well as impair the transport along the other directions in the LFP host structure and thus blocking the lithium transport, resulting in a comparibly lower practical capacity during electrochemical cycling.

To study the lithium exchange mechanism upon charging a LFP thin film cathode, an

all-solid-state thin film battery cell with a lateral design concept is developed and realized by pulsed laser deposition (PLD) and thermal evaporation techniques. Using PLD and shadow masks LFP cathode, Li_2O-V_2O_5-SiO_2 (LVSO) electrolyte and LiAl anode thin films are deposited sequentially in a way that the Li transport pathway in the resulting battery is along the X-ray transparent commercial Si_3N_4 membrane substrate. This enables the usability of synchrotron-based energy resolved scanning transmission X-ray microscopy (STXM) with its high chemical and spatial resolution to perform *in situ* absorption measurements at the Fe L_3 edge. Upon delithiation, a shift in the main absorption feature from 708 to 710 eV is used to fingerprint the change in the local state of charge, identifying areas containing Fe^{2+} (lithiated) and Fe^{3+} (delithiated), respectively. The initial lithiation process of a LFP thin film cathode material has been followed by *in situ* STXM, with a lateral resolution of 30 nm, during electrochemical charging of the thin film battery. The observed initial lithiation process does not follow the classical particle by particle mechanism, typical for multi-particle LFP cathodes, but instead a rather simultaneous, although inhomogeneous, lithiation is observed. The reason for this change in mechanism, compared to multi-particle powder electrodes, is found in mechanical interactions within the thin film upon lithiation, i.e. in the corresponding volume expansion and formation of high energy surfaces, changing the shape of the single-particle chemical potential to a monotone form upon lithiation. This has far-reaching consequences: not only the many-particle mechanism is changed to a concurrent lithiation, but also the single-particle mechanism is changed from a two-phase to a single-phase mechanism upon lithiation. Furthermore, a vanishing hysteresis loop and the disappearing of the memory effect is predicted. These findings are rather general and applicable to all kind of thin films of phase separating intercalation materials, undergoing a volume change upon lithium exchange.

To fill the gap in literature on *in situ* observations of the (L)FP phase evolution on a single-particle level with appreciable space and time resolution, a micrometer-sized all-solid-state thin film battery is built with a defect-chemically well characterized LFP single crystal as cathode material with dimensions of 16x1x0.2 µm. Using STXM, the phase evolution along the fast (010) orientation is followed during *in situ* electrochemical (de)lithiation on a micro-meter scale with a lateral resolution of 30 nm and with

minutes of time resolution. Furthermore, the STXM measurements performed on this sample are one of the few experiments ever taken on LFP materials with a well defined defect chemistry, even though fundamentally necessary for an overall understanding of the materials behaviour. This combination discloses not only the mechanism of LFP transformation on a single-particle level, but also the significance of elastic effects on the (de)lithiation process. Using a defect chemical analysis, the position of phase formation is found to be determined by the defect chemical situation, while the growth pattern of both LFP and FP is found to be dominated by elastic effects.

Chapter 1

Introduction

This work deals with the mechanism of lithium extraction and insertion in $LiFePO_4$ (LFP), a promising cathode material for lithium ion batteries (LIB), with a special focus on *in situ* characterizing the phase evolution using scanning transmission X-ray microscopy (STXM). Three different LFP systems, going from a multi-particle to a single-particle level, are studied within the framework of this thesis. First, cathodes with LFP powder as active material are investigated *ex situ* using i.a. electron energy loss spectroscopy (EELS) and X-ray absorption spectroscopy (XAS) (chapter 3). Secondly, thin films of $LiFePO_4$ are analyzed *in situ* as part of an all-solid-state thin film battery using STXM (chapter 4). Thirdly, the (de)lithiation of single crystalline $LiFePO_4$ as cathode material in a micrometer-sized battery is followed *in situ* by STXM (chapter 5). Before the obtained results will be discussed, some general remarks on LIBs and a summary of some of the main characteristics and features of $LiFePO_4$ as a cathode material are given in this chapter, followed by a short introduction to the main methods and techniques used throughout this thesis (chapter 2).

1.1 General Remarks

Battery research is essentially a multi-disciplinary field, connecting on a fundamental level physical, chemical and materials research, while in the area of application engineering and system integration prevail. Rechargeable batteries are the only devices which can directly and reversibly convert electrical into chemical energy. Due to the

connected efficiency of energy conversion and their ability to store energy, batteries are of paramount interest for an energy-dependent technological society as ours.

1.1.1 Historical survey

Batteries have become well-known energy conversion and storage devices since Alessandro Volta has reported "On the electricity excited by the mere contact of conducting substances of different kinds", introducing his electric pile in a letter to Joseph Banks already on march 20th 1800, published in the Philosophical Transactions of the Royal Society of London [1]. 59 years later, in 1859, the first rechargeable battery, the lead-acid battery, has been invented by Gaston Planté [2]. But it took nearly another 120 years until M.S. Whittingham, first proposed the concept of a lithium-based battery, using $LiTiS_2$ as cathode and lithium metal as anode in 1976 [3]. Encouraged by the work of Goodenough et al., demonstrating a lithium battery with $LiCoO_2$ (LCO) as cathode material [4, 5], and Yazami et al., reporting on the electrochemical intercalation of lithium in graphite [6], circumventing the savety problems connected with the use of metallic lithium as anode [7], SONY released the first commercial LIB in 1991. This battery system, using $LiCoO_2$ as positive and graphite as negative electrode proved successful and since then, lithium ion batteries have been of ever growing importance as one of the key devices for consumer electronics, electro mobility and net-integrated storage of fluctuating renewable energies.

1.1.2 Battery components

The overall properties of a battery, such as capacity, energy density, power density, cycle stability, voltage stability, rate performance and safety, are determined by the properties and the interplay of the electrochemical active components (electrodes and electrolyte). The main reason for the success of LIBs is their favorable energy and power density compared to other battery techniques, as illustrated in figure 1.1, combined with a high cycling stability. These superior properties originate from lithium fortunately being at the same time the lightest and one of the most electropositive metal elements of the periodic table, which can easily be accommodated in and migrate through various crystal structures.
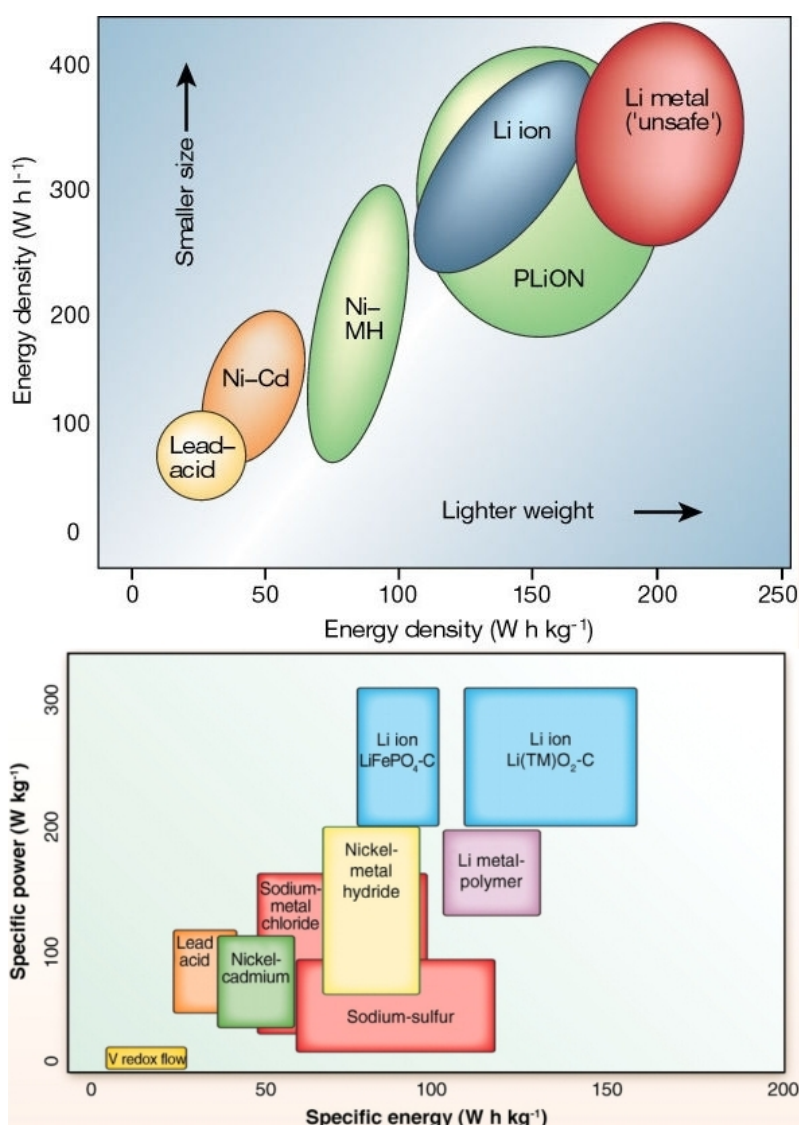
Figure 1.1: Power and energy densities for different rechargeable battery technologies. Top: volumetric vs. gravimetric energy density (taken from [8]). Bottom: gravimetric power vs. gravimetric energy density (taken from [9]).

Numerous electrode materials for LIBs are currently studied and their morphology [10, 11, 12], particle size [13, 14, 15] and defect chemistry [16, 17, 18] is analyzed and modified to understand and enhance their electrochemical properties. The most common anode materials are carbon materials, especially graphite [19]. But also the spinel $Li_4Ti_5O_{12}$ [20], as well as materials such as Sn and Si are under serious consideration as anode materials and already partly commercialized (among others Sn is used in Sony's Nexelion anode material [21]). Typical cathode materials comprise layered lithium transition metal oxides (e.g. LCO [5], $LiNi_yMn_yCo_{1-2y}O_2$ (NMC) [22]), spinels

(e.g. LiMn$_2$O$_4$ [23]), and olivine-type lithium transition-metal phosphates (e.g. LFP [24]). All cathode materials for LIBs have in common, that their theoretical capacity is relatively low in comparison to most of the studied anode materials, while the later ones have generally a lower cycle stability, due to the formation of a pronounced solid-electrolyte-interphase (SEI) and volumetric changes upon lithium insertion and extraction. Therefore, a lot of research effort is directed to these two fields.

Electrolytes are normally made of a solution of a lithium salt (e.g. LiPF$_6$) in a non-aqueous mixed organic solvent (e.g. ethylene carbonate - dimethyl carbonate (EC-DMC)) [25], whereat different soluble electrolyte additives [26] and non-soluble additives [27] are under investigation and research is carried out on polymer electrolytes [28] as well as ionic liquid based electrolytes [29]. Besides these three major electrochemical active battery components, the separator, a porous membrane soaked with electrolyte and positioned between the electrodes, allowing ionic flow but preventing a direct contact between the electrodes and electrical short circuiting, respectively, is of importance and has to be adjusted to the batteries' chemistry and geometry [30]. In addition to the cited references, nice overviews over different cathode, anode and electrolyte materials under investigation are given in [31, 32, 33, 34].

1.1.3   Working principle

In equilibrium state the cell voltage of a LIB is determined by the difference in the chemical potential of Lithium in the cathode $\mu_{Li}(c)$ and in the anode $\mu_{Li}(a)$ and holds

$$\mu_{Li}(c) - \mu_{Li}(a) = -nEF = \Delta_r G \ , \tag{1.1}$$

where n is the number of electrons per mole transferred in the reaction, E the cell voltage in thermodynamic equilibrium (also called electromotive force (emf) or open circuit voltage (OCV)), F the Faraday constant (96485.3 C/mol) and $\Delta_r G$ the Gibbs free energy of the reaction. If a charged LIB is connected to a load, Lithium ions are, according to equation 1.1, shuttled from the anode (electrode of higher lithium chemical potential) through the electrolyte to the cathode (electrode of lower lithium chemical

potential), while electrons are simultaneously pushed through the external circuit from the anode to the cathode. By doing so, LIBs convert chemical energy directly into electrical energy. The operating principle is based on three main mechanistic steps, whose mathematical formulation close to equilibrium conditions are given below.

Firstly, the chemical diffusion of (neutral) lithium atoms inside the electrodes (cathode and anode), which involves both the chemical diffusion of lithium ions Li^+ and electrons e^-, will be discussed. The driving force for this process is given by the gradient of the lithium chemical potential inside the electrode material $\left(\frac{\partial}{\partial x}\right)\mu_{Li}$, with $\mu_{Li} = \tilde{\mu}_{Li^+} + \tilde{\mu}_{e^-}$ and the transport coefficient by the ambipolar conductivity $\sigma^\delta = \left(\sigma_{Li^+}^{-1} + \sigma_{e^-}^{-1}\right)^{-1}$. The lithium flux is then given by

$$j \propto -\sigma^\delta \left(\frac{\partial}{\partial x}\right)\mu_{Li} \ . \tag{1.2}$$

This is generally the slowest of the three processes and the reason why electrode materials are often nano-sized (compare [35]).[1]

Secondly, the reversible Li ion transfer at the electrode | electrolyte interfaces is described. Here, the driving force is given by the difference in the electrochemical potentials of Lithium ions in both phases $\Delta\tilde{\mu}_{Li^+}$. Close to equilibrium the transport coefficient can be expressed by the exchange rate $\Re$ of the corresponding process, so that the lithium flux through the interface is given by

$$j \propto -\Re\Delta\tilde{\mu}_{Li^+} \ . \tag{1.3}$$

Thirdly, the lithium ion transport through the electrolyte is discussed. This is essentially a steady-state process, with transient phenomena being of dielectric nature and occuring on the order of nanoseconds. The driving force is determined by the gradient of the electrochemical potential of the Lithium ions $\left(\frac{\partial}{\partial x}\right)\tilde{\mu}_{Li^+}$, with the transport coefficient being the Li^+ conductivity σ_{Li^+}. Hence, the lithium flux in the electrolyte is

---

[1]Expressing the driving force in terms of lithium concentration gradients, the transport coefficient is given by the chemical diffusion coefficient D^δ and for the flux follows $j \propto -D^\delta \left(\frac{\partial}{\partial x}\right)c_{Li}$. Mass balance requires $\dot{c} \propto -\left(\frac{\partial}{\partial x}\right)j$.

given by

$$j \propto -\sigma_{Li^+} \left(\frac{\partial}{\partial x} \right) \tilde{\mu}_{Li^+} \ . \tag{1.4}$$

Notably, electroneutrality is kept due to the compensating electron flow through the outer circuit. A more elaborated overview on transport and storage can be found in [35].

1.1.4 Storage mechanisms

Four different mechanisms to store lithium in an electrode exist:[2]

1) The single-phase mechanism in which the lithium atoms are intercalated into a host structure, changing its overall chemical composition as a single phase. This mechanism is found e.g. in the layered $Li_x TiS_2$ for $0 \leq x \leq 1$ [36].

2) The two-phase mechanism in which the electrode consists of two different phases transforming into each other upon (de)lithiation, changing the ratio of both phases within the electrode material. This mechanism is found e.g. in $LiFePO_4$ | $FePO_4$ electrode materials. How exactly the phase transformation occurs in a multi-particle system is still under discussion and depends inter alia on particle size, morphology and apparently even on the charge rate (more details are compiled in subsection 1.2.4).

3) The multi-phase mechanism which is the underlying process of conversion reactions. The phase manifold is the reason why electrodes undergoing such a reaction normally show a bad cycle stability. An interesting exception is found by Zhu et al. using a very special geometry and morphology for their MoS_2 anode material ($MoS_2 + Li \rightarrow Mo + Li_2S$) leading to a very good reversibility [12].

4) The interfacial storage of lithium. This storage mechanism is related to a redistribution of charge carrier concentrations in the interfacial regions [37]. It can contribute a non-trivial share to the overall electrode capacity when it comes to very small particles (nanocomposites) with a high surface area to volume ratio. The phenomenon is especially interesting when it comes to the so-called job sharing mechanism [38], in which one phase stores Li^+ and the other e^-, as it is found e.g. for the Li_2O:Ru system [39].

---

[2]Very often it is only refered to 3 mechanisms, being the homogeneous intercalation, phase formation and interfacial storage mechanism.

1.2 LiFePO$_4$

LiFePO$_4$ is one of the most promising cathode materials for LIBs and is a prototype of olivine-type materials for the application in Li-ion batteries. It has been intensively studied during the last years, because of its good electrode performance, favorable energy and power density, low cost, safety and low toxicity [24, 40, 41]. Since it was first mentioned as a cathode material for LIBs in 1997 [24, 42], several thousand publications in peer-reviewed journals and even more than a hundred review articles and book chapters have been published. Most of them report on several different chemical (e.g. [43]) and physical (e.g. [44]) synthesis routes, effects of coatings (e.g [45]) and morphologies (e.g. [46]) and study the electrochemical properties (e.g. [47]) and defect chemistry (e.g. [48]), as well as calculating chemical and physical properties (e.g. [49]). On the other hand, investigations offering a deeper understanding of the phase transformation during lithium extraction and insertion, especially in terms of intrinsic properties, i.e. defect chemistry, are rare and will be subject of this thesis. Due to the huge amount of literature about LiFePO$_4$, an all-embracing overview can not be given within the introduction of this thesis. Instead, only a selection of the main characteristics and features is summarized.

1.2.1 Structure

The olivine structure of LiMXO$_4$ with the space group Pnma is shown in figure 1.2. It is built up by corner-sharing MO$_6$ (M=Fe, Ti, V, ...) octahedra and XO$_4^{n-}$ (X= P, S, As, Mo, ...) tetrahedral anions. The oxygen atoms form a distorted hexagonal close packed (hcp) structure with Fe and Li atoms occupying half of the octahedral and P atoms sitting on one-eighth of the tetrahedral sites. There are two crystallographically distinct octahedral positions that also differ in size: the M1 site with an inversion center symmetry and the M2 octahedron with a mirror symmetry. This favors an ordering in olivine structures when containing cations of different size and charge. In LiFePO$_4$ the lithium ions usually occupy the smaller octahedral sites with $\tilde{I}$ symmetry (M1),
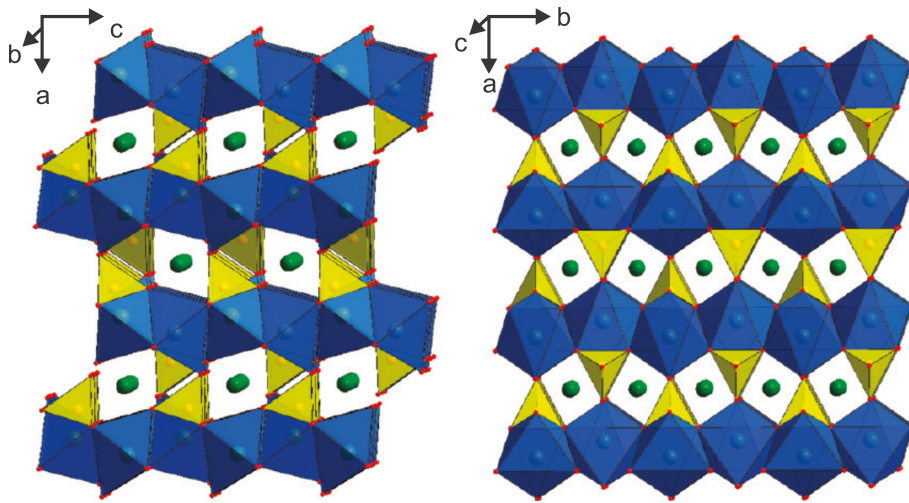
Figure 1.2: Crystallographic structure of LiFePO$_4$. Polyhedral representation of the structure of LiFePO$_4$ (space group Pnma) viewed along the b-axis (left) and along the c-axis (right). The iron octahedra are shown in blue, the phosphate tetrahedral in yellow, and the lithium ions in green (taken from [50]).

while Fe usually sits in the octahedral M2 sites. In this structure the M(2) sites are linked together over the corner-sharing FeO$_6$ octahedra within the b-c plane, while the edge-sharing LiO$_6$ octahedra form a linear chain along the b-axis. Each LiO$_6$ octahedra shares edges with two FeO$_6$ octahedra and two PO$_4$ tetrahedra. Furthermore have the FeO$_6$ and the PO$_4$ group one edge in common.

The strong P-O bonds result in a stable backbone of PO$_4$ polyanions and only small deformation from the orthorhombic symmetry occurs upon full delithiation [51]. The lattice parameters of LFP in the Pnma space group are reported to change upon delithiation from a = 10.334 Å, b = 6.008 Å, and c = 4.693 Å for LFP to a = 9.821 Å, b = 5.792 Å, and c = 4.788 Å for FP, so that the unit cell volume decreases by about 6.5 % [24].

1.2.2   Defect chemistry

Understanding the defect chemistry of a material is essential to understand its electrochemical properties and finally to optimize these properties by changing its defect chemical situation, e.g. via doping. While the LFP phase and its delithiated form, the FP phase, essentially refer to the same crystallographic structure, they behave from a defect chemical point of view antagonistically: LFP is a p-type electronic conductor

exhibiting lithium vacancies as ionic charge carriers, while FP is a n-type electronic conductor with lithium interstitials as ionic carriers [52, 53, 54, 55]. This opposing behaviour of the nature of electronic and ionic charge carriers, as illustrated in figure 1.3 by the symmetric dependence of the defect concentrations on the acceptor and donor content in LFP and FP, can easily be understood when - in a gedankenexperiment - assuming a continuous solid solution from FP to LFP.
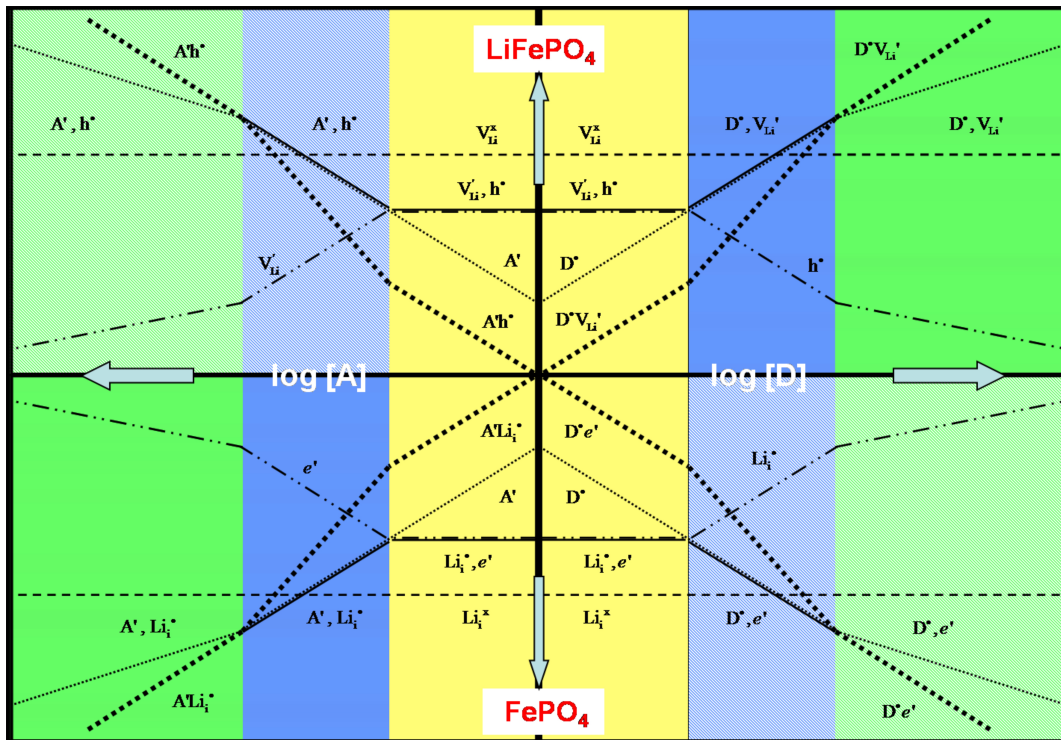
Figure 1.3: Comprehensive representation of the defect chemistry in LFP and FP. Charge carrier concentration as a function of acceptor (A) and donor (D) dopant concentration for $LiFePO_4$ and $FePO_4$ (taken from [48]).

Upon lithiation of FP, lithium occupies interstitial positions (Li-ion conduction), while a missing lithium atom on the same crystallographic site in LFP is considered as a lithium vacancy (Li-vacancy conduction). Furthermore, introducing lithium into $FePO_4$ fills the almost empty conduction band with electrons (n-type electronic conduction), while in $LiFePO_4$ the very same electronic band is the completely filled valence band, with electronic defects (holes) for Li-deficient LFP (p-type electronic conduction). A rather comprehensive description is given in reference [52] and figure 1.3 nicely elucidates this opposing behaviour, summarizing the charge carrier concentrations as a function of dopant concentration for both LFP and FP. While the formation

of vacancies and interstitials in the Fe- and O-sublattices of LFP are energetically unfavorable [56], anti-site defects ($Fe_{Li}^{\cdot\cdot}$) can easily be formed [17]. The defect concentration as a function of lithium activity in LFP is shown in the Kröger-Vink diagram (also called Brouwer diagram) in figure 1.4, illustrating the transition between the defect chemical D- and P-regime.
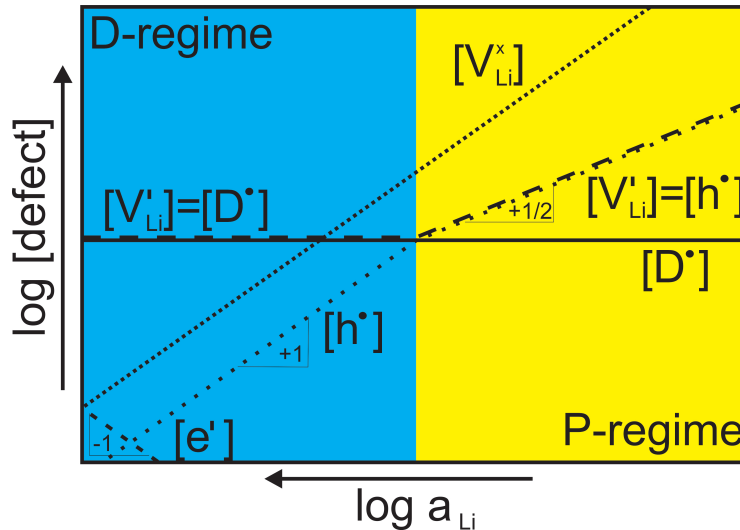

Figure 1.4: Kröger-Vink diagram. Illustration of the defect concentration as a function of lithium activity in LFP (according to [52]).

The D-regime is present at high lithium activity or in donor doped materials, while at low lithium activity (high lithium deficiency) or in acceptor doped LFP the P-regime is observed. In the D-regime, lithium vacancies (V_{Li}') are compensated by intrinsic anti-site defects ($Fe_{Li}^{\cdot\cdot}$) or extrinsic donor dopants, e.g. gallium on an iron site ($Ga_{Fe}^{\cdot\cdot}$). By increasing the donor concentration, being equivalent to go further to the left in the Kröger-Vink diagram, the hole concentration [$h^{\cdot}$] is decreased, while the lithium vacancy concentration [V_{Li}'] is approximately fixed by the dopant. This results in an increased ionic and decreased electronic conductivity, as proved by Amin et al., measuring the different ionic and electronic conductivities of 1 % Al donor-doped LFP single crystals [57, 58] and 1 % Si donor-doped LFP single crystals [59]. On the other hand, going further to the right in the Brouwer diagram by acceptor doping the material or lowering the lithium activity (by delithiation), the increase in [V_{Li}'] is compensated by an increase of hole concentration ([$h^{\cdot}$]). Completing the picture, Zhu et al. measured a predominant electronic conductivity for polycrystalline heterosite $FePO_4$, proving that

lithium interstitials ($Li_i^.$) and electrons (e') are the major charge carriers in $FePO_4$ [54].

1.2.3 Electrochemical properties

The theoretical capacity of $LiFePO_4$, following the (de)lithiation reaction

$$LiFePO_4 \leftrightarrow x \cdot FePO_4 + (1 - x) \cdot LiFePO_4 + x \cdot Li^+ + x \cdot e^- \qquad (1.5)$$
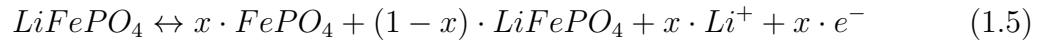
is about 170 mAh/g. Its crystallographic structure and defect chemical properties directly determine its (electrochemical) properties, ultimately leading to its pronounced anisotropic behaviour concerning ionic and electronic conductivities, as well as lithium chemical diffusion [15, 55]. As shown in figure 1.5, the polyanionic crystal structure favors lithium transport along one-dimensional pathways, formed by the edge-sharing LiO_6 octahedral chains along the **b** axis of the crystal [50, 56].
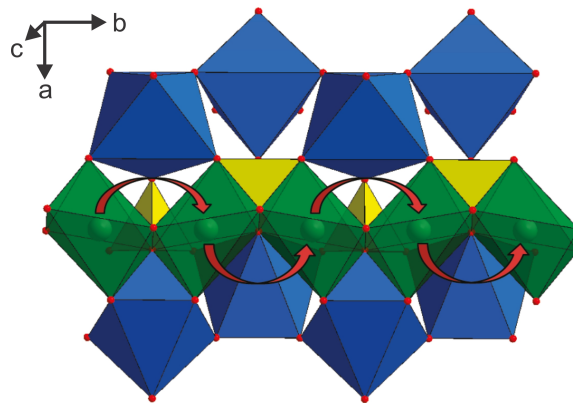
Figure 1.5: Curved trajectory of Li ion transport along the b-axis of LiFePO₄. The red arrows indicate the lithium transport along the fast **b** direction in LFP. The colour scheme of the polyhedral representation of the structure is the same as in figure 1.2 (taken from [50]).

Additionally, theoretical calculations predict a predominant lithium transport along the **b**-axis due to the lower energy barriers [60], which has also been observed for short-range motion [61]. On the other hand, experiments using oriented LFP single crystals, grown via optical floating zone technique [62], showed lowered mobilities along **a** (100) but unexpectedly similar values for **b** (010) and **c** (001), resulting in a two-dimensional anisotropy of electronic and ionic conductivities as well as lithium chemical diffusion in the **b-c** plane [53, 55]. Here, the defect chemistry comes into play, since already the

native anti-site defects present in LFP ($Fe_{Li}^{\cdot}$), functioning not only as intrinsic donor dopants, block the lithium migration along the curved 1d channels, resulting in the slower diffusion, decreasing electrochemical performance [15, 53, 56]. Figure 1.6 shows the expected unblocked capacity as a function of channel length for different defect concentrations. This nicely illustrates the direct correlation between the defect chemical situation and its influence on the electrochemical properties of a given material.
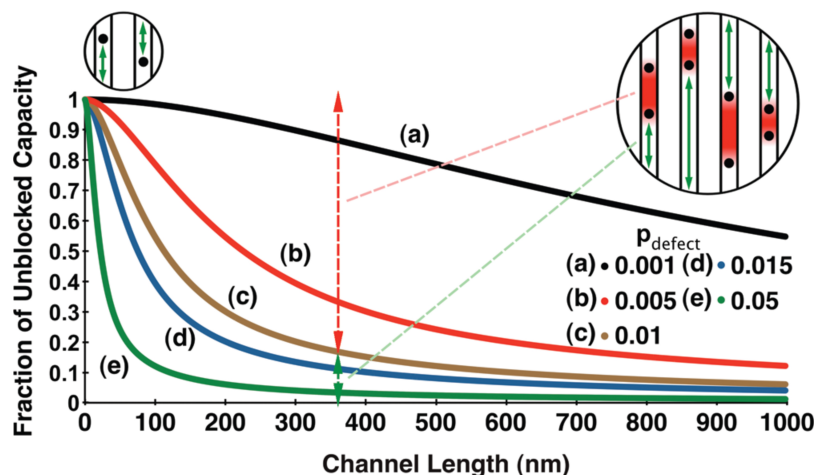

Figure 1.6: Unblocked capacity in LFP as a function of channel length. Expected unblocked capacity vs. channel length in LFP for various defect concentrations (taken from [15]).

The influence of particle size, morphology and defect chemistry, together with the exact lithium content in LFP on the electrochemical properties, is also likely to be the reason, why for the lithium diffusion coefficient D^{δ} of LFP at room temperature very different values have been measured ranging from 10^{-10} to 10^{-16} cm^2/s - a difference of six orders of magnitude [63, 64, 65, 66]. Along the three principle axes in macroscopic LFP single crystals D^{δ} is measured to be on the order of 10^{-12} cm^2/s along (010) and (001) and 10^{-14} cm^2/s along (100) (Pnma space group) [53, 55].

As already mentioned in subsection 1.2.1, the strong P-O bonds result in a stable backbone of PO$_4$ polyanions and only small deformations occur during cycling. Another related positive effect of the strong P-O bonds is the good thermal stability of LFP and its beneficial safety performance, since no gaseous oxygen is formed upon delithiation or heating [67]. Furthermore the very similar volume and crystallographic structure of LFP and FP prevents capacity degradation, since disintegration of particles upon

cycling is avoided (for small enough particles) [51, 68].

The already mentioned measurements on LFP single crystals furthermore proved the predominant electronic conductivity ($\sim 10^{-7}$ S/cm (**b**, **c**), $\sim 10^{-8}$ S/cm (**a**)) along all three crystallographic directions, being about five orders of magnitude higher than the respective lithium ion conductivities at room temperature ($\sim 10^{-12}$ S/cm (**b**, **c**), $\sim 10^{-14}$ S/cm (**a**)) [53]. Hence, LFP possesses both a low electronic conductivity, caused by the separation of the FeO_6 octahedra by the PO_4 tetrahedrons [69], as well as a very low ionic conductivity.[3] To improve the electrochemical performance and to overcome the drawbacks of the low ionic and electronic conductivities, three main strategies can be applied: the introduction of secondary phases (coating), decrease of particle size and tuning of the defect chemistry (doping).

The most widely used coatings of LFP particles are composed of carbon, enhancing the electronic conductivity of the material. Ravet et al. have first reported such a coating [71] and since then numerous carbonaceous organic compounds and various synthesis routes have been tested [72]. Besides its high electronic conductivity, carbon offers a low specific weight, low costs, sufficient chemical stability and is easily penetrated by lithium ions. It can be introduced as a coating by several techniques, whereat already small amounts (below 2 wt%) result in a significant performance increase [72]. Unfortunately, incomplete carbon layers lead to polarization effects and insufficient rate performances [73]. Hu et al. solved this problem using RuO_2 to patch the incomplete carbon network, reducing the polarization effects and improving the rate performance [74]. Also coatings of glassy phases have been reported, offering not only high electronic conduction (if doped with transition metals [75]), but also superior ionic conductivity [76].

While figure 1.6 already gives a hint, why "nano-sizing" is so important and the anisotropy of the ionic and electronic conductivities in LFP favors certain particle morphologies, also pure geometrical effects play a role. Reducing the particle volume of a spherical particle by a factor of 2, thus creating 2 smaller particles, increases the overall surface area by a factor of $2 \cdot \frac{1}{2}^{2/3}$ (about 26 %), increasing the contact area with

---

[3]Compared to other cathode materials, the room temperature chemical diffusion coefficient of lithium in LFP, as well as the electronic conductivity, are at least three orders of magnitude lower than in $LiCoO_2$ (10^{-12} vs. 10^{-9} cm^2/s and 10^{-7} vs. 10^{-4} S/cm, respectively [53, 70]).

the electrolyte and decreasing the geometrical part of the resistance. Furthermore, for a sample of thickness L, the storage and equilibration time τ_{eq}, respectively, is given by

$$\tau_{eq} \propto \frac{L^2}{D^\delta} \ . \tag{1.6}$$

Here, D^δ is the lithium chemical diffusion coefficient. Thus τ_{eq} is significantly decreased for smaller L. But going smaller in particle size may not only decrease the volumetric capacity because of lower packing densities, but also the gravimetric capacity due to the comparably higher amount of carbon coating, as well as increase the occurrence of undesirable surface reactions, lowering the cycling performance [41].

According to equation 1.6, τ_{eq} also depends on D^δ and hence on the defect concentrations. It was first found by Chung et al. [77] that cation doping with metal atoms supervalent to Li^+ (e.g. with Zr^{4+}, Nb^{5+}, ...) can increase electronic conductivity in LFP to values up to 10^{-2} S/cm (corresponding to an increase of eight orders of magnitude). Although it is argued that this tremendous increase in electronic conductivity originates in residual carbon from precursors [78] or formation of a Fe_2P phase upon heating [79], the already cited single crystal experiments on Al and Si doped LFP [57, 58, 59] proved that doping of $LiFePO_4$ is possible and measurably influences the underlying defect chemistry.

1.2.4   Phase transformation

A lot of effort has been made, disclosing the phase transformation mechanism in $LiFePO_4$ [51, 80, 81, 82, 83, 84, 85]. Nevertheless, the mechanism is still not fully understood and appears to depend, like the electrochemical performance, on parameters, such as particle size and morphology due to the small energetic differences involved [15, 86]. The extensive debate on the mechanism of phase transformation is mainly due to the lack of *in situ* observations with appreciable space and time resolution on materials with a defined defect chemistry. The intermixing of results obtained by chemical delithiation [68, 80, 81, 87] and electrochemical delithiation [51, 81, 82, 83], although driving forces and the mechanism of combined Li^+ and e^- insertion differ from each

other, does not contribute to clarify the picture. A nice review focussing on the details of the possible lithium insertion mechanisms in LFP is given by Malik et al. [88]. Here, only some of the main points are shortly summarized.

While in small particles interface formation may already cost so much energy, that nanocrystals stabilize the solid solution form, analyzing the phase diagram for particles larger than 100 nm reveals a solubility of FP in LFP and vice versa of up to 10 % at room temperature [13, 86, 89, 90, 91]. In between a two-phase regime is energetically favourable, separated from the solid solution by only small excess energies of about 50 mV [85]. These small excess energies can easily be washed out by effects such as capillary pressure or elastic interactions, hence opening the field for various possibilities of phase transformation mechanisms. Indeed, there is evidence for a shrinking and eventually disappearing miscibility gap and single-phase mechanism along a solid solution pathway upon particle size decrease, respectively [15, 86]. Such a solid solution mechanism may be complex and influenced by coherency stress effects, as well as include the formation of amorphous phases [92]. But most of the proposed models favor a two-phase mechanism involving the co-existence of two intraparticle phases [51, 80, 81, 82, 83, 84]. For large single particles the formation of such an interface is favoured and a shrinking core as well as the inverse scenario and delithiation from only one side of the particle has been reported [81, 93]. Furthermore, for large single crystals fragmentation and loss of single crystallinity upon chemical delithiation have been found by Weichert et al. [68]. In addition a spinodal-like decomposition of LFP is taken into account [94] and stripe patterns within single crystals formed by alternating lithiated and delithiated Phases with periods typical for such a spinodal decomposition have also been observed [80]. On the other hand, Gu et al. even report on the presence of a $Li_{0.5}FePO_4$ staging phase in which every second Li layer is either Li-free or fully occupied [95]. Such ordering phenomena may also lead to other stabilized phases as kinetic or thermodynamic attractors, e.g. integer multiplies of 1/6 [95]. In fact, Orikasa et al. report on a metastable Li_xFePO_4 phase (x=0.6-0.75) upon lithium (de)intercalation [96], whereat ordered intermediate phases are also found and discussed as low-energy solutions for the LFP/FP interface itself [97].

It is worth noting, that the (de)lithiation mechanism of $LiFePO_4$ reveals up to a certain

degree a scale invariant behaviour: the ordering phenomena found by Gu et al. on the level of individual atomic layers [95] corresponds to the stripe pattern found by Chen et al. [80], now on the order of 100 nm within a single particle, and can be continued on a multi-particle level, where generally a digital phase distribution is realized, with particles either almost completely lithiated or delithiated [82, 98]. Nevertheless, this correspondence has to be taken with a pinch of salt, as the reason for the digital phase distribution lies in the non-monotonistic dependence of the lithium chemical potential μ_{Li} on the lithium content [99]. But also on the multi-particle level the particle by particle mechanism of lithium intercalation seems not universal, but instead Li et al. reported that it can be changed to a concurrent lithium intercalation mechanism by applying higher currents [100]. This is attributed to a nearly constant current density at each particle undergoing the phase transformation within the full electrode, being independent of the cycling rate, so that higher currents are achieved by increasing the active particle population.

Chapter 2

Experimental Techniques

In this section a short general introduction to the main sample preparation and characterization techniques used within the framework of this thesis is given. For details of other, commonly used methods, which also find their way into this thesis, the interested reader is referred to some relevant literature. These methods include X-ray diffraction (XRD) [101], Raman spectroscopy [102], Transmission Electron Microscopy (TEM) [103, 104, 105, 106], secondary ion mass spectrometry (SIMS) [107], inductively coupled plasma optical emission spectrometry (ICP-OES) [108], molecular beam epitaxy (MBE) [109] and other thermal evaporation techniques, as well as sputter deposition [110], and cyclic voltammetry (CV) [111].

2.1   Pulsed Laser Deposition

Pulsed laser deposition (PLD) belongs to the group of physical vapor deposition (PVD) techniques [112] and is widely used for the preparation of thin films [113]. Laser pulses, typically generated by excimer or Nd:YAG laser, with energy densities > 1 J/cm^2 and wave length between 200-400 nm are directed towards the target. The pulses are either absorbed at the surface of the target via free charge carriers (mainly metallic character of the target) or in the near-surface volume of the target by electrons and phonons (mainly dielectric character of the target). The absorbed energy leads to a temporally melting of the target surface (formation of a Knudsen-layer) and a subsequent evaporation of target material. The evaporated material forms a plume consisting of

electrons, ions, atoms, molecules, clusters and possibly also micro-sized particles. If a dense target with a well-polished surface is used, the plume forms symmetrically perpendicular to the surface with a certain, elemental specific, angular distribution within, and expands due to the short length of the mean free path inside. Its constituents are transported through an gaseous atmosphere of defined pressure, chosen in accordance to the target material (e.g. generally oxygen is used for oxides, here Ar and Ar/H_2 (5 %) are used), and deposited on a typically heated substrate in a distance of a few cm (compare figure 2.1).
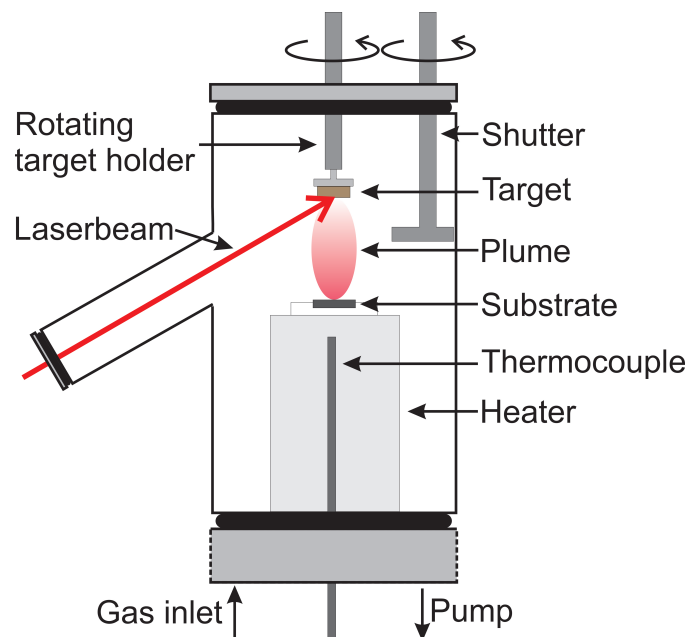

Figure 2.1: Drawing of the used PLD chamber. The positions of all the important components inside the chamber are depicted.

The heating allows a sufficient diffusion of the deposited material on the substrate and influences the crystallinity and morphology of the formed thin film. Since a good film quality and sufficient growth rate is correlated to an absorption of the laser pulses near the surface, to avoid exfoliation of the whole target and to minimize the effect of an expulsion of the liquefied material from the molten zone of the target by the shock wave recoil pressure of the evaporated material (catchwords: splashing, droplet formation), a good laser-target combination for dielectric materials is a combination where the frequency of the used laser corresponds to a high density of states (DOS) in the phononic band structure of the target material. This general statement is also found in particular

by Kuwata, Morcrette and Guillot-Noël et al. [114, 115, 116], reporting inter alia on the relation between the surface roughness and droplet density of PLD-deposited solid electrolyte thin films and the optical band gap of the used target materials, finding the expected correlation: the higher the optical absorption coefficient near the used wavelength of the laser, the lower the droplet density on the surface of the deposited films. The quality and properties of the formed thin films depend, besides other system dependent factors, on the target material (typically dense and homogeneous gives best results), the substrate material (including orientation), the target-substrate distance, base- and deposition pressure, as well as on the composition and the pressure of the gaseous atmosphere during deposition and possible annealing, process temperature and cooling rate, laser frequency and energy (density), beam profile and pulse duration (typ. 10-50 ns). Also the deposition rate depends on most of the mentioned parameters and can therefore vary between 0.5 nm/min and 20 nm/min.
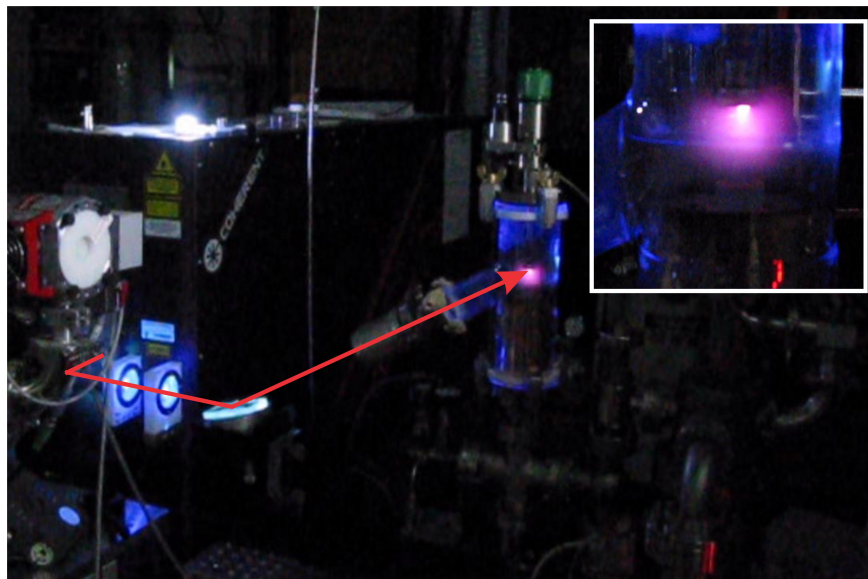

Figure 2.2: Photograph of the used PLD system. The Picture shows the PLD system upon deposition of a $LiFePO_4$ thin film. The path of the laser beam is indicated in red. The small inset picture shows the appearance of the plume, as well as its position within the target-substrate arrangement in more detail.

Figure 2.2 presents the used system consisting of a KrF excimer laser COMPEX PRO 201F from Coherent ($\lambda = 248$ nm), a quartz chamber with a heatable substrate holder (up to 850 °C substrate temperature), a heat shielding, a rotable target holder, a shutter between target and substrate, gas inlets, a pumping system, pressure gauges

and some optics connecting the laser and the chamber with each other. The upper part with the target holder can be removed to exchange the sample and can also be displaced by a pyrometer to calibrate the thermocouples of the heater with the real surface temperature of the sample. A set of optimal parameters for depositing $LiFePO_4$ with this system is given in subsection 4.1.2.

2.2   Electron Microscopy

Scanning Electron Microscopy (SEM) as well as Transmission Electron Microscopy (TEM) are widely used to obtain images of a sample with a lateral resolution of a few nanometers (SEM) and even atomic resolution (TEM) down to 0.05 nm [117]. The main parts of an electron microscope are the electron gun to generate an electron beam, the electron optic to focus the electron beam on the surface of the sample, and the detector, which is installed on the same side of the sample as the gun (SEM) and on the other side of the sample as the gun (TEM), respectively, to produce images from the electrons, which have interacted with the sample. Furthermore the whole system needs to be under a vacuum of at least 10^{-3} Pa to allow the electrons a maximum mean free path. For more details about the principle of electron microscopy the reader is referred to my diploma thesis in chemistry [118] as well as to more common literature [119]. Here, I will only shortly dwell on the opportunity to alter a samples surface by a Focused Ion Beam (FIB) mounted inside a SEM, which is used to fabricate the all-solid-state micro-sized thin film battery studied in chapter 5, as well as on the spectroscopic method of measuring the energy loss of scattered primary electrons in a TEM, the so-called Electron Energy Loss Spectroscopy (EELS), used in the next chapter.

2.2.1   Focused ion beam

The operating principle of a focused ion beam system is very similar to the operating concept of a SEM, except that ions instead of electrons are focused on the surface of a sample, where the beam is used for imaging (at low beam current), sputtering (at high beam current) or even for depositing several materials. The first FIB was

built by Levi-Setti et al. using hydrogen ions [120]. Today, most of the commercial FIB systems use a liquid metal ion source (LMIS), commonly filled with elemental gallium. But also a variety of other elements from Al to Zn are used in LMIS, with gold being one of the favorite supply metals in earlier days [121]. Quite recently even neon and helium ion beams are integrated in FIB systems by using gas field ion sources (GFIS) [122, 123]. They are especially of interest due to their superior imaging capabilities, even compared to state-of-the-art SEMs, with lateral resolutions below 1 nm and only very small sputter rates, as well as for applications in nanoscale lithography and synthesis [124, 125].

When the primary ion beam rasters the surface of a sample, secondary ions, neutral atoms and secondary electrons are produced. Collecting the secondary ions or electrons is used, as in SEMs, to form an image of the samples' surface, whereat at small beam currents the amount of sputtered secondary ions, as well as neutral atoms, is very small. On the other hand, using high primary ion beam currents allows for a precise removal of material from the sample. In both cases ions from the FIB are incorporated into the treated sample, even when using grazing incident conditions as it is the case for TEM preparation. Besides imaging and local sputtering, the FIB is also used to deposit other materials on a sample by introducing a precursor gas through a nozzle in the proximity of the impact point of the ion beam. The chemical bonds of the adsorbed precursor gas are broken by the ion beam induced generated secondary electrons, leading to volatile and non-volatile components of the precursor gas. The latter ones are subsequently deposited on the samples' surface. To ensure, that the recently deposited material is not sputtered by the incident ion beam, the FIB is used to raster the area where material should be deposited to allow new gas to adsorb on the surface. Parameters such as beam focus, dwell time and refresh time (time between two visits by the FIB of the same spot) are crucial for a successful deposition. Such a deposition can also be performed by using the primary electron beam in a SEM at significant lower deposition rates, but in exchange without any possible surface damage through sputtering effects. Typical precursor gases include Pt, W, and Pd, whereat the formed layers do not consist of pure Pt, W or Pd, but include also carbon from the precursor gas and e.g. Ga from the ion beam. In chapter 5 Ion Beam Induced Deposition of Platinum (IBID-Pt) is

used to build the current collectors of the all-solid-state micro-sized batteries.

2.2.2   Electron energy loss spectroscopy

Electron Energy Loss Spectroscopy (EELS) is an absorption spectroscopy method, probing the local unoccupied density of states (DOS), revealing structural and electronic information about the chemical elements and their stoichiometry in the specimen, the bonding and nearest-neighbor distribution. More precisely, EELS measures the energy loss of inelastically scattered primary electrons from a transmission electron microscope source, after their interaction with core electrons of a specimen. The inelastically scattered electrons loose energy, i.e. velocity, upon interaction. Therefore they can be studied using a magnetic prism creating a uniform magnetic field $\mathbf{B}$ perpendicular to the direction of travel of the primary electrons, forcing them into a circular orbit with radius r given by $r \propto \frac{v_e}{B}$, with v_e being the velocity of the scattered electrons and B the strength of the magnetic field. By this, the scattered electrons are energetically dispersed and their energy distribution, resulting from a different energy loss upon interaction with the specimen, gives the EELS spectrum. Such a spectrum exhibits very similar features as an absorption spectrum obtained by X-ray absorption spectroscopy (XAS) (see figure 2.3 a)). This can be understood by comparing the expressions of the cross sections for both interactions with each other. As will be stated in section 2.3: the emission of photoelectrons is the main contribution for X-ray absorption. Thus, within the dipole approximation, the cross section for this interaction is given by [126] [1]

$$\frac{d\sigma}{dE} \propto |\langle f \mid \boldsymbol{\varepsilon} \cdot \mathbf{r} \mid i \rangle|^2 \cdot \delta(E_i - E_f + E) \tag{2.1}$$

---

[1] The so-called Fermi's "golden rule" provides the transition rate $W_{i \to f}$, i.e. the probability of transition per unit of time, from an initial energy eigenstate $\mid i >$ into a single final eigenstate $\mid f >$ due to a perturbation $\hat{U}$ (incoming photon or electron): $W_{i \to f} = \frac{2\pi}{\hbar} \left| \langle f | \hat{U} | i \rangle \right|^2 \cdot \delta(E_i - E_f + E)$. Integrating for a given initial state over all possible final states gives the one-to-many transition rate, i.e. for example the absorption cross section of photons with defined energy, given by $W_{i \to f} = \frac{2\pi}{\hbar} \left| \langle f | \hat{U} | i \rangle \right|^2 \cdot \rho$, with ρ being the density of final states, i.e. the number of states per energy unit within a small energy band.

with $\mid i >$ being the initial state of the system, particularly represented by well-localized electronic core states, $< f \mid$ the final state of the system after X-ray absorption, i.e. an electron being excited to an afore unoccupied state or the continuum, $\boldsymbol{\varepsilon}$ the polarization vector, $\mathbf{r}$ the position vector, E_i the energy of the initial state, E_f the energy of the final state after absorption of the photon and E the energy of the absorbed photon. This is equivalent to the dipole approximation of the cross section in EELS given by

$$\frac{d\sigma}{dE} \propto \mid \langle f \mid \mathbf{q} \cdot \mathbf{r} \mid i \rangle \mid^2 \cdot \delta(E_i - E_f + E) \tag{2.2}$$

with $\mathbf{q}$ being the momentum transfer vector, fulfilling the same function $\boldsymbol{\varepsilon}$ does in XAS (here E presents the energy loss of the inelastically scattered primary electron).

This parallel in the underlying theory gives rise to similar analyzing procedures and retrievable information: what is called XANES (X-ray Absorption Near Edge Structure) and EXAFS (Extended X-ray Absorption Fine Structure) in X-ray absorption spectroscopy (see section 2.3 for further explanations) finds its counterpart in the so-called ELNES (Energy Loss Near Edge Structure) and EXELFS (Extended Energy Loss Fine Structure) in electron energy loss spectroscopy, respectively. While both XANES and ELNES study a region of less than 100 eV directly at the absorption edge, where the emitted electrons are excited to unoccupied states of the studied material, EXAFS and EXELFS are used to analyze the interference pattern in a region up to 1 keV behind the absorption edge, where the emitted electrons are excited to the continuum (compare figure 2.3 c)). Due to this effect, within the dipole approximation, results from ELNES measurements can nicely be compared to the results obtained by EXAFS measurements, which are introduced in the next section in more detail.

Within this thesis, EELS measurements, or more precisely ELNES measurements, are used to measure at the Fe $L_{2,3}$ edge to track the changes in the electronic structure of Li_xFePO_4 to distinguish between Fe^{2+} and Fe^{3+}, which is a direct measure for the Li content in the investigated volume. More specific information about the experimental implementation, theoretical description and application of EELS can be found in references [106, 127].

2.3   X-ray Absorption Spectroscopy

X-Ray Absorption Spectroscopy (XAS) belongs to the family of spectroscopic meth-
ods, studying the physical interaction between electromagnetic radiation and matter
to obtain information about the electronic and structural properties of the analyzed
materials. In XAS core electrons are excited to unoccupied states or the continuum,
providing information about the unoccupied part of the local density of states (DOS)
and the short-range order within the material. Therefore the method has similarities
with X-ray photoelectron spectroscopy (XPS), where valence electrons of the material
are excited to energy states above the Fermi level, generally providing information
about the occupied part of the DOS. To obtain a good energy resolution and signal-to-
noise ratio, XAS measurements are usually performed at synchrotron radiation sources
providing tunable monochromatic X-ray beams with high photon fluxes.

The energy of the incoming photons can range from 100 eV up to 100 keV, whereat
X-rays with photon energies being lower (higher) than 5-10 keV are called soft (hard)
X-rays. In this energy range the photoelectric effect [128] is the main contribution for
X-ray absorption and other effects like Compton scattering and elastic scattering play
a minor role. Here, the absorption coefficient μ of the sample, being proportional to
its photoionization cross section, determining the probability for photoionization (com-
pare subsection 2.2.2 and footnote therein), is studied as a function of the incoming
photon energy $\mu(E)$. Figure 2.3 shows a typical X-ray absorption spectrum. Such a
spectrum possesses three major features:

1) a decrease of the X-ray absorption with increasing energy, nearly proportional to
$1/E^3$. This is since the probability for photoionization, due to the photoelectric effect,
can be related to the cross section of a single electron, which in turn is proportional to
$1/E^3$ (for more details see e.g. [129]).

2) a sharp increase in absorption for certain defined energy values, forming so-called
absorption edges. This increase in the absorption coefficient is found for energies of the
incident X-ray beam being equal to the binding energy of core electrons. It is based on
the sharp increase of the number of electrons participating in the photoelectric effect,
and therefore on the increase of the photoionization cross section of the material, when
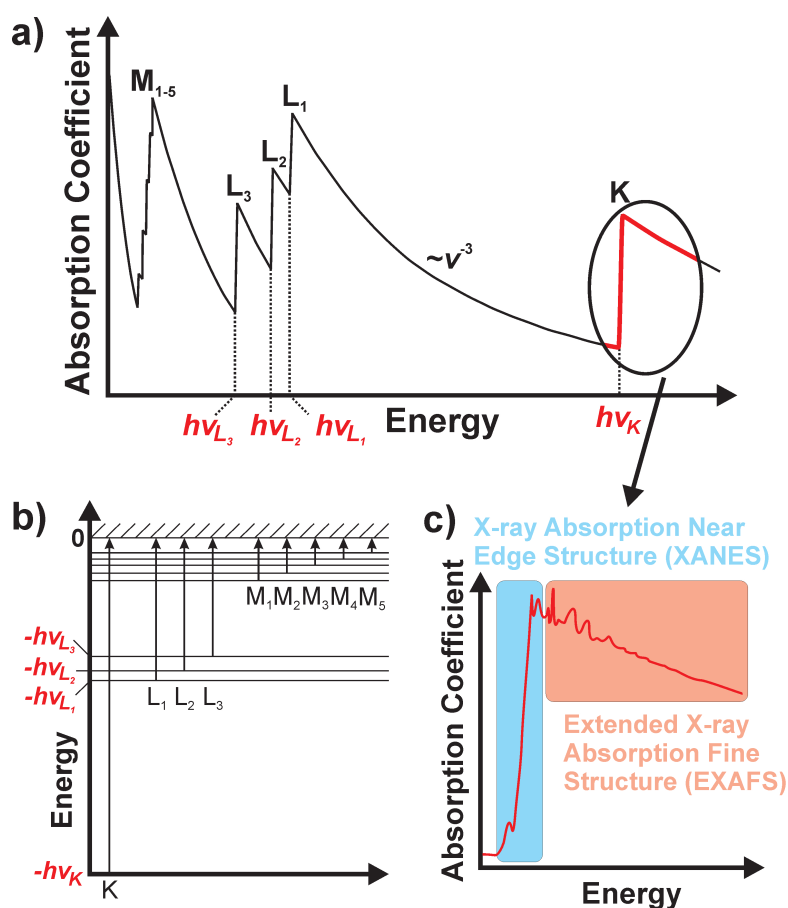such an energy value is reached.

Figure 2.3: X-ray absorption spectrum. a) Typical X-ray absorption spectrum featuring absorption edges and the exponential decrease of absorption with increasing energy of the incident beam. b) Energy level diagram of the same material, showing the connection to the absorption spectrum. c) Magnification of the K-edge showing the regions where XANES and EXAFS measurements are performed.

3) oscillations in the absorption coefficient, starting with an amplitude in the range of several percent of the total absorption, and lasting for up to several 100 eV directly behind the absorption edges until they are completely faded.

These oscillations can be understood when taken the quantum mechanical wave-like nature of the photoelectrons into account. Considering the surrounding atoms as point scatterers, the backscattered photoelectron waves interfere with the initial forward-propagating waves, causing the oscillations in the measured absorption coefficient (so-called short range order theory). In a first approximation this part of the spectra can be analyzed by assuming plane-waves and single scattering events.

As shown in part c) of figure 2.3, XAS is subclassified in two experimental methods, depending on the nature of the electronic transition. The so-called Near-Edge X-ray

Absorption Fine Structure (NEXAFS), also called X-ray Absorption Near Edge Structure (XANES), examines a region of less than 100 eV directly at the absorption edge, where the photoelectrons are excited to unoccupied states of the studied material. Shape and position of the adsorption edge comprise information about the chemical bonding, oxidation state and geometry of the absorption atoms. Accordingly, the Fe *L*-edge from $LiFePO_4$ shifts upon delithiation, and therefore oxidation of iron from Fe^{2+} to Fe^{3+}, forming $FePO_4$, by about 2 eV to higher energies due to a stronger bonding of the core electrons, for instance. Such a feature can be used as a fingerprint to easily distinguish between oxidation states and will be used throughout this thesis to (locally) determine the lithium content of Li_xFePO_4. Section 2.3.2 gives a more detailed introduction to the data analysis of the XANES spectra. In turn, the so-called Extended X-ray Absorption Fine Structure (EXAFS) studies a region up to 1 keV behind the absorption edge, where the photoelectrons are excited to the continuum and the analysis of the interference pattern, mentioned above, gives information about the short-range order around the absorption atom. Since in this thesis only XANES measurements are performed, the interested reader is referred for a more detailed description of EXAFS to the literature [130, 131].

There are three different ways to measure the absorption coefficient μ, which are all used within this thesis.

1) The probably easiest method is the transmission mode, where the ratio of the X-ray intensity before and after interaction with the sample is measured. For this purpose the sample has to be sufficiently thin, to circumvent saturation effects and ensure a good signal-to-noise ratio. Per construction, this method averages over the whole thickness of the sample; a separation in bulk and surface contributions is not possible.

2) After a photoelectron is excited, the unoccupied state is refilled by an electron of the sample material of higher energy. The gain in potential energy of this electron, given as the energy difference between its initial state and the initial core state of the photoelectron, is generally transferred to another electron which in turn will leave its bounded state, excited as a so-called Auger electron. The number of Auger electrons, as well as the number of secondary electrons excited via inelastic scattering with the relatively high-energy Auger electrons is proportional to the number of the initial pho-

toelectrons, and is therefore used as an indirect detection method of the absorption coefficient. Measuring the number of excited Auger electrons (Auger Electron Yield - AEY) with an electron multiplier gives very surface sensitive information from less than the top 1 nanometer of the sample, while measuring the sum of Auger, secondary and photoelectrons (Total Electron Yield - TEY) usually contains information of less than the top 10 nanometers of the material. This is due to the low mean free path of high energy electrons and the relatively higher mean free path of low energy electrons in solids. The TEY can also be measured as a sample current, evoked by the escaping electrons.

3) Instead of exciting an Auger electron the energy can also be released by irradiation of a photon. The probability for this process is in the soft X-ray region much lower than the emission of an Auger electron. But since the X-rays can penetrate through a thicker layer of the sample, equivalent to the fact, that the fluorescence photons contain also bulk information, the disadvantage of the lower probability and therefore the signal intensity is partly compensated. Measuring the Fluorescence Yield (FY) and the TEY are complementary, providing information about bulk and surface characteristics of a material.

XANES measurements have been performed at the synchrotron radiation facility HZB/BESSY II in Berlin at two different beamlines. At the ISISS (Innovative Station for *In Situ* Spectroscopy) beamline shown in figure 2.4, which is originally designed to perform *in situ* XPS and XAS measurements at catalytically active materials under defined gaseous atmospheres using monochromatic tunable X-ray radiation, FY and TEY are measured to determine the absorption coefficient and lithium concentration of electrochemically cycled $LiFePO_4$ electrodes at different state of charges, respectively (see chapter 3). Details of the used set up of the ISISS beamline can be found in reference [132] and relevant data of the beamline itself in reference [133]. At the MPI-IS UHV-STXM endstation "MAXYMUS", installed at the UE46-PGM2 undulator beamline, mainly designed to analyze element specific magnetic, as well as structural and chemical properties [134, 135], the X-ray absorption of thin film and micrometer-sized batteries with LFP electrodes is studied *in situ* during electrochemical (de)lithiation (see chapter 4 and 5). The principle of Scanning Transmission X-ray

Figure 2.4: Photograph of the Innovative Station for *In Situ* Spectroscopy. (taken from [133]).

Microscopy (STXM), employed at the "MAXYMUS" endstation, is explained in more detail in the next subsection 2.3.1.

2.3.1   Scanning transmission X-ray microscopy

Scanning Transmission X-Ray Microscopy using zone plate optics was first employed at the National Synchrotron Light Source (NSLS) in Brookhaven (USA) [136, 137, 138] in the late 1980s and is since then performed at several synchrotron radiation sources around the world. To the best of the authors knowledge, from the 47 synchrotrons operating worldwide [139], 10 research centers are currently running scanning X-ray microscopy beamlines using zone plate optics, which are besides the NSLS the Advanced Light Source (ALS) in Berkeley (USA) [140], the Canadian Light Source (CLS) in Saskatoon (Canada) [141], the Ultraviolet Synchrotron Orbital Radiation Facility (UVSOR) in Okazaki (Japan) [142], the European Synchrotron Radiation Facility (ESRF) in Grenoble (Frankreich) [143], the Swiss Light Source (SLS) in Villigen (Switzerland) [144], the Pohang Light Source (PLS) in Pohang (Korea) [145], the Shanghai Synchrotron Radiation Facility (SSRF) in Shanghai (China) [146], the Elettra Sincrotrone in Trieste (Italy) [147], and the Berlin Electron Storage Ring Society

for Synchrotron Radiation (BESSY II) in Berlin (Germany) [134, 135]. This list may not be complete since new instruments are still put into service like at the Diamond Light Source (DLS) in Oxfordshire (England) [148]. Here, I will not dwell on the physical principles of synchrotron radiation or the specifics of beamline and microscope configuration, but give a short introduction to the mode of operation of a STXM.

The used Scanning Transmission X-ray Microscope "MAXYMUS" is attached to the UE46 undulator beamline and together with the optical design of the beamline depicted in figure 2.5.
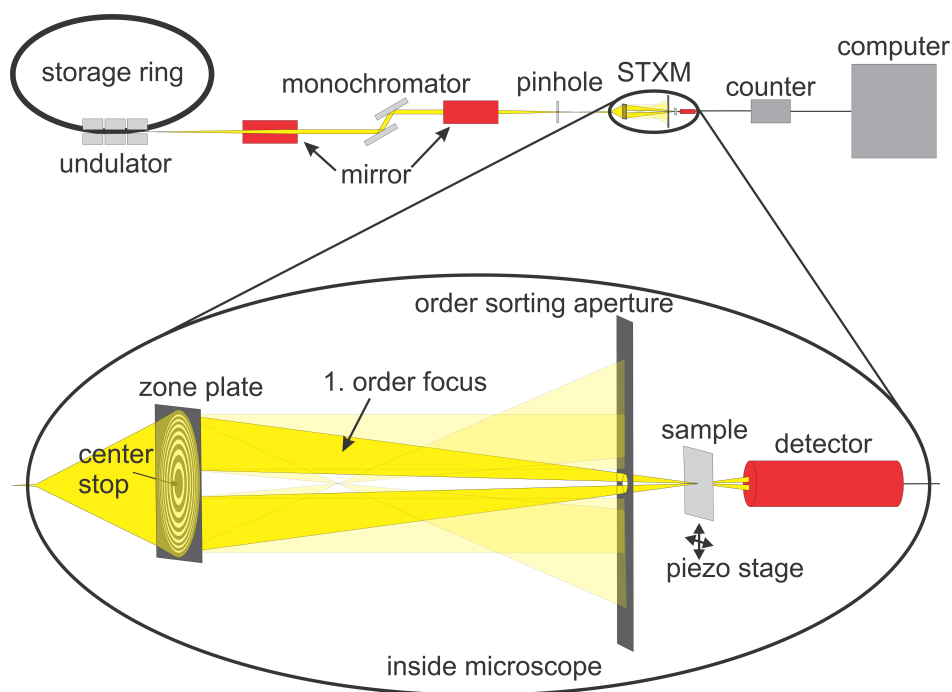

Figure 2.5: Drawing of the MAXYMUS beamline. Overview over the UE46-PGM2 undulator beamline with the MPI-IS UHV-STXM endstation "MAXYMUS", showing the optical path of the X-ray beam and the main working principle of a STXM.

An undulator is an insertion device used at synchrotron radiation sources producing a high photon flux in a narrow energy band [149]. It is built by a periodic structure of alternating dipole magnets, forcing the traversing electrons in the storage ring to undergo oscillations and consequently to emit electro-magnetic waves. The installed undulator covers a soft X-ray energy range from 130-2000 eV. From this energy band, single wave lengths are selected by a so-called collimated plane grating monochromator (PGM) [150]: the first mirror in the optical path, shown in figure 2.5, collimates the light which is then deflected by a tiltable plane mirror, allowing for the variation of the

deflection angle, onto the grating. From here the mono-energetic X-rays are focused by a toroidal mirror onto a pinhole and fed into the STXM, where the beam is focused by a Fresnel zone plate onto the sample, while a center stop in the zone plate blocks the zero order. The zone plate is built by alternating opaque and transparent concentric rings, the Fresnel zones, focusing the light by diffraction around the intransparent zones. The spacing of the zones is designed in a way that a constructive interference occurred at the focus point, whereat the width of the zones has to decrease with increasing distance from the center and the outermost spacing determines the minimal spotsize and therefore limits the resolution of the zone plate. Chao et al. reported on zone plates with outer zones and resolved features as small as 12 nm [151]. Even higher resolution down to the nm-scale might be obtained by Ptychography in the near future, where the diffraction pattern is recorded at every point of the scan and solved for its phase contributions [152, 153, 154]. An order sorting aperture (Osa) between zone plate and sample allows to select the required diffraction order (different diffraction orders are used for different energy ranges) and a fast avalanche photodetector (APD) is used for detecting the transmitted photons. While the positions of the zone plate, Osa and detector are fixed during the measurements, the sample is mounted on a piezo stage to raster it in x- and y-direction, while keeping it in the focus of the X-ray beam. Figure 2.6 shows photographs of the inside of the microscope.
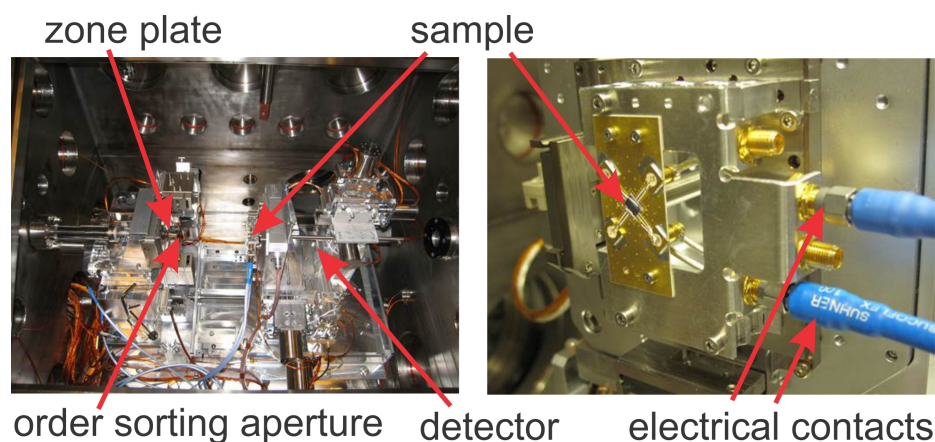

Figure 2.6: Photographs of the interior of the MAXYMUS endstation. The photographs show the UHV-STXM endstation "MAXYMUS" with a built-in sample.

Before the measurements start the right stage with detector and sample is moved closer to the Osa to place the sample in the focus of the X-ray beam, about a millimeter away

from the Osa. What sounds easy, requires a lot of alignment of all components in the optical path before and if necessary realignment during the measurements to obtain a good lateral and chemical resolution, as well as signal-to-noise ratio. Furthermore, suppression of instabilities, such as high and low frequency oscillations as well as beam drifts, is another big issue to conduct successful experiments, which should not further be addressed here.

The STXM main chamber of the used UHV-STXM endstation "MAXYMUS" is connected to a turbo molecular pump, an ion getter pump, a titan sublimation pump and a cryopump to reach and preserve a pressure of $< 1 \cdot 10^{-7}$ mbar during the measurements. After mounting the sample on the sample holder and fixing it in the optical path, the sample can be electrically contacted from the outside of the STXM, by connecting the cables with the vacuum tight electrical feed throughs.

STXM is used in this thesis to follow *in situ* the (de)lithiation of a LFP thin film as a special representative of a multi-particle arrangement (chapter 4), and the phase evolution in a micro-sized battery cell with a single crystalline $LiFePO_4$ cathode, literally made of a single LFP particle (chapter 5). This method is especially eligible due to its high chemical and spatial resolution as well as comparable low dose and good signal to noise ratio with a large field of view at a short measurement time, executed under a clean UHV environment. Compared to frequently used *in situ* XRD measurements reflecting ensemble averages [96, 155], and *in situ* TEM studies probing only a few hundred atoms or when using energy-filtered TEM, rely for a comparable field-of-view, chemical and lateral resolution and signal to noise ratio on a higher dose, more time and sample thicknesses below 50 nm [156, 157], STXM uniquely allows to observe the delithiation/lithiation mechanism in the studied samples with the needed chemical and spatial resolution.

2.3.2 X-ray absorption near edge structure - data analysis

The absorption spectrum at the Fe L edge is characterized by the electron transition from the $2p_{1/2}$ and $2p_{3/2}$ levels to unoccupied 3d states. Therefore the intensity and particularly the position of the L_2 and L_3 absorption feature depend on the occupancy of the d-band and the iron valence state ($Fe^{2+/3+}$), respectively (compare figure 2.7).

Upon delithiation a shift of the L_3 line from around 708 (Fe^{2+}) to 710 eV (Fe^{3+}) is known [155, 158, 159] and used throughout this thesis to fingerprint the change in the (local) state of charge.
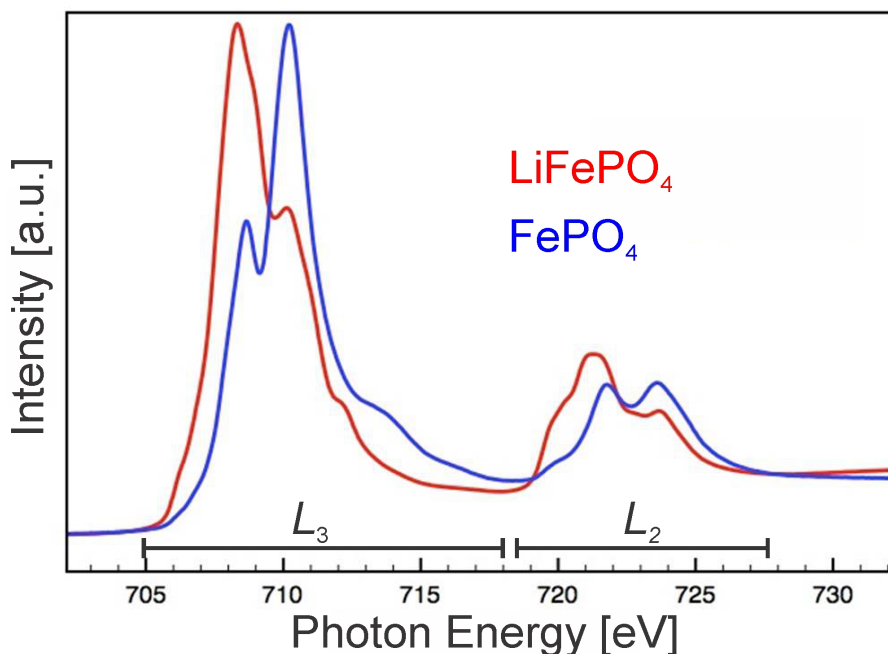

Figure 2.7: X-ray absorption spectrum of LiFePO$_4$ at the Fe $L_{2,3}$ edge. Intensity measured at the ISISS beamline around the Fe $L_{2,3}$ edge as TEY. As reference materials the commercially available LiFePO$_4$ powder for lithium ion power batteries from LinYi Gelon LIB Co.,Ltd, belonging to the Gelon LIB group [160] and a FePO$_4$ powder from Aldrich is used.

Using LFP and FP reference materials, e.g. the ones whose absorption spectra are shown in figure 2.7, the lithium content of the samples are determined by fitting their XANES spectra by a linear combination procedure of the two reference spectra after removal of the background and normalization.

To visualize (de)lithiation kinetics using *in situ* STXM, area scans are performed at single energies before the edge jump (704 eV) and at the centroids of the respective Fe^{2+} (708.7 eV) and Fe^{3+} (710.6 eV) Gaussian XANES contributions, as previously determined by a full absorption spectrum. Using the transmitted intensity at 704 eV as I_0, the intensity of the beam before interaction with the sample, the optical density and absorbance at 708.7 and 710.6 eV can be calculated, respectively. The absorbance is the mathematical quantity given by $A_\lambda = \lg\left(\frac{I_0}{I}\right)$, with I_0 and I being the intensity of the

radiation before (I_0) and after (I) it passed through the sample, respectively.[2] Comparing the absorbance at each point of the sample according to $lg\left(\frac{I_{704}}{I_{708.7}}\right)/lg\left(\frac{I_{704}}{I_{710.6}}\right)$ as a function of time, records the transition between the two oxidation states and therefore the (de)lithiation of $LiFePO_4$.

---

[2]Absorbance does not necessarily measure only the absorption of light; i.e. it can also include effects like light being scattered by a sample (e.g. inside a dispersion). However, these interactions can be excluded for the samples studied in this thesis. Hence, it is a measure for the absorption coefficient of the analyzed samples.

Chapter 3

Cycling of LiFePO$_4$ Powder Electrodes

In this chapter a full battery LFP electrode material, consisting of carbon-coated solvothermally grown LFP, additional carbon additive and a Polyvinyldifluorid (PVDF) binder is analyzed via XRD, XANES, EELS and HRTEM. The aim of this work is to investigate the lithium distribution in differently sized LFP particles within a multi-particle arrangement of a real battery material as a function of the batteries state of charge. The distribution inside the larger particles is compared with the distribution within the small, only some ten nanometer big, particles and is examined using EELS and HRTEM. Furthermore, a combination of surface sensitive total electron yield (TEY) and bulk sensitive fluorescence yield (FY) XANES measurements is used to distinguish between the lithium distribution in the surface and bulk region and gives an insight into the charging mechanism. A turbostratic stacking of layers is found in nanosized particles and identified to be responsible for sluggish lithium insertion and extraction, resulting in a comparibly lower practical capacity during electrochemical cycling than larger particles provide, not exhibiting higher dimensional defects.

3.1 Sample Preparation

3.1.1 Synthesis of powder

The solvothermal synthesized LiFePO$_4$ cathode material has been prepared according to [161]. In a nutshell, metallic lithium has been dissolved in ethanol, equimolar amounts of Fe(II) acetylacetonate and H$_3$PO$_4$, as well as a nitrogen containing carbon precursor to build a N-doped carbon coating on the forming LiFePO$_4$ particles, have been added and the solution has been heated in an autoclave to 200 °C for 24 h under autogenous pressure. The precipitation has been washed with ethanol and heated in a muffle oven to 700 °C for 6 h under nitrogen atmosphere to increase crystallinity and enhance electronic conductivity of the carbon coating. In a last step, the resulting chunks have been ground manually.

Furthermore, commercial FePO$_4$ powder has been purchased from Aldrich as a reference material for the XANES quantification of the FePO$_4$ amount in the cycled material.

3.1.2 Preparation of electrodes

The electrode material is composed of 85 % of the synthesized, carbon coated LiFePO$_4$ powder, 10 % carbon black (Super P - MMM Carbon) to form the electron conducting network and 5 % PVDF, acting as a binder. In a first step, the LFP powder is mixed with carbon black in a mortar for about 15 minutes. Then the PVDF binder is added as a 2.5 % solution with N-methyl pyrrolidone (NMP) as solvent and the suspension is mixed for another 15 minutes to obtain a homogeneous slurry. The subsequent coating of the well-homogenized slurry on a previously cleaned Al current collector foil, using a doctor blade with a spacing of 80 µm, is followed by drying the electrode foil in a vacuum oven at 60 °C for 14 h. Discs with a diameter of 10 mm are punched out of the foil, weighed and transferred to an Ar-atmosphere containing glovebox, where the electrochemical cells are assembled. The active mass for every electrode is calculated from the mass of the punched discs with and without casted electrode material, the amount of carbon coating on the LiFePO$_4$ powder and the mentioned composition of the electrode material (85:10:5).

3.1.3   Cycling of electrodes

Electrochemical charge/discharge measurements have been performed in vacuum tight two-electrode Swagelok-type stainless steel vessels (see figure 3.1), assembled inside an Ar-atmosphere containing glovebox.
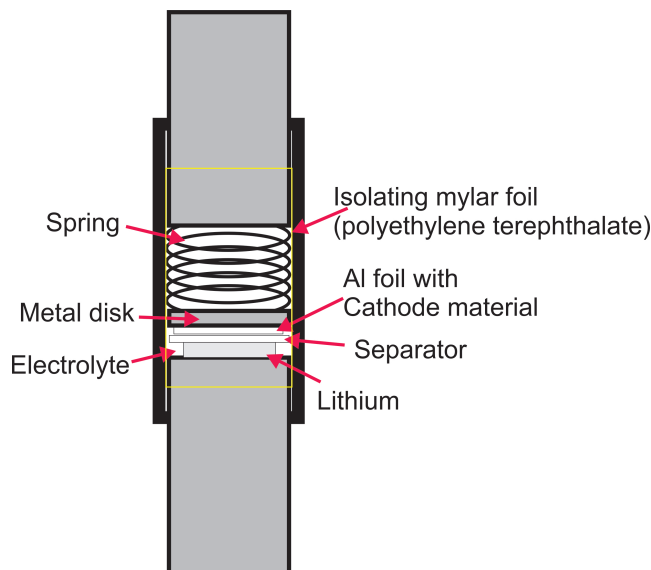

Figure 3.1: Measuring cell for electrochemical tests. Drawing of the battery set-up in a Swagelok-type cell.

The prepared LiFePO$_4$/C disc-electrodes have been used as working electrodes, pure lithium foil from Aldrich as counter and reference electrodes, glass fiber (GF/D) from Whatman as separator, and a 1 M lithium hexafluorophosphate (LiPF$_6$) in ethylene carbonate/dimethyl carbonate solution (EC/DMC, 1:1 by volume) as electrolyte. Using a battery tester BT Pulse from Arbin Instruments, the LFP cathodes have been galvanostatically charged and discharged at a current density of 0.1 C in the potential range between 2.0 and 4.0 V (vs. Li).

3.1.4   Preparation for XANES and EELS measurements

The cycled electrodes are withdrawn from the Swagelok-type cells inside an Ar-atmosphere containing glovebox and cut with a scalpel into two pieces. One of the two pieces is then dipped for 3 seconds in a 1 Vol% NMP in Tetrahydrofuran (THF) solution to dissolve some of the fluoride containing binder and residuals of the electrolyte from the surface to reduce the disturbing overlap upon XAS and EELS investigations of the Fe

L-edge from the cathode material and the F *K*-edge from the binder and electrolyte, respectively. Then both halves are again cut in the middle, so that for both XAS and EELS measurements a dipped and a non-dipped reference of the same electrode is available. For XANES measurements, the sample transfer from the glovebox to the ISISS endstation has been done with a vacuum transfer system to avoid any possible contaminations. The samples for EELS (and HRTEM) measurements are dry deposited onto a C-covered holey copper TEM-grid inside an Ar-atmosphere containing glovebox and the sample transfer to the TEM is done with a vacuum transfer holder.

3.2 Sample Characterization

3.2.1 Compositional characterization by ICP-OES

The as-prepared carbon coated LFP powder has a composition of 85.5 wt% LiFePO$_4$, 12 wt% C and 2.5 wt% N (nitrogen doped carbon coating). The exact cation ratios in the LFP powder are analyzed by ICP-OES using a Spectro Ciros CCD system from Spectro Analytical Instruments, while the oxygen content is determined by the carrier gas hot extraction method. The results are, within the error margins of 1-2 %, in agreement with nominally pure LiFePO$_4$

3.2.2 Morphological characterization by SEM and TEM

The SEM and TEM images shown in figure 3.2 disclose a broad particle size distribution of the active LFP material, as well as different particle morphologies. Such a wide distribution in particle size is not unusual, even for commercially available battery materials, and can also be found e.g. for the LFP powder for lithium ion power batteries from LinYi Gelon LIB Co., Ltd, belonging to the Gelon LIB group [160], exhibiting a granularity of D_{10} > 0.5 µm and D_{90} < 20 µm, respectively.

Hence, the studied powder shows a typical particle size distribution for a full battery electrode material. Furthermore, the TEM image in figure 3.2 nicely shows the carbon matrix, in which the LFP particles are imbedded, ensuring a good electronic contact of all particles.
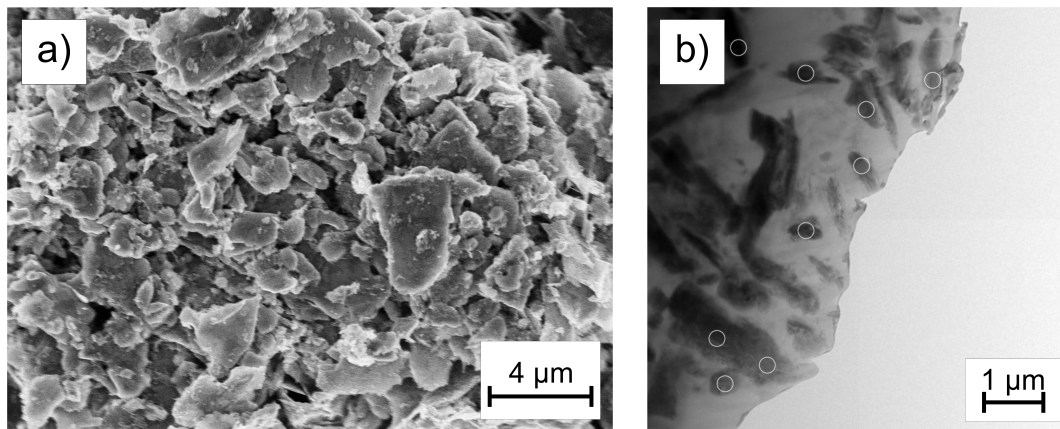
Figure 3.2: SEM/TEM image of the LFP powder. a) SEM image of the as-prepared LFP powder. b) TEM cross-section micrograph of LFP particles from the full LFP electrode. The circles in b) mark some of the studied LFP particles (see figure 3.8).

3.2.3　Electrochemical characterization

Electrochemical charge/discharge measurements have been performed according to subsection 3.1.3, using a battery charger BT Pulse from Arbin Instruments. Furthermore, cyclic voltammetry measurements have been done within the same two-electrode Swagelok-type stainless steel vessels against lithium metal. The shape of such a cyclic voltammogram has mathematically been described by Randles and Sevcik via the following equation [162, 163]

$$\left(\frac{i}{nAFc}\right)\left(\frac{RT}{nF\tilde{D}\nu}\right)^{1/2} = \pi^{1/2}\chi(x) \ \ .$$

(3.1)

Here, i is the faradayic current, n the number of electrons involved in the redox reaction (here: n=1), A the area of the electrode, F the Faraday constant, c the concentration, R the gas constant, T the absolute temperature, $\tilde{D}$ the chemical diffusion coefficient of the electroreducible species, ν the scan rate, and χ a transcendental function, used to express the general form of a voltammogram and whose values are tabulated for different kinds of chemical reactions and particularly for the different characteristic points of a voltammogram [164, 165].[1] If i is limited by the diffusion of the electroac-

---

[1]Interestingly, the Randles-Sevcik function $\sqrt{\pi}\chi(x)$ is identical to the Fermi-Dirac function $\Im_{-3/2}(x)$ [166], having the general form $\Im_k(x) = \frac{1}{\Gamma(k+1)}\int_0^\infty \frac{t^k}{e^{t-x}+1}dt$, being used inter alia for expressing the number of electronic charge carriers in an energy band of a solid (k=1/2).

tive species inside the electrode particles, i.e. fast charge transfer at the electrode - electrolyte interface, plotting the peak currents i_p of several voltammograms, obtained at different scan rates, versus the square root of the scan rate $\nu^{1/2}$, provides, according to equation 3.1, the chemical diffusion coefficient from the slope of the corresponding linear fit. To determine the peak currents, a background current baseline, originating from the ionic double layer at the surface of the electrodes, functioning as a capacitor, is extrapolated to the peak potentials. With a tabulated value of 0.4463 for the transcendental function χ at the peaks of the voltammogram [164], the Randles-Sevcik equation simplifies for T=298 K to

$$ I_p = 2.69 \cdot 10^5 \; \left[\tfrac{As}{molV^{1/2}} \right] \; n^{3/2} AC \left(\nu \tilde{D}_{Li} \right)^{1/2} \; . \tag{3.2} $$

For the measurements presented in figure 3.3 this gives $\tilde{D}_{Li}$=1.24·10^{-10} cm^2/s for the cathodic and $\tilde{D}_{Li}$=8.67·10^{-11} cm^2/s for the anodic chemical diffusion coefficient, respectively. Both values are well within the range of reported lithium diffusion coefficients,
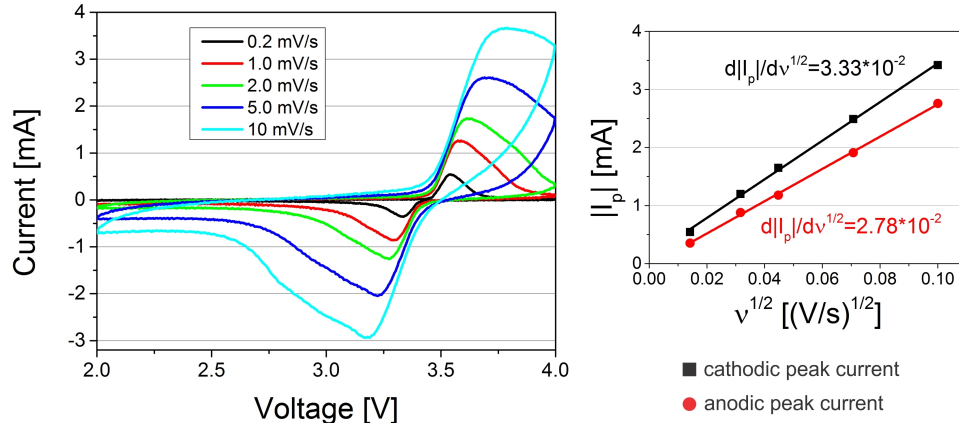

Figure 3.3: Cyclic voltammograms of a LiFePO$_4$ powder electrode. a) Cyclic voltammograms of a LiFePO$_4$ powder electrode, recorded at different scan rates. b) Plot of the cathodic (black) and anodic (red) peak currents vs. the square root of the scan rate $\nu^{1/2}$.

ranging from 10^{-8} cm^2/s to 10^{-16} cm^2/s [88].[2]

---

[2]Note, this method of determining the chemical diffusion coefficient, though widely used in literature, has some general shortcomings: first, the used electrode area does not stringently correlate with the surface of the active particles. Moreover, not all particles participate simultaneously in the lithium exchange, but a particle by particle mechanism is observed and therefore, for slow (dis)charging, most of the particles remain idle. Consequently, the measured (de)lithiation behaviour of the multi-particle system can not be simply transferred to the single-particle scale to determine a materials' prop-

Figure 3.4 a) shows a typical first charge-discharge cycle of one of the prepared LFP electrodes. A charge capacity of 147 mAh/g (average value: 150 ± 12 mAh/g) and a discharge capacity of 129 mAh/g (average value: 126 ± 6 mAh/g) is obtained at a rate of 0.1 C, cycled in a 1 M LiPF$_6$ in EC/DMC electrolyte versus lithium metal. The discrepancies between charge and discharge capacities during the first cycles are already known from literature and mainly attributed to the formation of a solid electrolyte interphase (SEI). After 10 cycles, capacity retention and coulomb efficiency, respectively, reaches already 98 % (compare figure 3.4 b)). Both CV and charge-discharge
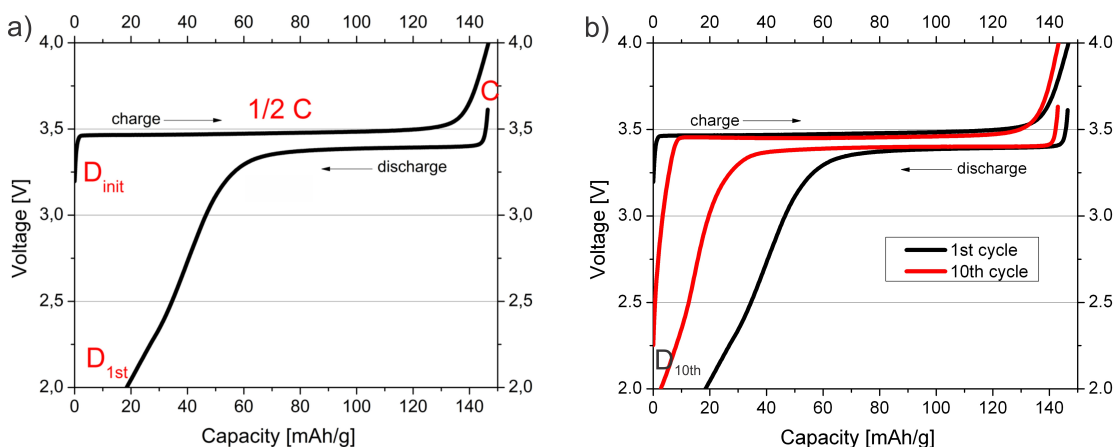
Figure 3.4: Charge-discharge cycle of LFP powder. Charge and discharge capacity of LFP in the first (a) and tenth (b) cycle. Several Electrodes are analyzed by XRD, XANES, EELS ans HRTEM before electrochemical cycling (just assembling and disassembling of Swagelok-cell, D$_{init}$), at half charged state (1/2 C), fully charged (C), fully discharged (D$_{1st}$) and after 10 complete cycles (D$_{10th}$).

experiments indicate that olivine structured LFP is not the only electroactive phase of the cathode material, but an impurity phase, exchanging lithium below 3 V, exists. The capacity of this phase impurity accounts for about 3-4 % of the overall electrode capacity and consequently has no measurable impact on the results, presented in the following sections.

---

erty. Furthermore, the concentration is generally chosen in literature as the lithium concentration in LiFePO$_4$, although the vacancies are the mobile species in the material. The concentration of which depends on the presence of impurities or anti-site disorder [57]. Thus determined chemical diffusion coefficients are therefore only effective values and are estimated here to roughly compare with other literature values and by no means expected to mirror a real materials' property.

3.3 Results

LFP powder electrodes are studied at different state of charge using XRD and HRTEM to investigate changes in the host structure, while XANES and EELS measurements are performed to analyze the changes in the electronic structure, giving information about the lithium content. To do so, the Swagelok-cells are carefully disassembled after the electrochemical cycling, as explained in subsection 3.1.4. The combination of integral methods (XRD, XANES) and lateral resolved methods (HRTEM, EELS) allows to carefully study the complex lithiation process on different scales. Several Electrodes are analyzed before electrochemical cycling (just assembling and disassembling of Swagelok-cell, D_{init}), at half charged state (1/2 C), fully charged (C), fully discharged (D_{1st}) and after 10 complete cycles (D_{10th}). The results are summarized in the following subsections.

3.3.1 Structural investigations - XRD measurements

The XRD measurements are performed on a Bruker AXS D8 Advance diffractometer using a Cu-Kα radiation source. Figure 3.5 shows the XRD pattern of the as-prepared cathode material together with the XRD patterns recorded at the different state of charge (D_{init}, 1/2 C, C and D_{1st}) and reference diffractograms for both LFP and FP. All main diffraction peaks from the as-prepared powder can be assigned to the LFP-related orthorhombic crystal system with space group Pnma(62). Only a small additional peak around 30° indicates the presence of a phase impurity, fitting to the electrochemical measurements.

The cycled electrodes show the expected phase content of LFP and FP at every state of charge (D_{init}, 1/2 C, C and D_{1st}), whereat detailed numbers, obtained by Rietveld analysis on the recorded XRD patterns, are given in table 3.1 in the next subsection, and are discussed together with the expected values from electrochemical cycling and XANES measurements. The obtained lattice parameters from Rietveld analysis are in agreement with a 2-phase reaction mechanism, i.e. they are independent of the batteries' state of charge (differences below 0.1 %), and determined to be for the LFP phase 10.321 (**a**), 6.001 (**b**) and 4.691 (**c**) and for the FP phase 9.812 (**a**), 5.791 (**b**)
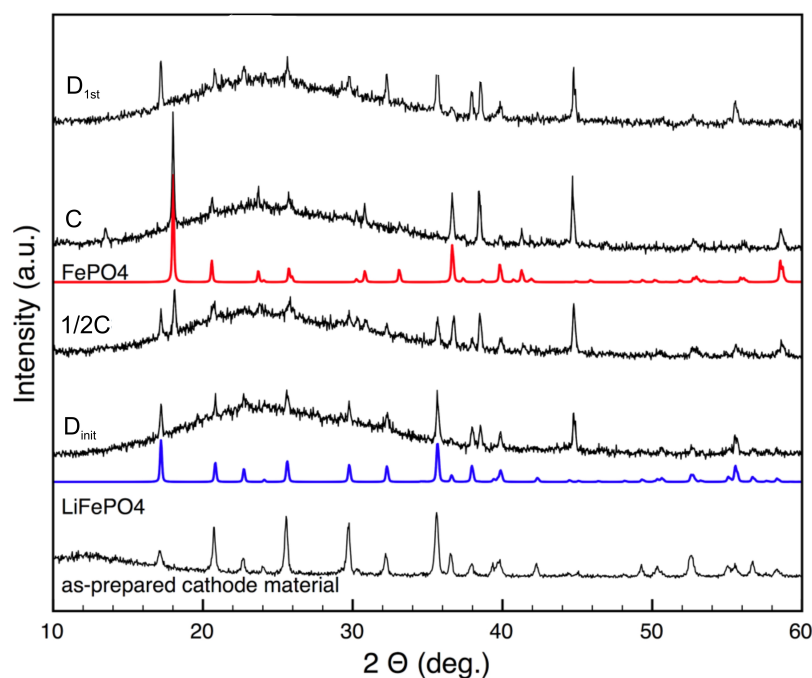
Figure 3.5: XRD pattern of differently cycled LiFePO$_4$ powder electrodes.
The XRD pattern of the as-prepared cathode material is plotted together with the
patterns of the initial electrode material, as well as with the half charged, fully charged
and fully discharged samples. Furthermore reference diffractograms for both LFP and
FP are shown (according to [167]).

and 4.784 (**c**).

3.3.2   Bulk and surface lithium concentration - XANES measurements

XANES measurements are done at the synchrotron radiation facility HZB/BESSY II
in Berlin at the ISISS beamline (compare section 2.3). Fe $L_{2,3}$ edge spectra are recorded
at energies of 705-730 eV to track the change in the iron oxidation state and lithium
concentration within the LFP cathode material, respectively. The shift in the main
absorption feature upon (de)lithiation is used to quantify the change in Fe^{2+}, Fe^{3+} and
the corresponding lithium concentration (compare subsection 2.3.2).[3] Both surface
sensitive TEY and bulk sensitive FY absorption measurements are carried out to dis-
tinguish between the lithium concentration within the surface and the bulk of the LFP

---

[3]A direct study of the Li K edge (around 55 eV [168]) is not possible due to an insufficient energy
resolution and overlap with the Fe M edge (around 54 eV [168]).

particles. Figure 3.6 shows the recorded TEY (a) and FY (b) spectra of the differently cycled electrodes. The difference in the spectral shape of TEY and FY measurements results from self-absorption of the emitted photons, generating the FY signal, while travelling through the solid, leading to a blurring of the FY spectrum.
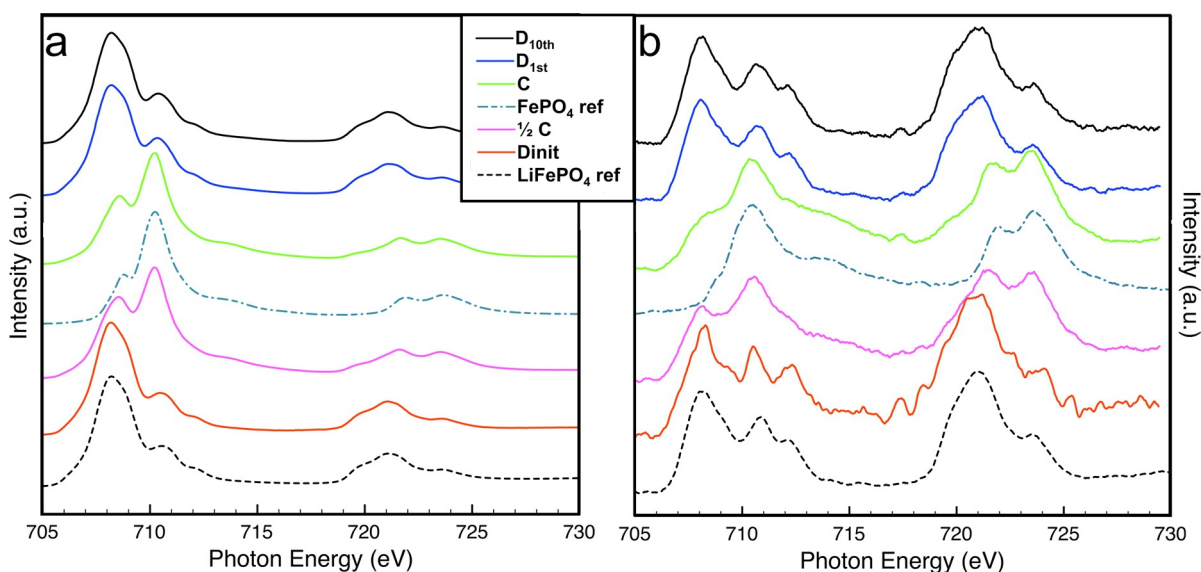

Figure 3.6: XANES spectra of cycled electrodes. Fe $L_{2,3}$ TEY (a) and FY (b) XANES spectra of the cycled LFP cathodes, plotted together with the LFP and FP references (according to [167]).

The LFP and FP contents of the differently cycled electrodes are determined after background removal and normalization of the spectra to the edge jump by fitting them with a linear combination of a FP reference spectra (material purchased from Aldrich) and the spectrum from the initial, uncycled LFP electrode. Table 3.1 lists the LFP and FP concentrations in the cycled LFP electrodes as expected by electrochemical cycling (EC) and determined by XRD and XANES measurements.

The deviation from 100 % FP in the charged state (C) and 100 % LFP in the discharged state (D_{1st}) for the values obtained from electrochemical cycling, results from the achieved respective capacities, deviating from the theoretical capacity of LiFePO₄ of 170 mAh/g. Interestingly, the XRD measurements show for the fully charged state a pure FP phase and for the fully discharged state (D_{1st}) a pure LFP phase. This is not a contradiction, since XRD gives the amount of crystallographic phase content of Li_xFePO_4 and $Li_{1-y}FePO_4$ in the sample, which is not directly correlated to the lithium concentration in the cathode material due to the unknown lithium con-

measurement mode	EC		XRD		XANES (FY)		XANES (TEY)	
state of charge	LFP	FP	LFP	FP	LFP	FP	LFP	FP
D$_{init}$	100	0	100	0	100	0	100	0
1/2 C	50	50	49	51	46	54	36	64
C	12	88	0	100	27	73	25	75
D$_{1st}$	86	14	100	0	96	4	89	11

Table 3.1: Quantification of LFP and FP content in cycled electrodes. LFP and FP concentration in the cycled LFP electrodes as expected by electrochemical cycling (EC) and determined by XRD (crystallographic phase content) and XANES (Fe$^{2+/3+}$ concentration), given in %.

tent in the boundary phases and due to the solubility of both phases in each other. Moreover, it should be kept in mind, that most of the XRD signal comes from large, well-crystallized particles, while this method is not very sensitive to nanosized particles. Hence, the XRD results indicate, that the vast majority of the big LFP particles have participated in the charge and discharge process of the battery, while they do not provide information about the total lithium concentration in the electrode at different states of charge. A more direct measure for the lithium content in the active material is given by the XANES measurements. These provide for the charged state a lithium content of 25 % (TEY) and 27 % (FY), respectively, while the determined lithium concentration in the electrodes after a complete cycle is again in agreement with the expectation from electrochemical cycling. The lithium content in the fully charged electrode, being higher than expected from electrochemical current integration, can be understood in terms of SEI formation on the lithium anode. Thus, a part of the current in the first cycle is generated by electrolyte decomposition at the anode. A look at the charge-discharge curves, shown in figure 3.4, reveals a current flow at voltages higher than the horizontal plateau, at the end of the charging process, equivalent to a capacity of about 15 mAh/g, corresponding to 9 % lithium exchange. Therefore, the lithium content determined by XANES measurements fits, within the error margins, to the expected content determined by electrochemical cycling, when SEI formation is taken into account. Interestingly, the TEY and FY results for the half charged sample (1/2 C) differ by 10 % from each other, i.e. upon charging the LFP electrode material, the surface layer of the particles is delithiated faster than the core. This fits to the delithiation behaviour observed by Sigle et al., namely that delithiation of large LFP

crystals proceeds via delithiation of the surface-near region [169].

3.3.3 Lithium distribution as function of particle size - EELS measurements

To study the lithium content of differently sized, individual particles, an image-corrected FEI 80-300 Cs TITAN TEM is used and EELS spectra acquired using a postcolumn GIF Tridiem Filter, exhibiting an energy resolution of 0.8 eV. The measurements are performed at acceleration voltages of 80 and 300 keV, respectively, whereat special care has been taken to exclude possible beam damage on the samples (more details can be found in [167]). Figure 3.7 shows for differently cycled electrodes, EELS spectra of particles smaller than 100 nm and compares them to the corresponding XANES (TEY) measurements.
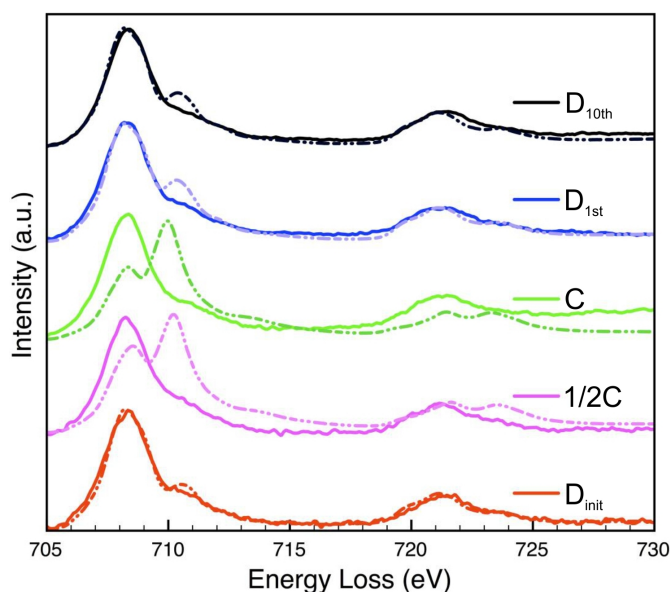
Figure 3.7: EELS spectra of particles smaller 100 nm. The solid lines are Fe $L_{2,3}$ EELS spectra of particles smaller than 100 nm. They are recorded at different states of charge of the battery and compared with the respective XANES (TEY) measurements (dotted lines).

As can be seen, the EELS spectra of all analyzed particles show only a Fe^{2+} contribution, independent of the state of charge of the associated electrode. This suggests that the nanosized particles in the LFP cathode material behave significantly different than the average electrode particle, i.e. they do not get delithiated and do not participate in

lithium exchange upon cycling, respectively. To ensure that this finding is not an artifact, maybe originating from the particle by particle (de)lithiation mechanism or some unknown measurement error, several particles of different sizes from the completely charged electrode material (charge state C) are analyzed. Some of the corresponding EELS spectra are shown in figure 3.8, representative for all analyzed particles.
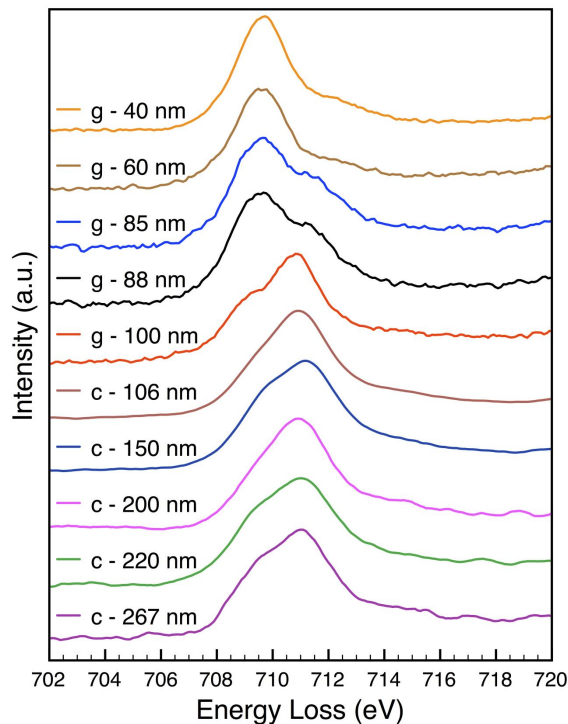

Figure 3.8: EELS spectra of differently sized particles. All analyzed particles are from the completely charged electrode (charge state C). Particles from the sample prepared in the glovebox and measured at 80 keV are labeled as "g", and cross-section prepared samples, measured at 300 keV are labeled as "c". Reprinted from [167].

A clear trend of increasing Fe^{3+} contribution with increasing particle size is found in the EELS spectra, whereat the biggest change in Fe^{2+} and Fe^{3+} contribution is found for particles around 100 nm in size. This proves the different cycling behaviour of differently sized particles within the same electrode, whereby the nanosized particles seem not to participate in the cycling at all.

3.3.4   Higher dimensional defects - HRTEM measurements

To elucidate the origin of the different cycling behaviour of differently sized particles within the same electrode, HRTEM measurements are performed on several particles

of various sizes. Figure 3.9 shows representative HRTEM images of a nanosized LFP crystallite.
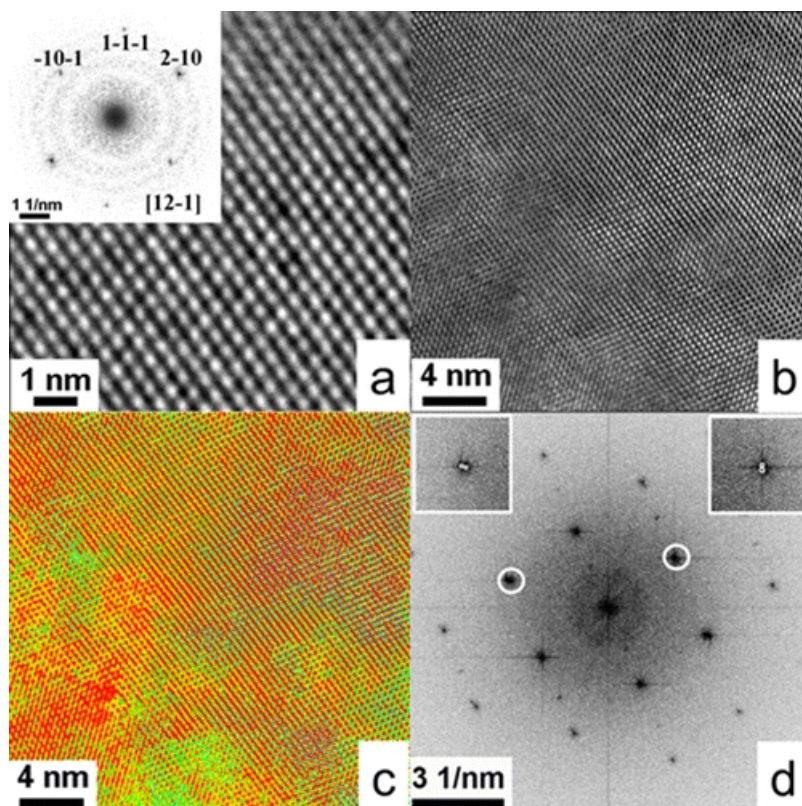

Figure 3.9: HRTEM image of a nanosized LFP crystallite. a) HRTEM of a small olivine-structured LFP crystallite, revealing point defects in the Li$_x$FePO$_4$ lattice. b) Turbostratic stacking of layers visible through non-periodic contrast variation. c) Colour coded representation of b). d) Fourier transformation of b) with an inset of the "split" diffraction spots, reflecting the turbostratic arrangement. Reprinted from [167].

The lattice fringe image, shown in figure 3.9 b), reveals a non-periodic contrast variation, originating from turbostratic stacking of LFP layers in the crystal. To visualize this defects and alterations from the perfect crystal structure, respectively, the same image is color-coded and replotted in figure 3.9 c). Additionally, the power spectrum (Fourier transformed) of this HRTEM image is plotted in figure 3.9 d), where a variation, i.e. "split", of diffraction spot positions can be seen in the small insets. These "double spots" are indicative for a turbostratic stacking and rotational disorder, respectively, of LFP layers within the particle. The analysis of the Fourier transformed image indicates for this nanosized LFP crystallite a rotational disorder along [101] between 0.4 and 0.9°, whereat also other rotational disorders are found in other nanosized

LFP particles. For the larger particles such higher dimensional structural defects could not be found, but instead they are mostly well crystallized. Figure 3.10 shows HRTEM images of the small (a,b) and of a representative larger LFP particle (c,d) in greyscale, as well as color coded. The gradual variations in the greyscale and color for the large
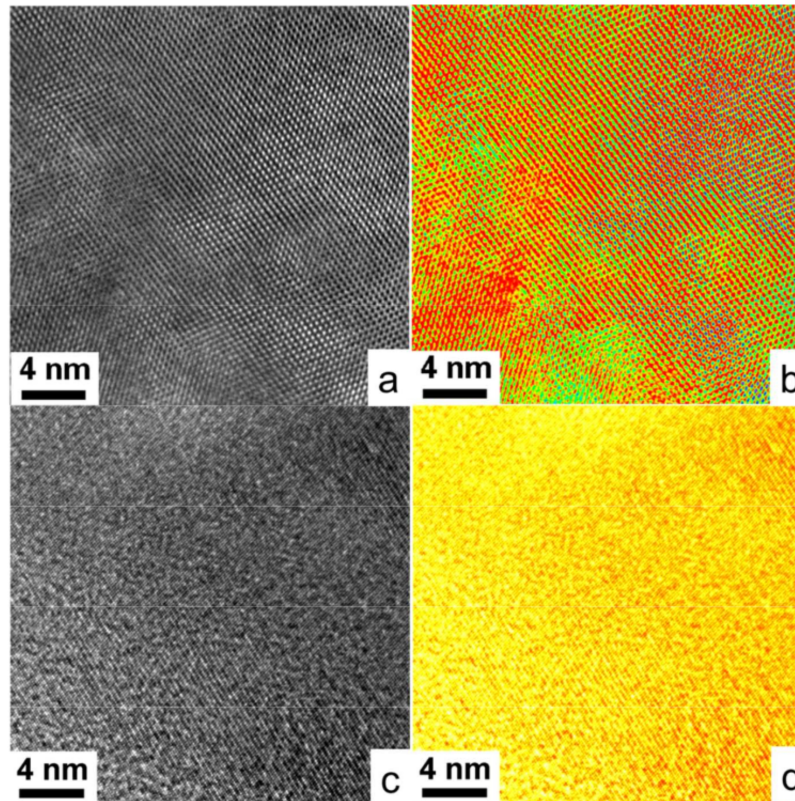

Figure 3.10: HRTEM of LFP crystallites. HRTEM of nanosized (a, b) LiFePO$_4$ particles and large (c, d) crystallites in comparison. Reprinted from [167].

LFP particle can be assigned to a gradual thickness variation, while the non-monotone, non-periodic contrast variation for the nanosized particle results from the mentioned rotational disorder. These higher dimensional defects are predominantly found in nanosized particles and are identified to be responsible for the sluggish lithium exchange, because a rotational disorder in the particle can block the 1-dimensional channels for lithium transport, as well as impair the transport along the other directions, leading to a "trapping" of lithium in the lattice.

In a nutshell: while the obtained results are in agreement with a 2-phase mechanism (XRD), as already proposed by Padhi et al. [24], and with a core-shell structure of the active particles (XANES), as already reported by Sigle et al. [169], EELS measure-

ments indicate that, within the studied full electrode material with a broad particle size distribution, particles smaller than 100 nm show a different cycling behaviour and seem not to participate in the charging process at all. This is totally unexpected since the lithium chemical potential within the particles μ_{Li} is given by the bulk value μ_{Li}^{∞} plus a term proportional to the surface energy γ divided by the particles' radius r ($\mu_{Li} = \mu_{Li}^{\infty} + \frac{2\gamma}{r}V_m$, V_m molar volume). Hence, μ_{Li} is larger for smaller particles, so that these should delithiate first. A comparative study of particles of different sizes by HRTEM identifies a turbostratic stacking of layers in the nanosized particles as the origin of this loss in practical capacity, due to a disturbance and eventually blocking of the 1-dimensional lithium transport channels in the olivine structure, giving a striking example for the importance of defect chemistry on the (de)lithiation mechanism. A possible explanation, why these higher dimensional defects are only present in small particles (< 100 nm), may be found in the synthesis of the LFP powder, favoring the growth of particles without higher dimensional defective structures.

Chapter 4

In situ Observation of Lithiating a Li$_x$FePO$_4$ Thin Film

In this chapter, the work carried out on a newly designed and fabricated all-solid-state thin film micro battery using LiFePO$_4$ as cathode, Li$_{3.5}$V$_{0.5}$Si$_{0.5}$O$_4$ (LVSO) as electrolyte and a lithium aluminum alloy (LiAl) as anode material is presented. All three layers are grown by pulsed laser deposition. Compared to other thin film solid-state electrochemical cells presented in literature [114, 170, 171, 172], this concept does not have simply anode, electrolyte, and cathode stacked on top of each other on the substrate. Instead, a geometry which is rotated by 90° compared to typical solid-state electrochemical cells is employed, so that a lateral design concept results, in which the overall Li transport path is oriented along the substrate's surface. Using a X-ray transparent Si$_3$N$_4$ membrane as substrate, this geometry makes it possible to use STXM to follow *in situ* the (de)lithiation of Li$_x$FePO$_4$ within the multi-grain LFP thin film cathode by studying the shift in the Fe *L*-edge upon lithium exchange. The observed initial lithiation process does not follow the classical particle by particle mechanism as described by Dreyer et al. [99], but instead a rather simultaneous albeit inhomogeneous lithiation is observed.

4.1 Sample Preparation

4.1.1 Synthesis of powder and preparation of targets

$LiFePO_4$

$LiFePO_4$ powder is synthesized using an aqueous solution route, mixing equimolar amounts of $Fe(NO_3)_3 \cdot 9H_20$ (99.99 %, Aldrich) and LiH_2PO_4 (99.99 %, Aldrich). Under continuous stirring on a hot plate the water is evaporated upon release of nitrous fumes, whereat a temperature of $> 100\,°C$ is avoided at the end of evaporation to protect from splashing. The obtained white powder is milled in a mortar and immediately heated to $300\,°C$ for 3 h inside an Al_2O_3 crucible in an Ar atmosphere containing 5 % H_2. The resulting brownish powder is again milled and then isostatically pressed into a pellet using rubber forms and a pressure of about 300 MPa. These pellets are sintered under Ar/H_2 atmosphere (95/5 Vol%) at $500\,°C$ for 12 h and show a grey colour after the heat treatment.

To prepare the targets for PLD the pellets are grinded in a mortar and the fine powder is isostatically pressed into a new pellet at a pressure of 600 MPa, followed by a 2 h heat treatment at $600\,°C$ under Ar/H_2 (95/5 Vol%) atmosphere. The pellets have a diameter of about 11 mm, a height of about 5 mm and a density of about 68 %, which is slightly higher than what is reported by Sauvage et al. for their $LiFePO_4$ PLD targets [173]. They are glued onto a stainless steel target holder with a silver epoxy glue and subsequently stored in an desiccator.

LVSO

The electrolyte material with the nominal composition $Li_{3.5}V_{0.5}Si_{0.5}O_4$, being a solid solution of Li_4SiO_4 and Li_3VO_4, is synthesized by a solid-state reaction method mixing equimolar amounts of Li_2CO_3 (99.99 %, Aldrich), SiO_2 (99.9 %, Aldrich) and V_2O_5 (99.99 %, Aldrich) according to [174, 175]. After mixing the powder in a ball mill with acetone, it is dried and heated to $750\,°C$ in air inside an Al_2O_3 crucible for 24 h to convert Li_2CO_3 to Li_2O and to form the solid solution. After the reaction the powder is milled in a mortar and then isostatically pressed into pellets using rubber forms and a pressure of about 600 MPa, followed by a 4 h heat treatment at $800\,°C$ in air. The

resulting pellets have a diameter of about 10 mm, a height of about 5 mm and a density of about 82 %. They are glued onto a stainless steel target holder with a silver epoxy glue and stored together with the LFP targets in an excicator.

LiAl

LiAl alloy with a molar ratio of 1:1 has been bought as a powder (99.9 %, ELSAmetal) and directly pressed into a pellet at a pressure of 600 MPa, whereat the rubber forms have been filled, sealed and reopened after the pressing inside an Ar-atmosphere glovebox. The pellets have a similar size as the LFP and LVSO pellets and are as well glued onto a stainless steel target holder with a silver epoxy glue, again under Ar-atmosphere. The powder as well as the targets are stored in an Ar-atmosphere glovebox and transferred to the PLD chamber under argon atmosphere to prevent reactions with air and to ensure a target surface as clean as possible.

4.1.2   Thin film deposition by PLD

The importance of various parameters in PLD on the film quality and composition has already been described in section 2.1. Here the parameters for growing LFP, LVSO and LiAl films, found to be optimal for the given PLD system using a KrF excimer laser with a wave length of 248 nm, are listed. For all films freshly polished targets are used. Furthermore all substrates are polished and cleaned in acetone in an ultrasonic bath for 10 minutes before placing in the PLD chamber. Only the fragile Si_3N_4 membranes, which are single packed under clean room conditions by the producer, being used as substrates for the thin film batteries, are used without further treatment.

The deposition procedure starts for all materials with an evacuation of the chamber for about 2 h, meanwhile temporarily flooding the chamber with the process gas to get rid of adsorbed water inside. The pressure is kept constant at the respective deposition pressure during heating, deposition and cooling by a combination of pumping and a continuous flow of process gas into the chamber. After heating the substrate to deposition temperature, the temperature is hold for at least 1 h to equilibrate before the deposition starts. After deposition and cooling, the chamber is flooded with argon and both sample and target are removed.

LiFePO$_4$

The optimized parameters, in terms of phase purity, crystallinity and electrochemical performance, for the growth of LiFePO$_4$ via PLD are summarized in table 4.1. Similar parameters have already been reported in literature for LFP deposition using other PLD-systems (compare e.g. [47, 176]).

Parameter	Value
Rotational speed of target	$> 90/s$
Distance target - substrate	30 mm
Substrate materials	Si (100), Nb:STO (100), Ti, Si$_3$N$_4$
Substrate sizes	(10x10x0.5) mm, (5x5x0.5) mm
Base pressure	$\approx 10^{-3}$ mbar
Process gas	Argon
Deposition pressure	0.2 mbar
Flow rate	≈ 3 sccm/s
Deposition temperature at substrate	525 °C
Equilibration time before deposition	1 h
Heating rate	20 °C/min up to 250 °C
	10 °C up to 525 °C
Cooling rate	5 °C/min down to 250 °C
	10 °C/min down to room temperature
Laser energy (density at target)	75 mJ (1.3 J/cm^2)
Laser frequency	5 Hz
Pulse duration	~ 10 ns
Laser pulses with closed shutter	600
Growth rate	≈ 0.10 Å/ pulse
	(from SEM cross section measurements)

Table 4.1: PLD parameters for LFP deposition. This table lists the used PLD parameters for depositing LiFePO$_4$. The given heating/cooling procedure is especially important when using Si$_3$N$_4$ membranes as substrate, to ensure membrane stability.

The main challenge in depositing LFP in the available PLD quartz glass chamber is, that the used PLD set-up is not totally gas-tight and has a leakage rate of about $Q = 3 \cdot 10^{-4}$ mbar·L/s [1], respectively, so that air and therefore small amounts of oxygen pour into it. While this is not a fundamental problem for synthesizing oxygen materials, the iron in LiFePO$_4$ is easily oxidized to Fe^{3+}, following e.g. the reaction $12LiFePO_4 + 3O_2 \rightarrow 4Li_3Fe_2(PO_4)_3 + 2Fe_2O_3$ [178], making it impossible to form pure olivine structured LiFePO$_4$. This inflow of oxygen is enough to oxidize all of the

---

[1]According to [177] a vacuum chamber is very close for Q $< 10^{-6}$ mbar L/s, sufficiently close for Q $< 10^{-5}$ mbar·L/s and leak for Q $> 10^{-4}$ mbar·L/s.

deposited Fe^{2+}. The use of KF flanges, which are limited by the o-rings' properties, is identified to be the weak point of the recipient. However, the quartz glass chamber can only be used with KF flanges, becoming noticeable leaky at elevated substrate and correspondent chamber temperatures. Trying simultaneous evaporation of lithium during deposition and changing the process gas to 5 % (Ar/H$_2$) has not brought the expected results. However, a freshly polished titanium metal plate, placed on top of the heater inside the chamber, thus having a temperature of about 750 °C during deposition (at 525 °C substrate temperature), functions as a getter and enables the growth of LiFePO$_4$ thin films.

LVSO

The used parameters for depositing LVSO via PLD are summarized in table 4.2 and are similar to the parameters reported by Kawamura et al. for room temperature deposition of LVSO via PLD [179].

Parameter	Value
Rotational speed of target	$> 90/s$
Distance target - substrate	30 mm
Substrate materials	Si (100), Ti-covered LFP, Si$_3$N$_4$, MgO (110)
Substrate sizes	(5x5x0.5) mm
Base pressure	$\approx 10^{-3}$ mbar
Process gas	Oxygen
Deposition pressure	0.03 mbar
Flow rate	≈ 1.7 sccm/s
Deposition temperature at substrate	Room temperature
Laser energy (density at target)	80 mJ (1.4 J/cm^2)
Laser frequency	5 Hz
Pulse duration	~ 10 ns
Laser pulses with closed shutter	600
Growth rate	≈ 1.21 Å/ pulse
	(from SEM cross section measurements)

Table 4.2: PLD parameters for LVSO deposition. This table lists the used PLD parameters for depositing LVSO.

Upon fabricating the all-solid-state thin film battery, the LVSO electrolyte layer is deposited after the LFP cathode. This leads to a constraint in the usable deposition temperature since the predeposited LFP-layer would be oxidized at elevated temperatures in an oxygen containing atmosphere, as it is used for the deposition of LVSO.

Hence, although the deposition of LVSO at elevated temperatures or alternatively a subsequent heat-treatment of the deposited thin film generally is beneficial in terms of morphology and ionic conductivity [174, 175, 179, 180], the LVSO thin film used as electrolyte in the all-solid-state thin film battery is deposited at room temperature, forming an amorphous lithium ion conductor.

LiAl

Table 4.3 summarizes the used parameters for the deposition of LiAl thin films via PLD.

Parameter	Value
Rotational speed of target	$> 90/s$
Distance target - substrate	30 mm
Substrate materials	Si (100), Nb:STO (100), Ti, Si_3N_4
Substrate sizes	(5x5x0.5) mm
Base pressure	$\approx 10^{-3}$ mbar
Process gas	Argon
Deposition pressure	0.1 mbar
Flow rate	≈ 0.6 sccm/s
Deposition temperature at substrate	Room temperature
Laser energy (density at target)	80 mJ (1.4 J/cm^2)
Laser frequency	5 Hz
Pulse duration	~ 10 ns
Laser pulses with closed shutter	600
Growth rate	≈ 0.35 Å/ pulse (from SEM cross section measurements)

Table 4.3: PLD parameters for LiAl deposition. This table lists the used PLD parameters for depositing LiAl.

The parameters have not been intensively optimized, since the paramount requirement for the anode material in the fabricated thin film battery is to provide a sufficient reservoir for the uptake and release of lithium, rather than being phase pure, specifically crystalline, providing a certain morphology or showing the maximum possible electronic and ionic conductivity. Furthermore, the exact ratio of lithium to aluminum in the deposited film does not play a decisive role, since in principle also a pure aluminum and pure lithium anode would fulfill the requirement to take up all the lithium from

the LFP cathode, respectively.[2] However, a ratio between 0.1:1 and 0.9:1 (Li:Al) would be optimal to sufficiently cycle the anode within the $(\alpha + \beta)$ two-phase region of the Li-Al phase diagram, which ranges at room temperature from close to 0 up to 50 at.% lithium [181, 182]. In this $(\alpha + \beta)$ region the Li-Al alloy is typically cycled, exhibiting a voltage plateau of about 350 mV vs. lithium metal [183]. Additionally, the LiAl thin film is made sufficiently thick to reliably work as a reservoir for the uptake and release of lithium in the all-solid-state thin film micro battery (see sections 4.2.4 and 4.3). Nevertheless, great attention has been paid such that target, deposited LiAl thin films and assembled thin film batteries do not get in touch with air and the contact time is minimized, respectively, to prevent possible reactions with oxygen, nitrogen and air humidity, being by far more important than precisely tuned deposition parameters.

4.2 Powder and Thin Film Characterization

4.2.1 Structural characterization by XRD and Raman

X-ray diffraction and Raman spectroscopy have been used to characterize the LiFePO$_4$ powder and thin films as well as the LVSO target. Most of the standard powder XRD measurements have been carried out at room temperature on a Philips PW 3710 diffractometer with a Cu-Kα radiation source, while the diffractograms of the thin films have been taken with a Philips MRD instrument, using a Co-Kα radiation source, under grazing incidence (GIXRD) of $\Omega = 2°$ with steps of $0.02°$ and a detection time of 18 s/step.

The Raman measurements have been performed at room temperature in a quasi-backscattering geometry on a Jobin Yvon Typ V 010 single grating spectrometer, equipped with a double razor edge filter and a CCD camera, offering a resolution of 1 cm^{-1} with the used grating of 1800 lines/mm. The spectra have been taken using the 632.817 nm line of a He/Ne gas laser, having a power < 1 mW, focused through a 50x microscope objective onto the samples surface to a 5 µm spot.

---

[2]Howbeit, pure aluminum shows a poor reversibility upon lithium uptake and pure lithium is very sensitive to oxygen, air humidity and especially nitrogen, making it more difficult to handle.

LiFePO$_4$

Typical X-ray diffractograms of LFP powder used for preparation of the PLD targets and of 300 nm thick LFP thin films deposited on different substrates under the same deposition conditions (compare subsection 4.1.2) are shown in figure 4.1.
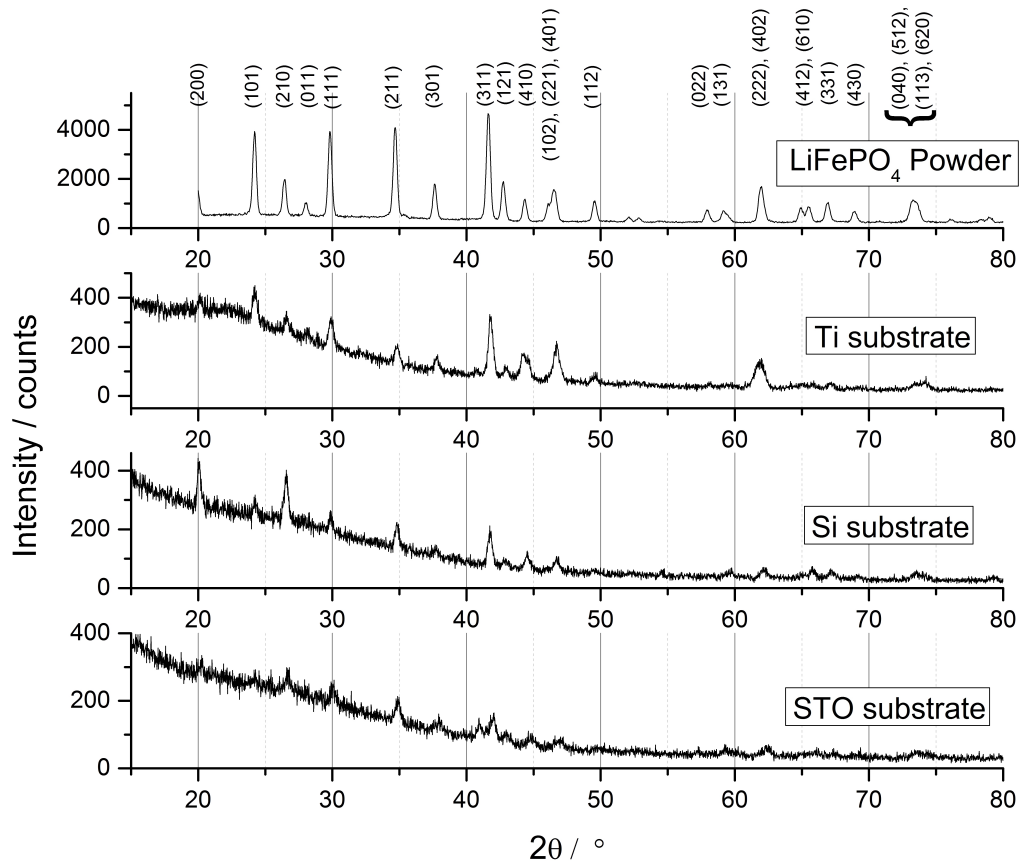

Figure 4.1: X-ray diffractograms of LFP powder and thin films. Room temperature X-ray diffractogram of LiFePO$_4$ powder and LFP thin films deposited with PLD on titanium, silicon (100) and Nb:STO (100) substrates. The peaks are indexed based on the orthorhombic crystal system with space group Pnma(62).

All diffraction peaks from the powder measurements can be assigned to the LFP-related orthorhombic crystal system with space group Pnma(62), proving a high phase purity. Furthermore, also all the diffraction peaks of the dense 300 nm thick films, deposited via PLD, can be assigned to the relevant crystal system without phase impurities like LiFeP$_2$O$_7$, Fe$_4$(P$_2$O$_7$)$_3$, Li$_3$Fe$_2$(PO$_4$)$_3$, Fe$_2$O$_3$ or other impurities that have been reported in literature for deposited LFP thin films [176, 178, 184]. As expected, by comparing X-ray diffractograms of LFP thin films from literature [44, 47, 157, 176], the

texture of the PLD-grown crystalline LFP thin films depends on the substrate material with different pronounced orientations, but in all cases without any XRD-detectable impurities. While the LFP thin films on Si (100) and non-oriented Titanium substrates exhibit a nice crystallinity and high phase purity, the films on Nb:STO do not show such pronounced peaks, indicating a not well crystallized material. Additionally to the XRD measurements, Raman spectra have been taken from the LFP target material, shown in figure 4.2.
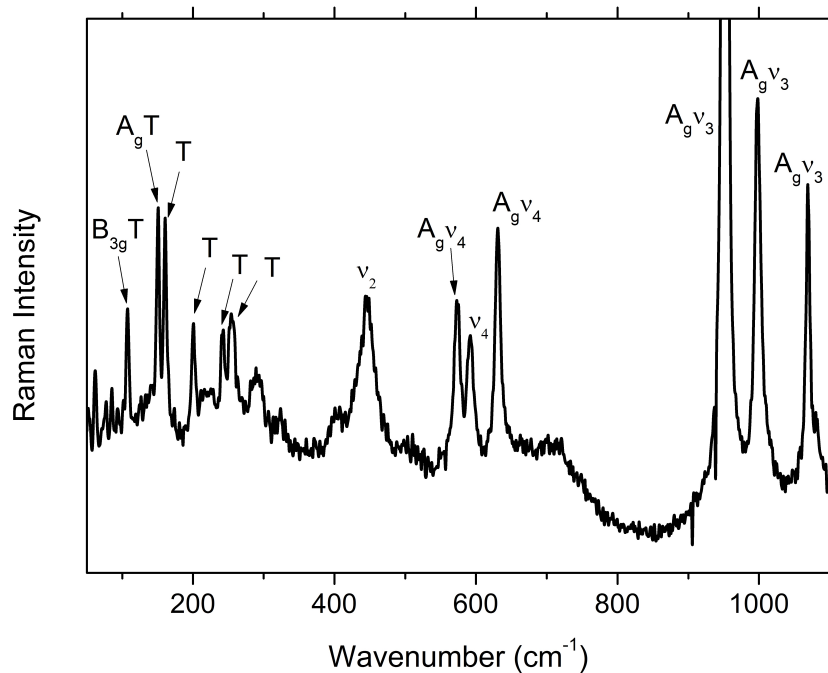
Figure 4.2: Raman spectrum of LFP. Unpolarized Raman spectrum of the LFP target material. The main peaks are indexed according to [185].

The modes in the unpolarized Raman spectrum of the target material are indexed according to [185], demonstrating that all pronounced peaks correspond to resonances of LFP. Especially, no peak around 670 cm^{-1} is found, indicating iron oxide species, easily developing upon heat treatment of the powder during synthesis.

LVSO

Figure 4.3 shows the X-ray diffractogram of a finalized pressed and sintered LVSO pellet as described in section 4.1.1. The main diffraction peaks are indexed according to reference [174], where a Li$_{3.4}$V$_{0.6}$Si$_{0.4}$O$_4$ powder was analyzed, documenting the

successful solid-state reaction of Li_2CO_3, SiO_2 and V_2O_5 forming a Li_2O-SiO_2-V_2O_5 solid solution as described in subsection 4.1.1. The LVSO thin film deposition is carried out at room temperature, resulting in X-ray amorphous films.
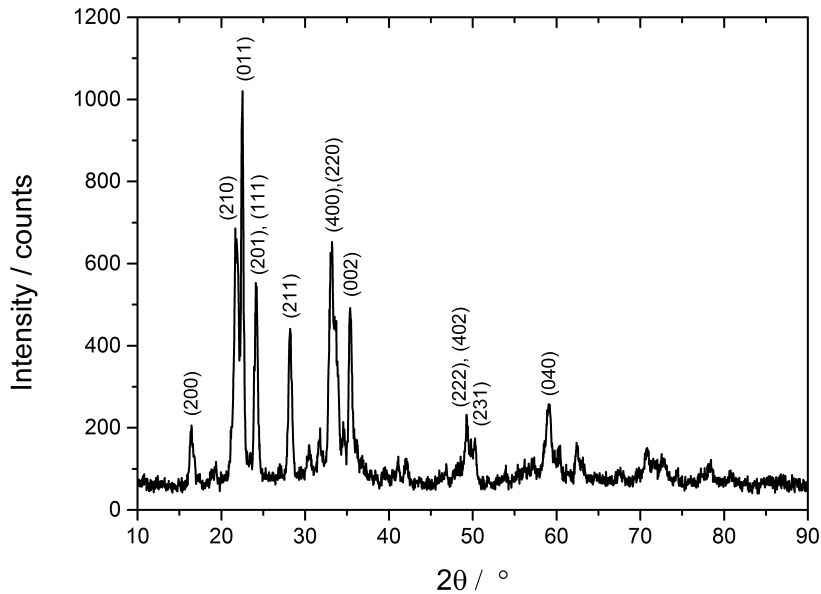
Figure 4.3: XRD of the LVSO target. Room temperature X-ray diffractogram of the $Li_{3.5}V_{0.5}Si_{0.5}O_4$ PLD target. The main peaks are indexed based on reference [174].

Additionally, the exact chemical composition of the LVSO target material and the thin films has been analyzed using Inductively Coupled Plasma - Optical Emission Spectrometry (ICP-OES) and the results are shown together with the ICP-OES results for the LFP target and thin films in the next subsection.

4.2.2 Compositional characterization by ICP-OES and SIMS

The exact cation ratios in LFP and LVSO powders and thin films are analyzed by ICP-OES using a Spectro Ciros CCD system from Spectro Analytical Instruments. Furthermore, the oxygen content of the powders is determined by the carrier gas hot extraction method. Due to the fact that the amount of material in the thin films is not sufficiently enough to be used to determine the oxygen content with this method, it is calculated from the ICP-OES-results. The obtained values are summarized in table 4.4, whereat experimental errors are approximately 1-2 %. Additionally, SIMS measurements are performed on LFP thin films to profile the elemental distribution

along the thickness of the films.

Intended composition	Measured Composition	
	Powder	Thin Film
Li$_{1.00}$Fe$_{1.00}$P$_{1.00}$O$_{4.00}$	Li$_{0.96}$Fe$_{1.00}$P$_{0.96}$O$_{3.82}$	Li$_{0.92}$Fe$_{1.00}$P$_{0.98}$O$_{3.92}$
Li$_{3.50}$V$_{0.50}$Si$_{0.50}$O$_{4.00}$	Li$_{2.23}$V$_{0.44}$Si$_{0.50}$O$_{3.16}$	Li$_{2.31}$V$_{0.59}$Si$_{0.50}$O$_{3.63}$

Table 4.4: Chemical composition of LFP and LVSO powder and thin films.
This table lists the chemical composition of LFP and LVSO powder and thin films as
determined by ICP-OES and carrier gas hot extraction, assuming Fe to be stoichio-
metric in LFP and Si to be stoichiometric in LVSO samples.

LiFePO$_4$

The results obtained by ICP-OES show a 8 % lithium deficiency for the LiFePO$_4$ thin
films, which could not be further decreased using the given PLD system. Nevertheless,
this lithium deficiency is still within the solubility limit of FP in LFP, which is up to
10 % at room temperature [13, 86, 89, 90, 91], so that the elemental analysis is not
contradicting the growth of phase pure Li$_{1-x}$FePO$_4$. Furthermore, the depth profiles
of as-prepared LFP thin films, recorded by SIMS and shown in figure 4.4, confirm a
homogeneous distribution of Li, Fe and P within the electrode.
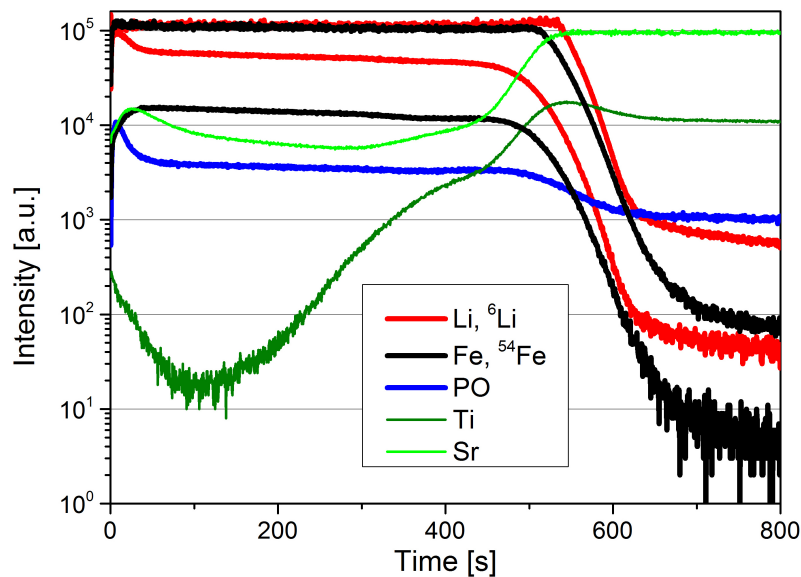
Figure 4.4: SIMS measurement of LFP thin film. The SIMS measurement shows
a homogeneous distribution of Li, Fe and PO over the whole thickness of the LFP thin
film, deposited on STO.

LVSO

For LVSO the lithium content is found to be sufficiently lower in the target material than what has been intended upon synthesis. This lack in lithium is expected and in line with what is reported in literature, where a nominal composition of $Li_{3.4}V_{0.6}Si_{0.4}O_4$ results in target compositions of $Li_{1.53}V_{0.35}Si_{0.4}O_{2.44}$ [179] and $Li_{2.0}V_{0.47}Si_{0.53}O_{3.2}$ [114], respectively, using the same synthesis procedure as reported by Ohtsuka and Yamaki, which has also been used in this thesis [174, 175]. Compared to these results, the lithium content of the target is even slightly higher than what would have been expected from a literature study, which is supposed to be due to the slightly lower sintering temperatures, reducing the evaporation of lithium. The relative increase of Vanadium concentration from V/Si=4.4/5.0 to V/Si=5.9/5.0 in the deposited thin films, compared to the target material is again in line with what has been reported for PLD-grown LVSO thin films [114, 179]. Finally, the synthesized LVSO targets and deposited X-ray amorphous LVSO films show nearly identical X-ray diffraction patterns (target) and chemical compositions (target, thin film), compared to what has been reported in literature [114, 170, 174].

4.2.3 Morphological characterization by SEM

The morphology of LFP and LVSO thin films deposited on different substrates is studied via SEM using a Merlin and a Crossbeam scanning electron microscope with built-in FIB (Crossbeam) from Zeiss [186, 187].

$LiFePO_4$

The LFP thin films deposited via PLD possess a dense morphology without any voids or pores, but exhibiting cracks, most likely developing upon cooling down the sample after deposition (compare figure 4.5 a)). This holds for all kind of substrates (Si (100), titanium, Nb:STO (100) and Si_3N_4 membranes), even though leading to slightly differently textured thin film morphologies. In addition, the formation of droplets on the thin films, which is related to the ejection of liquid material from the target (compare section 2.1), has been largely avoided by the chosen PLD parameters. The cross sectional view in figure 4.5 b) demonstrates that the deposited LFP thin films are

well adherent to the substrate, exhibiting an almost uniform thickness, while the surface modulation originates from the existing individual grains, which are also sintered together during the deposition process.
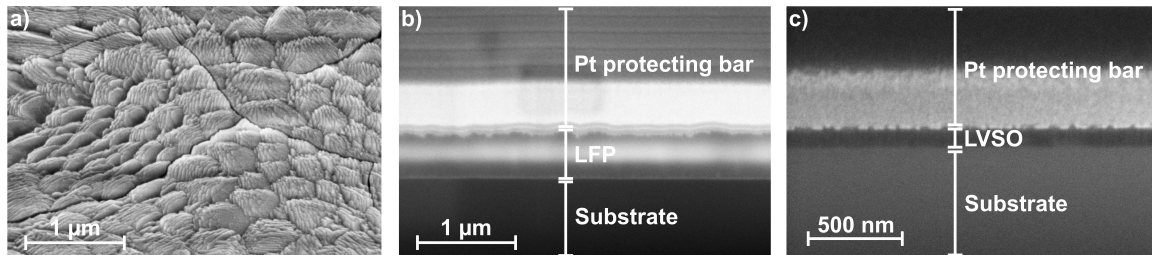

Figure 4.5: SEM images of LFP and LVSO thin films. The SEM micrographs of fabricated thin films show a typical a) LFP surface b) LFP cross section c) LVSO cross section.

LVSO

The LVSO films, deposited at room temperature without any further annealing steps, exhibit a rough surface, but show a nice areal contact to the substrate, without any observable voids, pores or cracks (compare figure 4.5 c)). Although a higher substrate temperature during deposition generally leads to smoother thin films, as has also been found by Zhao et al., studying the dependence of film morphology and substrate temperature for LVSO thin films deposited via PLD in more detail [180], the substrate temperature is the only parameter which should not be changed, since the LVSO electrolyte layer is deposited after the LFP cathode during fabrication of the all-solid-state thin film battery, and the latter one easily oxidizes at elevated temperatures in an oxygen containing atmosphere, as already mentioned in subsection 4.1.2. Therefore, although deposition of LVSO at elevated temperatures or alternatively a subsequent heat-treatment of the deposited thin films generally is beneficial in terms of morphology and even ionic conductivity [174, 175, 179, 180] (see also next subsection), the LVSO films are deposited at room temperature to keep the main part of interest of the thin film battery, the LFP cathode material, as pure and unaltered as possible.

4.2.4 Electrochemical characterization

LiFePO$_4$

Charge-discharge, as well as cyclic voltammetry measurements have been performed on the deposited LFP thin films to characterize their electrochemical behaviour, using a battery charger BT Pulse from Arbin Instruments. (Discharge) capacities of about 100 mAh/g have been achieved for 300 nm thick films at a rate of 0.1 C, cycled in a 1 M LiPF$_6$ in EC/DMC electrolyte versus lithium metal.[3] This already indicates that the time needed to study a complete cycle of (de)lithiation of the electrode material by *in situ* XAS will be on the order of days, rather than hours. Figure 4.6 shows several cyclic voltammograms, obtained at different scan rates ν, recorded within the same battery arrangement as stated above. They are shown together with a plot of the measured peak currents I_p versus $\nu^{1/2}$ to determine the chemical diffusion coefficient of the Li$^+$ ions in the LiFePO$_4$ thin film, using the Randles-Sevcik equation 3.1, introduced in subsection 3.2.3. For this, a background current baseline, originating from the ionic
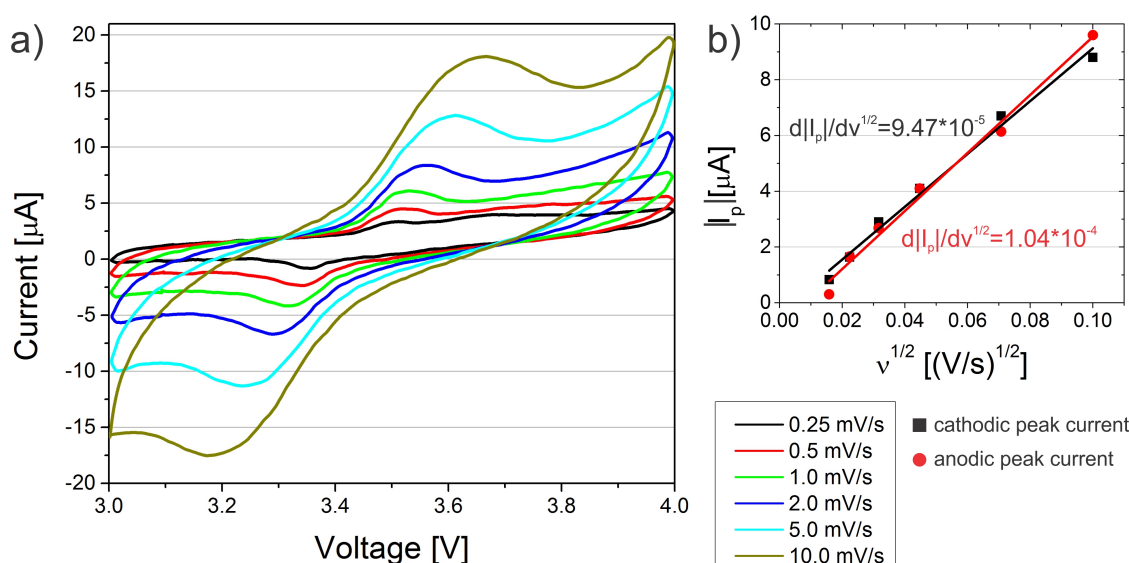
Figure 4.6: Cyclic voltammogram of a LiFePO$_4$ thin film. a) Cyclic voltammograms of a LiFePO$_4$ thin film at different scan rates. b) Plot of the cathodic (black) and anodic (red) peak currents vs. the square root of the scan rate $\nu^{1/2}$.

double layer at the surface of the electrodes, functioning as a capacitor, is extrapolated

---

[3]Given the dense morphology of LFP thin films observed with SEM, a density of the film of 3.5 g/cm^3, corresponding to the bulk value of LiFePO$_4$, is assumed to calculate the gravimetric capacity from the film thickness, area and current flow.

to the peak potentials to measure the peak currents. With a tabulated value of 0.4463 for the transcendental function χ at the peaks of the voltammogram [164], the Randles-Sevcik equation simplifies for T=298 K to

$$I_p = 2.69 \cdot 10^5 \; \left[\tfrac{As}{molV^{1/2}} \right] \; n^{3/2} A c \left(\nu \tilde{D}_{Li} \right)^{1/2} \tag{4.1}$$

(compare equation 3.2). Since the number of electrons involved in the redox reaction is n=1, the area of the electrode A=0.5 cm^2 and the lithium concentration in LiFePO$_4$ c=0.0222 mol/cm^3, for the chemical diffusion coefficient of the Li$^+$ ions in the LFP thin film follows from the slopes in figure 4.6 b) $\tilde{D}_{Li}$=1.01·10^{-15} cm^2/s for the cathodic and $\tilde{D}_{Li}$=1.21·10^{-15} cm^2/s for the anodic diffusion coefficient, respectively. Both values are well within the range of reported lithium diffusion coefficients in LFP thin films determined by CV, ranging from 10^{-18} cm^2/s to 10^{-14} cm^2/s [47, 188] (remember the second footnote in subsection 3.2.3). Furthermore, electrochemical measurements do not give any evidence for significant concentrations of phase impurities like Li$_3$Fe$_2$(PO$_4$)$_3$, LiFeP$_2$O$_7$ or Fe$_4$(P$_2$O$_7$)$_3$, whose Fe^{3+}/Fe^{2+} redox couples lie at 2.8, 2.9 and 3.1 eV vs. lithium metal, respectively [42].

LVSO

To measure the in-plane conductivity of LVSO, deposited on 10x10 mm^2 MgO (110) substrates, two 1 µm thick and 10 mm wide platinum electrodes have been deposited by means of DC magnetron sputtering on top of the LVSO thin film with a distance of 1 mm between them. Both AC and DC measurements have been conducted at room temperature under argon atmosphere. Using a Novocontrol Alpha-A High Performance Frequency Analyzer, the AC measurements have been carried out between 0.1 Hz and 2 MHz with a 100 mV amplitude, while DC measurements have been performed with a Keithley 220 SourceMeter and a Keithley 6514 system electrometer, operated in parallel to the current source, at a constant current of 3·10^{-9} A until steady state voltages are achieved. The DC measurements result in an electronic conductivity of 1.8·10^{-5} S/cm and together with the AC measurements in an ionic conductivity of 7.2·10^{-5} S/cm. While the latter one is even in the upper range of reported ionic conductivities in LVSO thin films (10^{-7} - 10^{-5} S/cm), an ion transference number of

only about 80 % is far below all reported values [174, 175, 179, 180]. Even though Zhao et al. found a decreased ion transference number for LVSO thin films deposited at room temperature, their measured values are still above 99 % [180]. Furthermore, although cross-contamination during deposition of the LVSO thin film and a possible doping of the electrolyte material, respectively, can not totally be excluded, it is, due to the low deposition temperature, very unlikely. Hence, the reason for this unusual high electronic conductivity is essentially unclear. Nevertheless, for the purpose of this work the electrolytes' properties are sufficient enough, accepting high non-Faradayic currents through the electrolyte. In summary: while the properties of the LVSO thin film in terms of electronic conductivity and also morphology could have been improved using higher surface deposition temperatures [180], prevention of loosing the high purity of the LFP cathode phase is rated to be more important than having a better electrolyte.

Electrode Capacities

An upper limit for the capacity C_{LFP} of the LFP thin film electrode, as being part of the all-solid-state thin film battery, can be calculated from its volume $V_{LFP} \approx 4200 \cdot 1200 \cdot 0.3$ µm^3 = $1.5 \cdot 10^6$ µm^3, density $\rho_{LFP} \approx 3.5$ g/cm^3 and theoretical gravimetric capacity $C_{theo,LFP} = 170$ mAh/g via $C_{LFP} = V_{LFP} \cdot \rho_{LFP} \cdot C_{theo,LFP}$ giving $C_{LFP} = 0.89$ µAh. For the LiAl thin film anode, theoretical values of the capacity are due to inevitable short contact times of the deposited thin film with air (after PLD deposition, before mounting in the STXM) and hence possible unwanted side reactions and a possible reduction of practical capacity, respectively, not that meaningful. Instead, initial charge and discharge capacities, as well as the capacities after 10 cycles, are determined for deposited LiAl thin films after an air contact of 5 minutes, and measured to be $C_{prac,LiAl} > 0.6$ mAh/mm^3. With the volume of the thin film anode within the all-solid-state thin film battery of $V_{LiAl} \approx 4200 \cdot 2200 \cdot 0.5$ µm^3 = $4.6 \cdot 10^6$ µm^3, the capacity of the LiAl anode for both uptake and release of lithium is $C_{LiAl} > 2.76$ µAh. Therefore, the practical capacity of the LiAl anode is at least 3 times the overall theoretical capacity of the LFP cathode, so that it can reliably fulfill its desired function as a reservoir for lithium uptake and release upon cycling.

4.3　Assembling of the All-solid-state Thin Film Battery

The micro battery is built on top of a 0.5 x 0.5 mm^2 wide and 200 nm thick X-ray transparent commercial Si_3N_4 membrane from Silson, which is used as the substrate. Compared to other thin film solid-state batteries presented in literature [170, 171, 172], the concept does not have anode, electrolyte, and cathode simply stacked on top of the substrate. Instead, it employs a geometry which is rotated by 90° compared to typical solid-state batteries, so that the Li transport pathway is along the substrate as it can be seen in figure 4.7. This design makes it possible to use STXM to image the charge state within the LFP cathode material, using the shift of the main absorption feature of the Fe L-edge upon (de)lithiation.
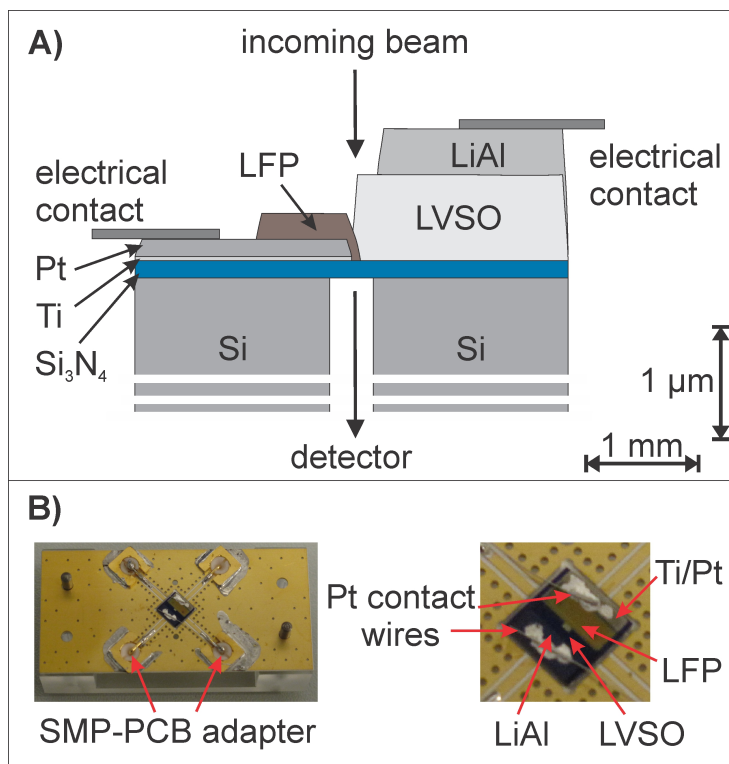
Figure 4.7: All-solid-state thin film battery. A) A sketch of the side view of the designed all-solid-state thin film battery cell. B) Photos of the sample mounted on top of the conductor board.

A detailed description of all processing steps, needed for the fabrication of the thin-film battery on top of a Si_3N_4 membrane (see step (1) in figure 4.8), including the deposi-

tion of the Ti/Pt current collector (step 2), the LFP cathode (3), the amorphous LVSO solid electrolyte (4), the LiAl anode (5) and mounting the sample on a conductor board connecting it to the electrical contacts (6) is given below and visualized in figure 4.8.
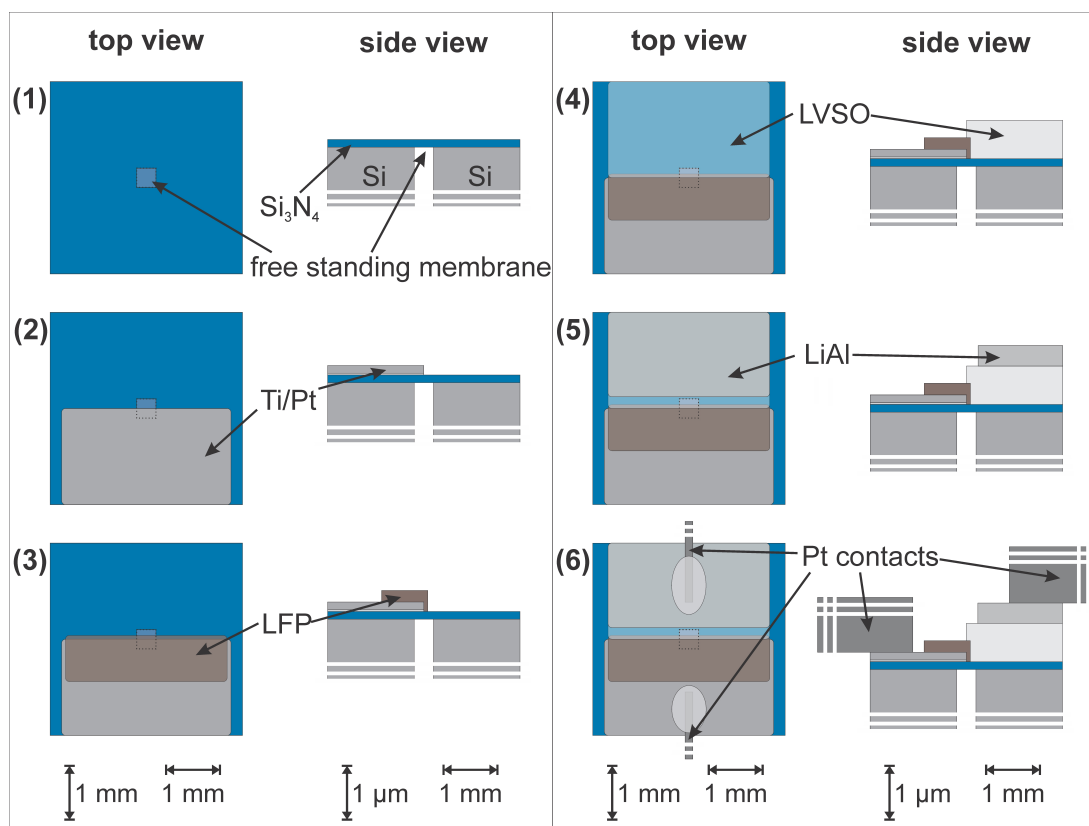
Figure 4.8: Fabrication steps of the all-solid-state thin film battery. The thin film battery is built on top of a Si$_3$N$_4$ membrane (1) by deposition of the Ti/Pt current collector (2), the LFP cathode (3), the amorphous LVSO solid electrolyte (4) and the LiAl anode (5). Subsequently, the sample is mounted on a conductor board and connected to the electrical contacts (6).

In a first step, dense films of 50 nm Ti and 200 nm Pt have been deposited by DC magnetron sputtering onto the future cathode side of the Si$_3$N$_4$ substrate as an inert metal contact layer using a modified EMITECH K575X inside an argon glove box employing a sputter current of 100 mA and an argon process pressure inside the sputter head of $7 \cdot 10^{-3}$ mbar. The titanium works as a binding layer for the platinum, whereat the platinum prevents the titanium from being oxidized during the deposition of LiFePO$_4$. The metal layer ensures a good electrical contact to the electrode material, while it is inert against lithium insertion. Furthermore, it is used as current collector to measure the total electron yield signal (TEY), providing surface sensitive information (compare

section 2.3). Using PLD and different 100 µm thick shadow masks out of molybdenum, a 300 nm thick LiFePO$_4$ cathode, 1000 nm of LVSO electrolyte and a 530 nm thick LiAl anode film have been deposited sequentially within the same PLD system, shown in figure 2.2 in section 2.1, using the PLD parameters given in subsection 4.1.2. A small gap between substrate and shadow masks of about 100 µm is kept to avoid direct contact, side reactions and damaging of the sensitive membrane and deposited films, respectively. After deposition of the LFP layer at 525 °C and cooling the sample down to room temperature, only the shadow mask and target are exchanged against the respective target and shadow mask for depositing the LVSO electrolyte. The amorphous electrolyte is then deposited at room temperature inside an oxygen atmosphere. Afterwards, target and shadow mask are replaced against the ones used for deposition of LiAl. Due to the layout of the PLD chamber, particularly it does not have any adapter for a sample transfer under an inert atmosphere, a short contact of the LiAl target and deposited LiAl anode with air can not be prevented, but only minimized by using an argon counterflow in the chamber when open, and a transfer box which is immediately evacuated and flooded with argon upon sample transfer to prevent reaction with oxygen and air humidity. Finally, the sample is mounted inside an argon glove box on a substrate holder equipped with SMP-PCB adapters, which are connected to the Ti/Pt contact layer and to the LiAl anode via Pt-wires and conductive silver, to electrically contact the sample and charge/discharge the battery while analyzing the cathode material inside the STXM.

Generally, great attention has been paid to the positioning of the shadow masks before film deposition, since this determines the exact layout of the thin film battery. For this purpose a specially designed quartz glass holder is used in which both substrate and shadow masks can be positioned reproducible accurate in both the sputter and the PLD system. Nevertheless, a precision of more than 100 µm in lateral direction for each of the deposited layers is hard to achieve, due to the error margins in manufacturing the quartz glass holder and the shadow masks. This is also the major drawback in the fabrication of this model thin film battery, intended to study the phase evolution of (L)FP *in situ* upon electrochemical (de)lithiation.[4]

---

[4]Using lithography with accuracies below 1 µm for manufacturing an improved all-solid-state thin film battery has also been extensively studied (see subsection 4.4.6).

4.4 Results

All measurements presented here are taken at the MPI-IS endstation "MAXYMUS" at BESSY. Fe $L_{2,3}$ edge spectra are recorded to track the change in the iron oxidation state and local lithium concentration within the thin LFP cathode material, respectively. Using a combination of surface sensitive total electron yield and bulk sensitive absorption measurements at different energies, specific for iron and vanadium, respectively, the exact positions of the different phases is determined. An area close to the Pt current collector is chosen for the *in situ* STXM measurements, where the LFP cathode material is already covered by the LVSO electrolyte. In this region, both full absorption spectra at energies of 705-715 eV and area scans before the edge jump (705 eV) and at the centroids of the respective Fe^{2+} (709.5 eV) and Fe^{3+} (711 eV) Gaussian XANES contributions are recorded before and during lithiation to specify the initial conditions of the sample and to visualize the insertion of lithium and the corresponding phase transformation, respectively.

4.4.1 Survey of the battery layout

Due to the manufacturing process of the all-solid-state thin film battery, the exact positions of the current collector, cathode and electrolyte can not be precisely controlled and are only defined within lateral dimensions on the order of 100 µm. Nevertheless, the exact layout is important to know, to decide on the area where the phase transformation upon (de)lithiation should be followed using *in situ* STXM. Performing energy-line scans across the boundary areas at energies of 705-715 eV (indicative for Fe, i.e. LFP) and 513-523 eV (indicative for V, i.e. LVSO), a combination of surface sensitive total electron yield (TEY) and bulk sensitive absorption measurements (compare section 2.3) is used to determine the exact course of the current collector - cathode material - electrolyte boundaries. The Ti/Pt metal layer is used as current collector to measure the TEY, while all STXM measurements are performed at a pressure of $< 1 \cdot 10^{-7}$ mbar. Figure 4.9 provides a clear picture of the configuration of the all-solid-state thin film battery. In transmission mode (see left images in figure 4.9 c) and d)) the location of the Pt current collector can easily be determined, given by the non-transparent area
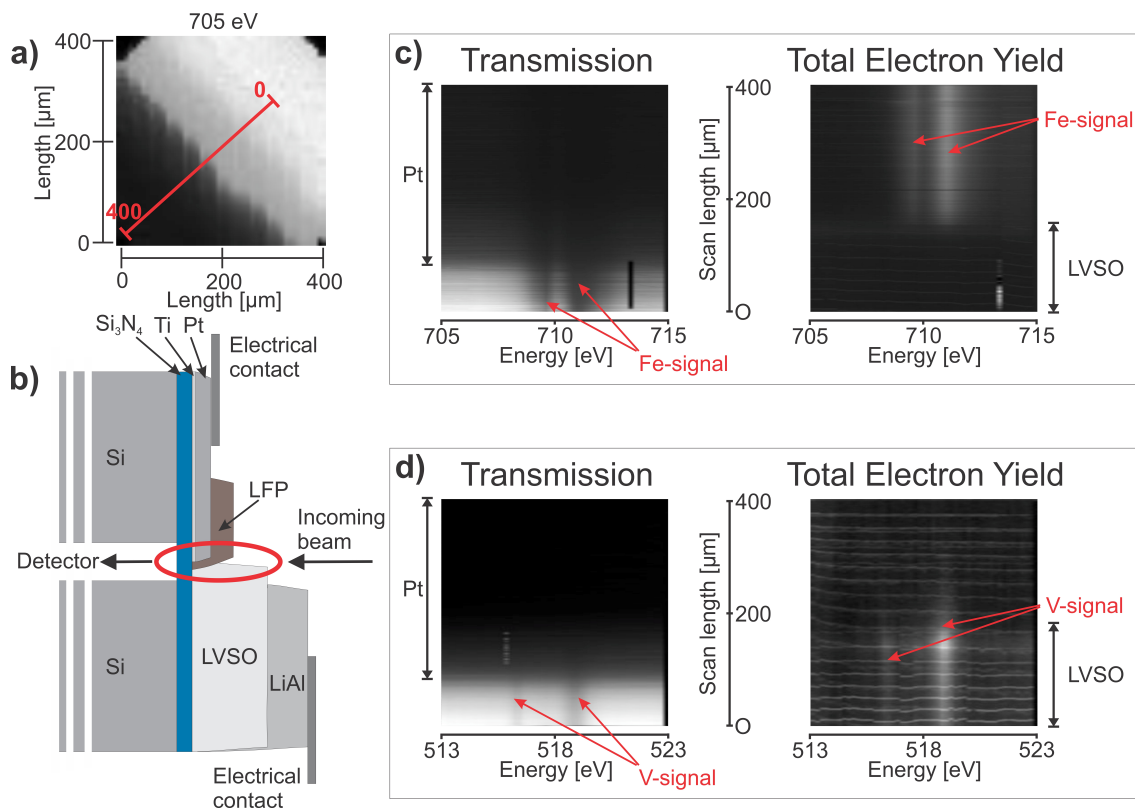
Figure 4.9: Current collector - cathode material - electrolyte boundaries as determined via XAS. a) 400 x 400 µm² overview scan of the sample taken at 705 eV with marked area for line scans shown under c) and d). b) Sketch of the thin film battery with encircled region where the area and line scans shown in a), c), and d) have been taken. c, d) Line scans recorded for energies of 705-715 eV (c) and 513-523 eV (d) in transmission and TEY mode, documenting areas of the Pt current collector, LFP cathode and LVSO electrolyte.

coloured in black for all energies. Additionally, in the range of 705-715 eV also some signal from the iron in the LFP cathode material and in the range of 513-523 eV some signal from vanadium in the LVSO electrolyte is recorded beyond the brink of the Pt current collector. This indicates that the LFP cathode material deposited beyond the Pt current collector is covered with LVSO. The region where $LiFePO_4$ is covered with the electrolyte can be seen in the TEY measurements. Vanishing of the Fe-signal in the energy range of 705-715 eV at the same position where the V-signal in the energy range of 513-523 eV starts, confirms that the LFP cathode is covered with a closed electrolyte layer, starting already above the brink of the Pt current collector.[5]

---

[5]Performing these measurements to pin down the exact layout of the battery also indicates the advantage of using LVSO over the more widely used nitrogen doped Lithiumphosphate (LiPON) electrolyte, because the latter one does not provide, in comparison to LFP, an additional specific

Because of the high X-ray absorption coefficient of Pt it is not possible to follow the
(de)lithiation process of the LFP cathode material on top of the current collector even
though it has a diminishing thickness. Instead, an area close to the Pt current collector
is chosen for the *in situ* STXM measurements, where the LFP cathode material is
already covered by the LVSO electrolyte. In this region full Fe $L_{2,3}$ edge absorption
spectra and area scans are recorded to specify the initial conditions of the sample and
to visualize the insertion of Lithium. The results are discussed in the next subsections.

4.4.2 Initial state of the cathode material

Area scans within the region of interest close to the Pt current collector, where the
LFP cathode material is still covered with the electrolyte, reveal a strong lithium defi-
ciency and an inhomogeneous lithium distribution in the cathode material, even before
starting electrochemical measurements. Figure 4.10 shows such a typical area together
with the corresponding XANES spectra. The STXM image in figure 4.10 a) itself
is calculated from three single STXM images recorded at energies of 705, 709.5 and
711 eV, being processed according to the explanations in subsection 2.3.2.
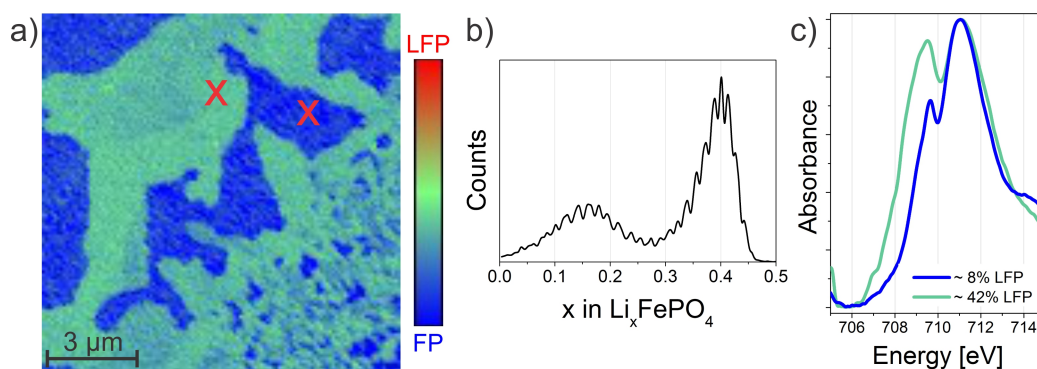
Figure 4.10: Initial state of the cathode material. a) STXM image of a
12x12 μm^2 area, comparing the optical densities of the sample at 709.5 and 711 eV
with each other before electrochemical (de)lithiation. The two red crosses indicate the
points where the XANES spectra, shown in c), have been taken. b) Histogram of the
distribution of averaged lithium concentrations. c) XANES spectra recorded at the
positions marked with the red crosses in a). The color-coding of the STXM image and
XANES spectra is done consistently.

A typical parameter set recording full absorption spectra, as shown in figure 4.10 c),

---

absorption edge to easily observe its deposition area.

includes an energy range from 705-715 eV with energy steps of 0.1 eV, a dwell time per energy step of 1000 ms and a defocus of the X-ray beam between 100 and 200 nm. Performing full XANES spectra at different places with different lithium concentrations enables one to assign to the differently color-coded regions in figure 4.10 a), as well as to the line scans and histograms (compare figure 4.10 b)), the lithium concentrations, averaged along the direction of the X-ray beam. To do so, first absorption spectra of LFP and FP reference samples are taken (compare figure 2.7 in subsection 2.3.2). Then, after normalization, the absorption spectra recorded at different positions of the sample are fitted by a linear combination procedure of the two reference spectra. Afterwards, the corresponding averaged lithium concentrations are assigned to the positions on the sample where the absorption spectra have been recorded and are synchronized with the corresponding color-code, i.e. with the relative absorbances of the sample at energies of 709.5 eV and 711 eV. Plotting the lithium concentration as a function of the used color-coded intensity and fitting the data points by an asymptotic function of the form $y=a+b \cdot c^x$, allows one to convert the measured relative absorbances directly into lithium concentrations. A red area in figure 4.10 a) would correspond to pure LFP, while the lithium content decreases from red over green to blue (FP). Thus, the recorded lithium concentration within the whole area is below 45 %.

Because all the measurements carried out on LFP thin films, deposited at the same conditions as the LFP cathode material for the all-solid-state battery, confirm a pure LFP phase without any secondary phases and only 8 % lithium deficiency (compare section 4.2), there seem to be only two possible effects contributing to an explanation of the initially inhomogeneous lithium distribution and overall lithium deficiency in this region: First, although both electrolyte and anode are deposited at room temperature, preventing any further reaction of the LFP thin film with oxygen, there might be a lithium redistribution at the LFP - LVSO interface, which can lead to a small lithium deficiency in the cathode material. But since this redistribution is limited to the interface, it can not be the dominant effect for the huge lithium deficiency and measured Fe^{3+} concentration, respectively. Instead, the foremost reason is presumed to be found in the deposition procedure using shadow mask, which also function as a partially heat shielding, especially due to the small gap of about 100 µm between sub-

strate and mask, allowing heat transfer only via thermal radiation. To take this effect into account, the surface temperature of the Si$_3$N$_4$ substrate has also been calibrated to the heater output power with built-in shadow mask, using a pyrometer, focused on the non-shadowed substrate area. Nevertheless, a temperature gradient on the substrate between shadowed and non-shadowed areas may exist, so that especially the outer areas of the deposited LFP thin film could have been exposed to a locally higher substrate temperature. Furthermore, the lower temperature of the surrounding shadow mask may have influenced the temperature measured with the pyrometer through the 4.2x1.2 mm^2 wide gap in the shadow mask, so that the actual substrate temperature is higher than the effectively measured one. A higher surface temperature during deposition than the aimed 525 °C would have two main effects on the thin film, which have both been observed and partly reported in literature for LFP films deposited without shadow masks at higher surface temperatures. Firstly, a higher surface temperature actually leads to a slightly higher lithium deficiency, most likely due to an increased lithium evaporation. Secondly, a possible increase in deposition temperature may also lead to an increase in secondary phase formation, especially of Li$_3$Fe$_2$(PO$_4$)$_3$, in which iron possesses the oxidation state Fe^{3+} and might be mistaken for delithiated LFP.[6] For a surface temperature of 600 °C the amount of Li$_3$Fe$_2$(PO$_4$)$_3$ phase in LFP thin films can be even in the range of about 20 % [178]. On the other hand, the formation can still be neglected around 550 °C, because no sign of a Li$_3$Fe$_2$(PO$_4$)$_3$ phase has been observed by XRD measurements of LFP thin films deposited by the used PLD system at such surface temperatures. This may be due to the special care that have been taken to keep the oxygen content as low as possible in the PLD chamber, thus preventing the reaction

$$12 \; LiFePO_4 + 3 \; O_2 \rightarrow 4 \; Li_3Fe_2(PO_4)_3 + 2 \; Fe_2O_3 \; , \qquad (4.2)$$
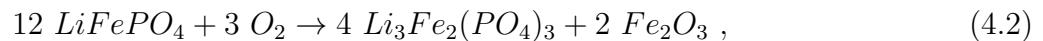
responsible for the impurity phase formation [178]. The exact difference between the substrate temperature set point and actual substrate temperature due to possible tem-

---

[6]Due to the very similar shape and position of the Fe $L_{2,3}$ edge in the XANES spectra of FePO$_4$ and Li$_3$Fe$_2$(PO$_4$)$_3$, the STXM measurements can not be used to distinguish between both phases and to determine the concentration of a possible phase impurity within the cathode material, respectively [189].

perature gradients along the substrate and a possible nonconforming temperature calibration is hard to determine, but the difference is not expected to be higher than 50 °C.[7] Therefore, a safe upper limit for a Li$_3$Fe$_2$(PO$_4$)$_3$ secondary phase impurity concentration within the LFP thin film is given by 10-20 % (based on the iron content). Hence, while the general trend of increased lithium deficiency can be understood in terms of a higher deposition temperature, induced by a partial heat shielding of the shadow mask, a concentration of up to 20 % of a Li$_3$Fe$_2$(PO$_4$)$_3$ secondary phase can not totally be excluded.

Although these starting conditions of the cathode material are unexpected and unfavorable, it is interesting to see, that the Fe^{2+} and lithium concentration, respectively, is not uniformly distributed within the still mostly olivine-structured LFP thin film. Instead, areas containing around 16 % and 40 % lithium prevail, existing directly in contact with each other (compare figure 4.10 a) and b)). Furthermore, a continuous gradient in lithium concentration between these areas does not exist, but rather exclusively the two given lithium concentrations can be found. It can not be excluded that a non-homogeneous distribution of the possible Li$_3$Fe$_2$(PO$_4$)$_3$ impurity phase is the cause for the regions of lower Fe^{2+} concentration. Nevertheless, there are also several groups reporting on minima in the formation energy (even below kT at room temperature) and metastable phases in the Li$_x$FePO$_4$ system, inter alia for compositions of Li$_{0.16}$FePO$_4$, Li$_{0.32}$FePO$_4$ and Li$_{0.5}$FePO$_4$ (see also subsection 1.2.4) [85, 95, 96, 97]. Additionally, phase separation upon cooling down a LFP sample has also been reported [190]. Therefore, the observed two phases can also well be pure Li$_x$FePO$_4$ with lithium concentrations of 16 and 40 %.

Here it should be kept in mind that the observed Fe^{2+} and lithium concentrations, respectively, are averaged at every point along the sample thickness (around 300 nm of LFP) in the direction of the beam and do not contain any further local information on the lithium distribution. Nevertheless, the absence of a smooth lithium gradient in the LFP thin film suggests that there are not several different Li$_x$FePO$_4$ phases sitting on top of each other, whose ratios could easily vary, thus leading to various averaged lithium concentrations, but rather the two observed concentrations are also present

---

[7]Estimated from simple thermal conduction ($\dot{Q} = \frac{\lambda}{d} A \Delta T$) and thermal radiation ($\dot{Q} = \varepsilon \, \sigma \, A \, T^4$) equations.

along the thickness of the cathode material.

4.4.3 STXM mapping during lithiation

Because the area of interest exhibits a lithium concentration below 45 %, the battery is first discharged and the cathode material lithiated, respectively. Here, the usage of a lithium containing anode pays off. Discharging of the all-solid-state thin film battery is done galvanostatically at a current of 25 nA using a Keithley 2634B System SourceMeter, which can even reliably source and measure currents of below 1 pA (voltage accuracy is in the micro-range)[191]. The shift in the main absorption feature from around 711 to about 709.5 eV upon lithiation is used to fingerprint the change in the local state of charge. Therefore, image sets of 3 images, taken at energies of 705, 709.5 and 711 eV, are recorded to compare the normalized relative X-ray absorption at the centroids of the respective Fe^{2+} (709.5 eV) and Fe^{3+} (711 eV) Gaussian XANES contributions, being corrected for the optical density of the sample. The scans are done on a 12·12 µm^2 area (see figures 4.10 a) and 4.11) with a 50 nm step size, a dwell time at each point of 1 ms, a line delay (uni-directional scan) of 250 ms and a 30 nm focus of the X-ray beam. Together with other waiting times such as for the piezo motors and the monochromator to change the energy, the total time to acquire one set of images is about 12 minutes.

The first necessary step of data processing is to well-align the 3 images to each other, because of small shifts of the sample in the beam over time. Then the absorbance at each point of the sample is calculated for 709.5 and 711 eV according to $lg\left(\frac{I_{705}}{I_{709.5}}\right)$ and $lg\left(\frac{I_{705}}{I_{711}}\right)$, respectively. By dividing the two resulting absorbances at each point, generating a single image from the image set, the lithiation of the cathode material is followed as a function of time. More details on performing the *in situ* STXM measurements and how the obtained data is analyzed are already given in subsection 2.3.2.

During lithiation several image sets are recorded and figure 4.11 shows a series of those, documenting the initial lithiation process of the thin $Li_x FePO_4$ cathode material. The images are colour-coded so that the lithium content decreases from red (LFP) over green to blue (FP) (compare figure 4.10). They are also used for a more detailed line scan analysis across the most active part of the studied region to analyse the phase
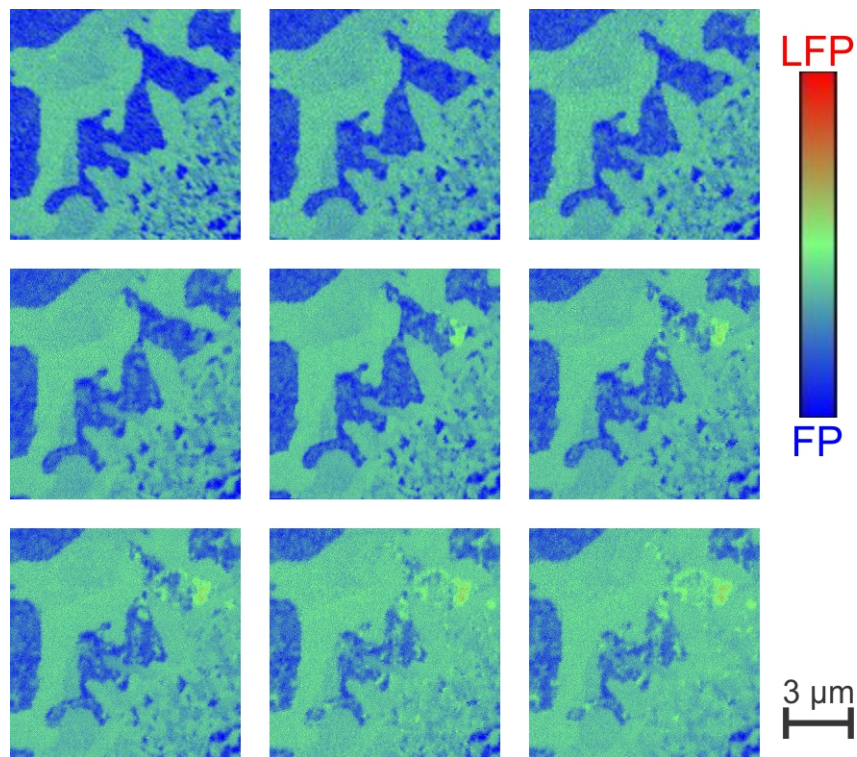
Figure 4.11: Series of STXM images. STXM images of 12x12 µm^2 comparing the optical densities of the sample at 709.5 and 711 eV with each other during electrochemical lithiation.

evolution in more detail (see figures 4.13 and 4.14), which is discussed in the next subsection.

It is obvious from figure 4.11, that the lithiation of the LFP cathode material has been stopped long before it has been completely lithiated. This is because the lithiation is very slow due to the long diffusion paths and can not be further accelerated without taking the risk of decomposing the battery material. At the applied current of 25 nA (corresponding to a C-rate of about 1/36), the corresponding voltage is already as high as 27 V. The most probable reason for such a high value is the long distance lithium ions have to travel through the electrolyte and electrons have to travel through the cathode material, given rise to high resistivities. Although such a voltage is inexpressibly high for any known possible battery system and would directly lead to a decomposition and break down of the active materials, it is not clear where exactly the applied voltage drops and the large dimensions of the present cell most probable lead to much lower voltages, any of the battery components is directly exposed to. Another reason for the slow lithiation of the LFP cathode is the high non-Faradayic by-pass current, reduc-

ing the measured OCV to values in the mV range, so that most of the 25 nA is even conducted by electronic instead of ionic transport. Taking the limited beam time into account, following the lithiation of the LFP cathode material any further seems to be impractical.

Nevertheless, a closer look at the *in situ* recorded initial lithiation of the Li$_x$FePO$_4$ cathode material, shown in figure 4.11, reveals already some important observations and clear indications for the overall underlying lithiation mechanism of the LFP thin film: Firstly, the lithiation does not occur homogeneously within the whole cathode material, but is primarily rather limited to the areas of initially very low lithium concentration (initially blue-colored). Thus, while the lithium concentration in the areas showing an averaged composition of about Li$_{0.4}$FePO$_4$ does not significantly change, the regions initially having a lower lithium concentration undergo the lithiation first and faster, respectively. Secondly, even within the areas of initially low lithium concentration, the lithiation does not occur homogeneously but starts at some chosen sectors. Here it is worth noting, that the areas where the lithiation starts are not completely lithiated before other areas undergo the lithiation process, but instead more and more regions start to participate in the lithiation, so that one can speak from a simultaneous lithiation of the cathode material, though inhomogeneous in nature. These findings are discussed in more detail in the next subsection using histograms to compare the overall distribution of lithium concentration within the analyzed area. Furthermore line scan analysis and series of full XANES spectra, recorded during lithiation at the same positions, document the constant increase in Fe^{2+} and lithium concentration, respectively, as a function of time and place.

4.4.4 Phase evolution

Figure 4.12 discloses how the overall distribution of lithium concentration within the studied area changes upon lithiation of the cathode material, by providing the total counts of each lithium concentration within several processed absorbance images, some of which are also presented in figure 4.11, representing the change over time. What could already be seen from the series of STXM images shown in figure 4.11 manifests also in a more quantitative way in figure 4.12, scilicet that mainly the areas of lower
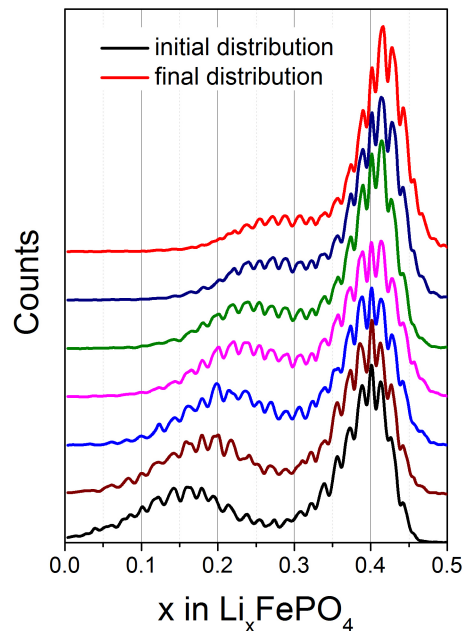
Figure 4.12: Change in distribution of lithium concentration. Distribution of lithium concentration within several absorbance images of the cathode material, recorded during galvanostatical discharging of the thin film battery to visualize the lithiation process.

lithium concentration are lithiated first, while the distribution of lithium concentration around a composition of $Li_{0.4}FePO_4$ stays at the beginning nearly unchanged. This is expressed by the first peak in the lithium distribution, centered around $Li_{0.16}FePO_4$, shifting to higher lithium concentration before it begins to flatten and the center of the second peak, around $Li_{0.4}FePO_4$, begins to shift. While this representation reflects the overall trend, more details on the local change in lithium concentration is given in figure 4.13, presenting both series of XANES spectra and a line scan analysis. In figure 4.13 a) and b) STXM images are shown, recorded before (a) and after (b) electrochemical lithiation for a direct comparison of the changes in lithium concentration. As can be seen from the XANES spectra in figure 4.13 c), recorded at position (1) in figure 4.13 a) and b), respectively, the lithium concentration changes at this position from an initial value of about 8 % to 48 %, while in the meantime, the lithium concentration at position (2) only changes from 42 to 44 % upon lithiation (4.13 d)). These series of XANES spectra confirm the inhomogeneous lithiation of the cathode material, with the general trend, that initially mainly areas of low lithium content are lithiated. Furthermore, the line scan analysis shown in figure 4.13 e), performed along the red lines
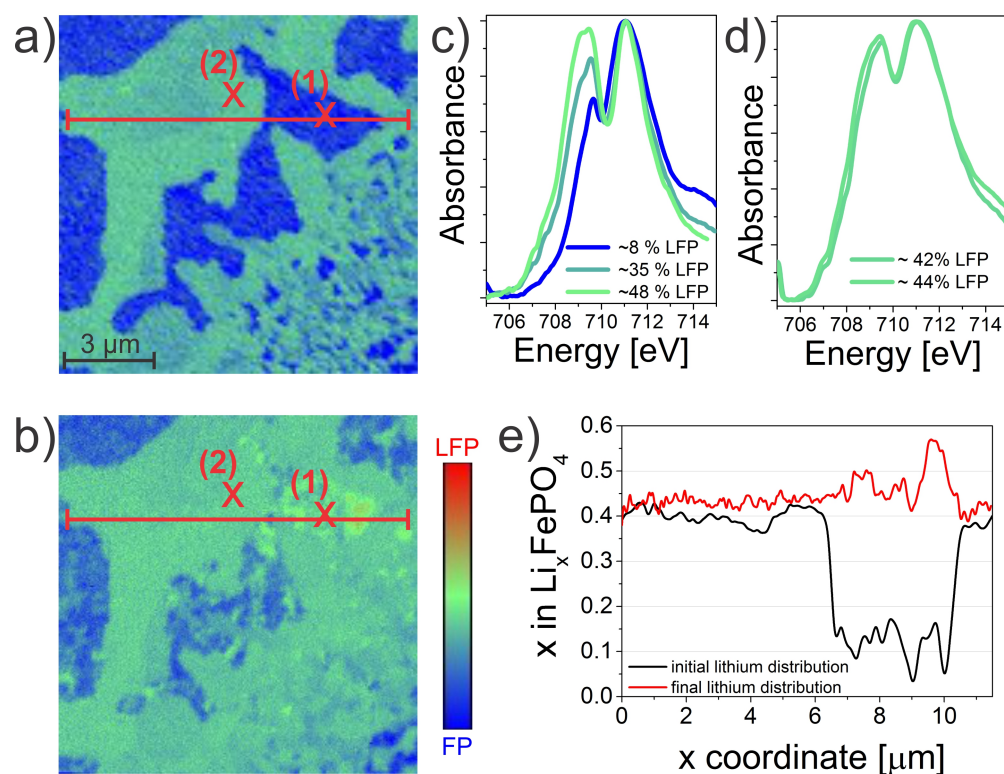
Figure 4.13: Local change in lithium concentration. Initial (a)) and final (b)) STXM images of the studied 12x12 µm^2 area, comparing the optical densities of the sample at 709.5 and 711 eV with each other during electrochemical lithiation. The red crosses labeled with (1) and (2) mark the points where XANES spectra have been repeatedly recorded during lithiation, some of those are shown under c) and d). Line scans have been taken along the red lines in the STXM images under a) and b) and are shown together in subimage e).

in figure 4.13 a) and b), respectively, illustrates the phase evolution upon lithiation: While only relatively small changes occur within the first 6 µm of the line scan, the lithium concentration between µm 6 an 11 changes significantly, whereat the initial form of the distribution of lithium concentration is not preserved throughout the lithiation process. Performing a line scan analysis not only on the initial and final state of the cathode material, but also at intermediate states, as reflected by the STXM images in figure 4.11, presents the concurrent but inhomogeneous lithiation very clearly and is shown in figure 4.14. Following e.g. the green line in figure 4.14 identifies areas with an increase in lithium concentration between two line scans of more than 10 %, whereat other regions are not lithiated at all. This nicely documents that different parts of the cathode material with initially the same lithium concentration, and which even stay in
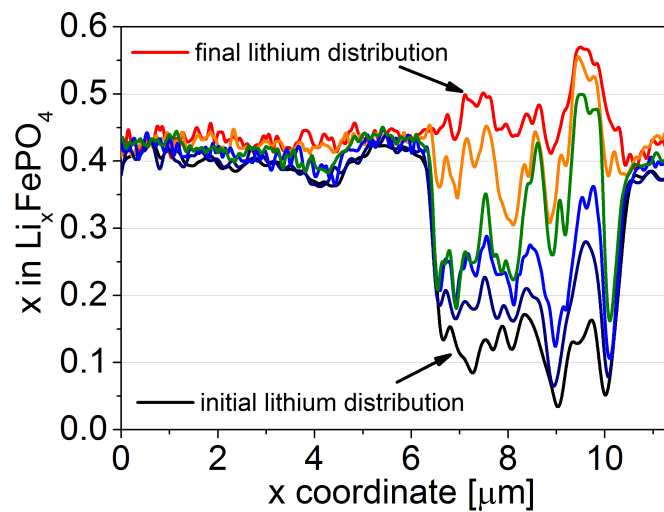
Figure 4.14: Line scan analysis. The presented line scan analysis on several STXM images, some of which are shown in figure 4.11, is done along the red line of figure 4.13 a).

direct contact with each other, are lithiated successively during the lithiation process. Furthermore it is obvious, that not a single region is first completely lithiated before another region begins to lithiate, but instead the regions which are lithiated the most within a given period of time alternate. In addition, these line scans show, that the lithium concentration in the initially blue-colored areas rises even above the concentrations within the surrounding Li$_{0.4\pm\delta}$FePO$_4$ and that only from that point on also the lithium concentration in that phase starts to change measurably (see orange and red line in figure 4.14), with a tendency to reach a not to different lithium concentration within the sample. Finally, a monotone increase in lithium concentration is observed at every point of the sample, meaning that no area is lithiated at the expense of another and all lithium is provided from the electrolyte, respectively.

Before these results are discussed in more detail, it should be argued that both the electrode - electrolyte contact as well as possible cracks within the cathode material are very unlikely to be causal for this behaviour: That cracks within the electrode material may separate all the regions from each other, which are not lithiated at the same time, can be simply excluded by comparing the STXM absorbance images (see figure 4.11) as well as the line scans (see figure 4.14) with the recorded SEM images (see figure 4.5), documenting different scales and patterns. In addition, crack formations accompanied by cleavage formations between the two separated parts would also

be visible within the original STXM images by areas of lower X-ray absorption. Such cracks could not be observed in the STXM images. A crucial influence of the electrode - electrolyte contact on the observed lithiation process can be excluded, because of the areal contact of the deposited LVSO thin film (see figure 4.5) and the observed alternation of the lithiation process within areas of same initial lithium concentration.

4.4.5 Mechanistic interpretation

As already summarized in subsection 1.2.4, a digital phase distribution can be observed in multi-particle arrangements with either nearly completely lithiated or delithiated particles [98]. The reason for such a distribution lies in the non-monotone dependence of the lithium chemical potential μ_{Li} on the lithium content on the single-particle level, as shown in figure 4.15 a), favoring particle by particle (de)intercalation [99, 192].
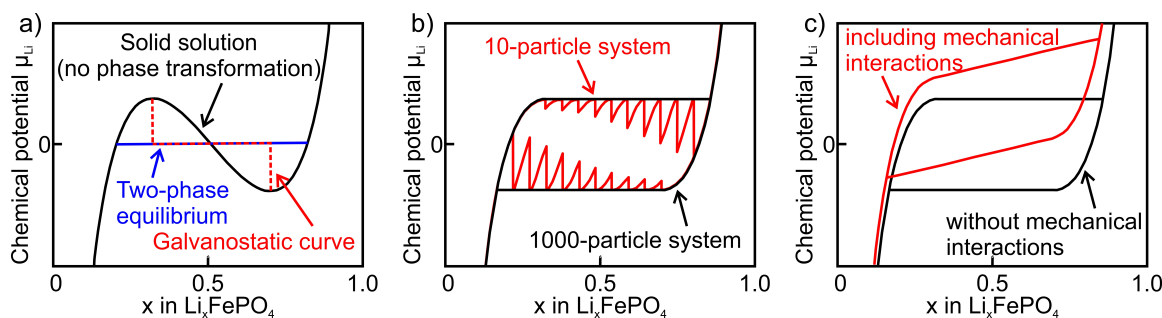
Figure 4.15: Lithium chemical potential in LFP. a) Profiles for the lithium chemical potential in a single LFP particle. The black curve represents the course without a phase transition, the blue line the two-phase equilibrium potential and the dashed red line the galvanostatic path for slow (dis)charge and phase separation. b) The red line gives the chemical potential of a system containing 10 LFP particles and the black line describes the hysteresis loop of a many particle system with 1000 particles. c) The black line represents again the system containing 1000 particles and the red line the same system, but this time mechanical interactions between the single particles are taken into account. Representation according to [99, 192, 193].

Going from the single-particle level gradually to a multi-particle arrangement leads to a lithium chemical potential, dominated by a hysteresis loop, as it is depicted in figure 4.15 b). However, a thin film cathode is not an ordinary multi-particle electrode material, but can instead be viewed as an intermediate stage between a huge two-dimensional expanded single particle and a multi-particle arrangement, in which the particles stay in direct contact with each other, without any other secondary phases

such as carbon coatings or binders between them (in particular: no phase that can buffer mechanical interactions of the LFP particles due to volume changes upon cycling). This circumstance is also reflected by the observed lithiation: for an exemplary multi-particle system one would expect the mentioned particle by particle mechanism, i.e. only very few regions should undergo the lithiation at the same time up to nominally pure LFP, while all others stay essentially unchanged or rather show even a slight decrease in lithium concentration while the neighboring areas are lithiated. For the thin film cathode under investigation, a rather simultaneous lithiation is observed, even though inhomogeneous in nature. The inhomogeneity can principally have several reasons, such as different particle orientations (catchword: anisotropy of ionic and electronic conductivities), possible higher dimensional defects (compare chapter 3), different good electrode-electrolyte contacts or mechanical interactions, induced by the volumetric expansion of the particles upon lithiation of about 6.5 % [24] (compare subsection 1.2.1 and see explanations below), influencing the local kinetics and even changing the thermodynamics upon lithiation.

Here it should be pointed out again, that the STXM measurements do not provide any information about the lithium distribution along the direction of the X-ray beam and hence no information, whether the phase transformation within the thin film follows a single- or two-phase mechanism. Furthermore, it is not possible only from the STXM measurements to exclude the possibility that the thin film cathode consists of stacks of many particles, which are successively lithiated, thus following the expected lithiation mechanism for a multi-particle system as described by Dreyer et al. [99]. Nevertheless, TEM measurements of LFP thin films grown under the same conditions in the same PLD system show thin film cathodes consisting of single grains along the film thickness. In addition, the possibly higher than projected deposition temperature of the cathode material would rather lead to bigger than to smaller particles. Finally, no decrease in lithium concentration close to areas of increasing lithium concentration, i.e. no demixing of phases, has been observed, which could have supported the particle by particle mechanism. Hence, the observed lithiation mechanism corresponds rather to a single-particle lithiation process or to a multi-particle mechanism of a material with a monotone and almost monotone chemical potential, respectively, whereby the classical

particle by particle mechanism can not be observed.

A possible reason for the difference in (de)lithiation mechanism for multi-particle and thin film LFP cathode materials may be found in the different significance of mechanical interactions between LFP particles in a full battery electrode material and within the studied LFP thin film. While in powder electrodes secondary phases, such as carbon coating and binders, are expected to buffer most of the mechanical stress in the cathode, induced by the volume change upon (de)lithiation, thin films do not have such "buffer layers". Dreyer et al. showed, that mechanical interactions upon lithiation between individual LFP storage particles result in a non-zero slope of the otherwise horizontal two-phase plateau [192], as it is also shown in figure 4.15 c). Such a slope in chemical potential should therefore be visible in the charge-discharge curves of the LFP thin films, represented by a corresponding slope of the voltage plateau. And indeed, non-horizontal voltage plateaus have been observed for the deposited LFP thin films and are also widely reported in literature (e.g. [47, 194]), even for LFP thin films containing small amounts of carbon [44, 157, 184]. How steep the slope is, should depend on several parameters such as film porosity, possible secondary phases (e.g. carbon), particle (grain) size, film thickness and thin film orientation (catchword: anisotropy of lattice parameter change upon lithiation, compare subsection 1.2.1) but also on the exact measurement environment (e.g. within an all-solid-state battery or in contact with a liquid electrolyte, which itself may not be restricted in volume) and is also differently strong pronounced in the cited literature. Hence, not all LFP thin films should necessarily show the same (de)lithiation mechanism, but instead it should be possible to tune it by turning the mentioned adjusting screws. Interestingly, a disappearing horizontal voltage plateau is also found for multi-particle systems, where the particle size is so small, that the miscibility gap vanishes and therefore a single-phase mechanism prevails, not favoring anymore the particle by particle mechanism [195, 196].[8]

The reduced capability of LFP thin films, especially within an all-solid-state thin film

---

[8]Actually, the reported slope in the LFP thin film voltage plateau in reference [194] is expected to rather originate from the above mentioned mechanical interactions than from the, assumed by the author to be causal, small particle sizes in the LFP thin film of about 20 nm, because for 20 nm particles the observed tilt is expected to be much more pronounced and the voltage change to be on the order of several 100 mV, instead of the observed 20 mV. Furthermore the overall course of the voltage-curve should have a different shape (compare [13, 196]) and no hysteresis should have been observable.

battery, to accommodate these mechanical interactions may not only result in a tilt of the voltage plateau, but also significantly decrease the non-monotonicity and may even change the characteristics of the single particle chemical potential to a monotone form, due to the volumetric restrictions. Furthermore, in a dense film, volume expansion can only occur perpendicular to the surface. Since the interface energy at the surface is larger than the interface energy at a grain boundary, which in turn is larger than in the bulk, the formation of a new surface area by particle expansion perpendicular to the surface is energetically unfavorable. In other words, it is energetically more favorable to simultaneously lithiate various particles minimizing mechanical stress and interface energy within the LFP thin film, in which stress can essentially only be released perpendicular to the surface, by crack formation (compare the observations for large LFP particles [68]) or if particles are lithiated whose **c**-axis is oriented along the surface (decrease in lattice parameter along (001) upon lithiation, compare subsection 1.2.1). Therefore, the observed largely concurrent lithiation mechanism with alternating active regions for the lithiation can be understood in terms of mechanical interactions between the single grains of the thin film, resulting due to volume expansion and connected formation of new high energy surfaces upon lithiation, leading to a change in lithium chemical potential of each individual grain during the lithiation process and hence to an effective tipping of the lithium chemical potential to a monotone form. Moreover, the mentioned change in the single particle chemical potential to a monotone form further implies, that the lithiation of the LFP thin film and the individual particles (grains) therein, is also changed from a two-phase to a single phase mechanism upon lithiation, minimizing the occuring mechanical stress. Though, STXM measurements do not provide direct information about the lithium distribution along the X-ray beam, the observed lithiation phenomenon of the thin film and corresponding interpretation offers this additional information by unfolding the single particle lithiation mechanism to follow a solid solution path after the tipping of the lithium chemical potential to a monotone form upon lithiation.

The observed change in the (de)lithiation mechanism of LFP thin films compared to ordinary multi-particle systems implicitly suggests that no or only a greatly reduced hysteresis of thermodynamic origin, as described by Dreyer et al. [99], should be found

in these cathodes and that the respective batteries should not exhibit any memory effect and the accompanying problems of estimating the state of charge as described by Sasaki et al. as a result of the particle by particle mechanism [193]. Furthermore, this leads to an increase in efficiency of batteries exhibiting LFP thin films compared to batteries with ordinary LFP powder electrodes. Finally, these findings are rather general and applicable to all kind of thin film electrode materials with a non-monotone single particle chemical potential, which show a large enough volume change during lithiation. Since such non-monotonicity can be found for most insertion battery materials [99], the conclusions made here are largely independent from the phase-purity of the analyzed sample, especially since they are found within both areas of initially different Fe^{2+} and lithium concentrations, respectively.

4.4.6 Outlook

The major drawback, arising from the fabrication of this model system, intended to study the phase evolution in thin film LFP electrodes *in situ* upon electrochemical (de)lithiation, is that the exact positions of the current collector - cathode and cathode - electrolyte interfaces can not be precisely controlled using shadow masks and are only defined within lateral dimensions on the order of 100 µm. Furthermore, the design involves long diffusion paths and hence slow charging rates. This, in combination with the limited beam time, makes it difficult to follow a complete lithiation/delithiation cycle of the cathode material. To overcome these problems photo and electron beam lithography with accuracies below 1 µm have been used to manufacture an improved version of this all-solid-state thin film battery, whose projected layout is shown in figure 4.16

In close collaboration with the Nanostructuring Lab of the Max-Planck Institute for Solid State Research great efforts have been made to realize this battery cell. Unfortunately the difficulties emerging upon repeated application and removal of photoresist and ion milling to remove parts of the waste photoresist, cathode, electrolyte and anode material on top of the only 200 nm thick Si$_3$N$_4$ membrane, coming along with altering the originally deposited LFP material, could not be overcome.

Another possibility to study the phase evolution within the LFP cathode of an all-
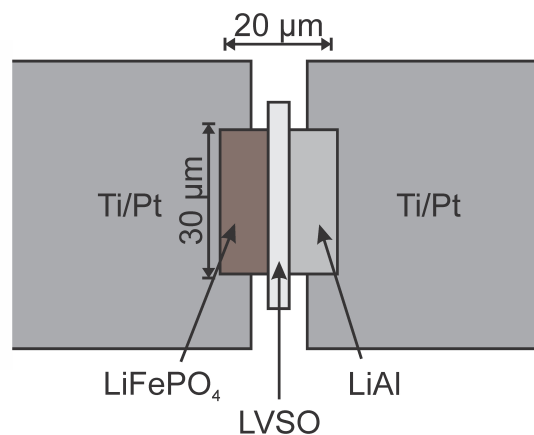
Figure 4.16: Layout of the improved all-solid-state thin film battery. This sketch shows the projected layout of the all-solid-state thin film battery to be fabricated using lithography methods on top of a Si_3N_4 membrane.

solid-state thin film battery is given when measuring the X-ray absorption at the Fe K-edge, instead of using the Fe L-edge, to distinguish between the different oxidation states, following the (de)lithiation process. The higher X-ray energy at the K-edge enables one to use thicker samples due to the higher absorption length of the X-ray beam (e.g.: absorption length of Ti current collector at 700 eV: 200 nm, at 7 keV: 7800 nm). Hence, it is possible to fabricate an ordinary all-solid-state thin film battery (all layers simply stacked on top of each other) on top of a Si_3N_4 membrane and to use XAS to measure the absorption of the LFP cathode. Such a layout has some advantages and disadvantages, compared to the all-solid-state thin film battery design shown in figure 4.16. The disadvantages are, that in such an arrangement it is in principle not possible to follow the (de)lithiation process within the LFP thin film along the transport pathway between electrolyte and current collector and the larger overall contact area does not allow one to study the whole battery at once, so that important characteristics may not be seen. On the other hand such an all-solid-state thin film battery is much easier to fabricate (no lithography or shadow masks needed) and the shorter diffusion lengths through the electrolyte will enable one to study a complete (de)lithiation cycle, following the phase evolution in terms of particle by particle or concurrent mechanism. Such measurements should be possible e.g. at the full-field transmission X-ray microscope (TXM) at the wiggler beamline 6-2c at the Stanford Synchrotron Radiation Lightsource (SSRL), providing a spatial resolution of 30 nm for

photon energies in the range of 5-14 keV [197].

While working on the improved all-solid-state thin film battery with a lateral design concept, the idea for a micrometer-sized all-solid-state battery has been conceived and the cell fabricated using nanostructuring tools. The limited available synchrotron beam time is dedicated to that newly developed battery design and the next chapter deals with the phase evolution within the single crystalline LFP cathode material of this micrometer-sized battery cell.

Chapter 5

In situ Observation of Cycling a LiFePO$_4$ Single Crystal

In this chapter scanning transmission X-ray microscopy measurements following *in situ* the phase boundary propagation within a LiFePO$_4$ single crystal along the (010) orientation during electrochemical lithiation/delithiation are presented. The defect chemistry of the as-prepared single crystals has already been carefully analyzed in previous publications [53, 55], thus allowing for a detailed analysis and understanding of the observed characteristics. The evolution of a two-phase-front is followed on a micrometer scale with a lateral resolution of 30 nm and with minutes of time resolution. Measurements are performed on a micrometer-sized all-solid-state thin film battery cell with oriented LFP / FP as positive electrode, LiF as electrolyte and Aluminum as negative electrode. The lamella-like battery cell is fabricated by an advanced newly developed SEM/FIB procedure, using rotable 4-axes micro manipulators and Ion Beam Induced Deposition of Platinum (IBID-Pt) to obtain a quasi two-dimensional 250 nm thick and about 10x20 µm wide sample.

The images displayed in the lower right corner of the following pages are thought to be used as a flip-book, visualizing the (de)lithiation of the studied sample. The small time-voltage profiles, also shown in figure 5.5 in more detail, are added to the flip-book as an orientation, so that each picture can easily be assigned to the timeline of the

(dis)charging process. What exactly can be seen in these STXM images and how they come about is described in section 5.3.

5.1 Sample Preparation

5.1.1 Synthesis and characterization of LFP single crystals

In a first step about 15 g of LFP powder has been synthesized according to the procedure described in section 4.1.1 and its purity characterized by XRD, Raman spectroscopy and ICP-OES. The powder is used to form the feed rod for growing LFP single crystals via optical floating zone technique, using a furnace from Crystal System Incorporation and a sequential growth rate of 2 and 4 mm/h under continuous argon flow, as described in reference [62]. To cut out slices with well-defined surface and edge orientations from the obtained LFP-rod of about 80 mm in length and 5 mm in diameter, the single crystalline rod is firstly mounted on a goniometer. Samples with dimensions of a few mm exhibiting surface and edge orientations, controlled by Laue diffraction, of (100), (010), and (001) are then cut off using a fast rotating circular saw. The compositional purity Li:Fe:P:O=1:1:1:4 of the crystals has been verified within the error margins (appr. 1-2 %) by ICP-OES using a Spectro Ciros CCD system from Spectro Analytical Instruments, while the oxygen content has been determined by the carrier gas hot extraction method. Figure 5.1 shows the Laue diffractogram of the (010) orientation together with the corresponding XRD image over the 2-Θ region, confirming the orientation, and a photo of the crystal.

5.1.2 Fabrication of micrometer-sized thin film battery cell

After polishing the surfaces of the obtained oriented LFP single crystals with an oil-diamond suspension and cleaning them consecutively in acetone, iso-propanol and bi-distilled water in an ultrasonic bath for 15-30 min, they are used as substrates to deposit a thin LiF layer of about 100 nm as solid electrolyte under UHV-conditions at a base pressure of $1 \cdot 10^{-10}$ mbar using molecular beam deposition. The evaporation source contains pure LiF and is heated up to 820 °C to provide a beam flux of about
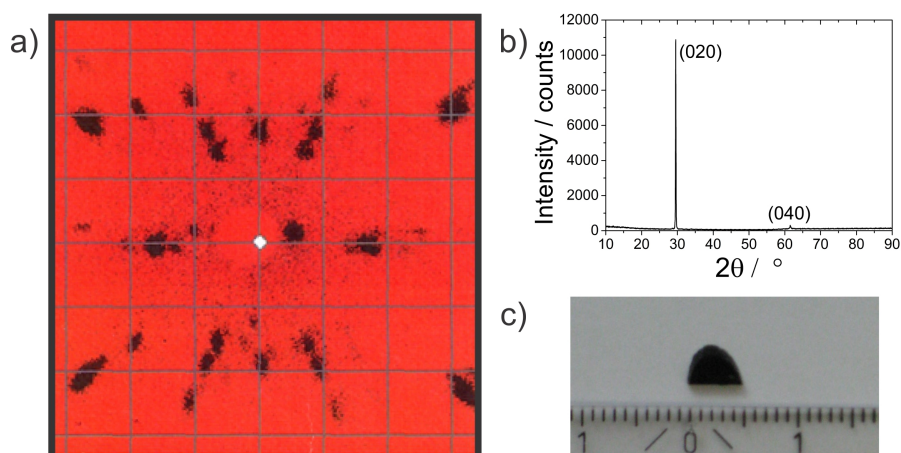
Figure 5.1: LiFePO$_4$ single crystal. a) Laue diffractogram of the (010) orientation, b) XRD image of the same sample over the 2 Θ region and c) Small photo of the crystal.

$5 \cdot 10^{-7}$ mbar, resulting in a growth rate of approximately 0.5 Å/s LiF. During deposition the LiFePO$_4$ single crystals are held at room temperature. In the next step a 400 nm thick layer of aluminum is deposited as anode material on top of the solid LiF electrolyte via e-beam evaporation in a Univex 450 system in N$_2$ atmosphere at a base pressure of about $1 \cdot 10^{-5}$ mbar. The layered sample is then transferred under argon atmosphere with less than 5 minutes of air-contact into a scanning electron microscope (SEM, Zeiss Crossbeam) with built-in FIB (Ga source), a positionable nozzle providing a gaseous organo-platinum precursor and a 4-axes micro manipulator attached at the walls of the SEM-chamber to take up the micro-sized sample and to position and align it in the electron and ion beam, respectively. Using a focused gallium ion beam inside the SEM a gaseous organo-platinum precursor is decomposed on the surface of the layered structure, forming a Platinum bar of about 7 µm thickness. After this ion beam induced deposition of Platinum (IBID-Pt) a 16x16x1 µm lamella sample is cut out of the formation and taken up by a 4-axes micro manipulator, attached at the walls of the SEM-chamber, as shown in figure 5.2 a). To take up the lamella sample, the manipulator is glued with IBID-Pt to it before the lamella is completely cut free from the rest of the sample. From this manipulator the lamella-like sample is transferred to another manipulator, mounted on a standard SEM sample holder, providing more
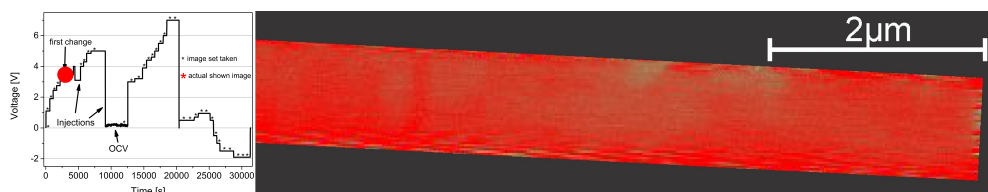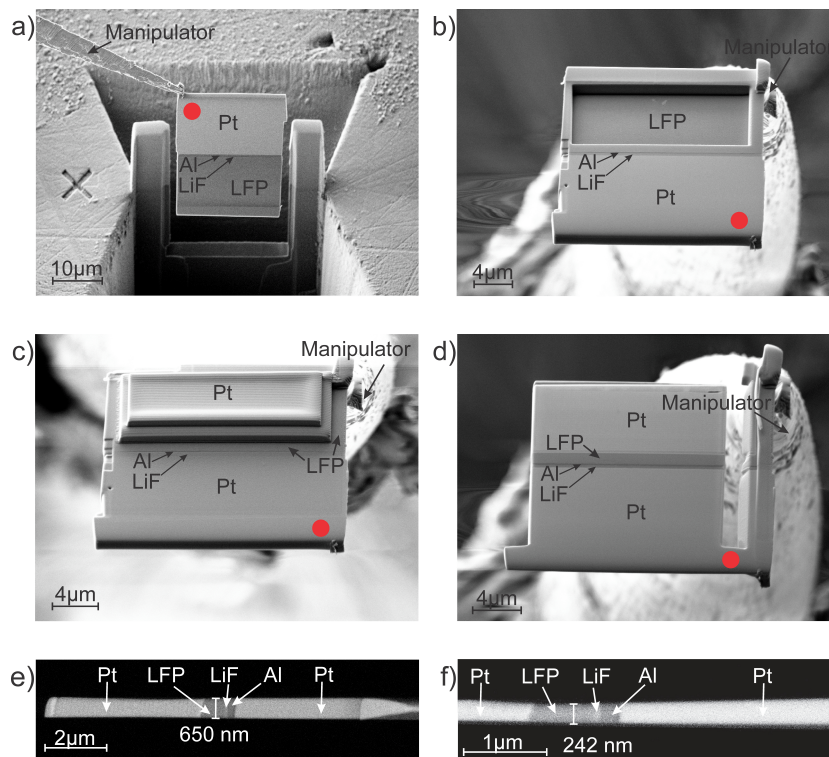
Figure 5.2: SEM images documenting the manufacturing process. The shown SEM images are recorded during fabrication of an all-solid-state thin film battery cell. The red dot in images a)-d) always marks the same position and is added for the readers orientation. a) A Lamella is cut out of the starting material (oriented LFP single crystal with deposited LiF electrolyte and Al anode layer on top) after deposition of a platinum bar on the surface. b) A cuboid cavity is cut in the LFP side of the lamella. c) The cavity is filled up with IBID-Pt. d) Lamella sample after removal of the redundant platinum of the filled cavity by a focused gallium ion beam under grazing conditions and cutting away the edges of the sample. e) Side view of the all-solid-state thin film battery cell after further thinning the lamella to a thickness of 650 nm, removing the LFP-bottom of the former cuboid cavity, providing a multi-layered sample consisting of current collector | cathode | electrolyte | anode | current collector (Pt | LFP | LiF | Al | Pt). f) Side view of the thin film battery sample after thinning it down to its final thickness of about 250 nm. According to Ohmer et al. [198].

stability for further operations. In a next step a cuboid cavity is cut in the LFP part of the structure with dimensions of 15x8x0.6 µm and a distance of 1 µm to the electrolyte, using the FIB with a 50 pA current (see figure 5.2 b)). This cavity is then filled up with IBID-Pt (compare figure 5.2 c)). Here, the nozzle with the gaseous organo-platinum precursor is positioned as close as possible to the sample (distance less than 100 µm) and is carefully adjusted to ensure a sufficient concentration of precursor gas in the cavity when using the focused gallium beam to deposit Pt, not to further cut in the

cavity of the lamella sample. Later, the deposited platinum functions as the current collector on the cathode-side of the battery cell. The protruding platinum is removed by the FIB under grazing conditions, followed by a thinning of the whole sample from both sides, thereby also removing the bottom of the former cavity in the LFP structure, so that a multi-layered sample consisting of current collector | cathode | electrolyte | anode | current collector (Pt | LFP | LiF | Al | Pt) results. The exact angle between the incoming ion beam and the lamella sample has to be carefully readjusted several times upon thinning of the sample to guarantee a homogeneous thinning over the whole length of about 20 µm. After removing the redundant material at the edges of the sample, it is thinned down to its final thickness of about 250 nm by the focused gallium ion beam (compare figure 5.2 d)-f)). The thickness of the sample is chosen to secure
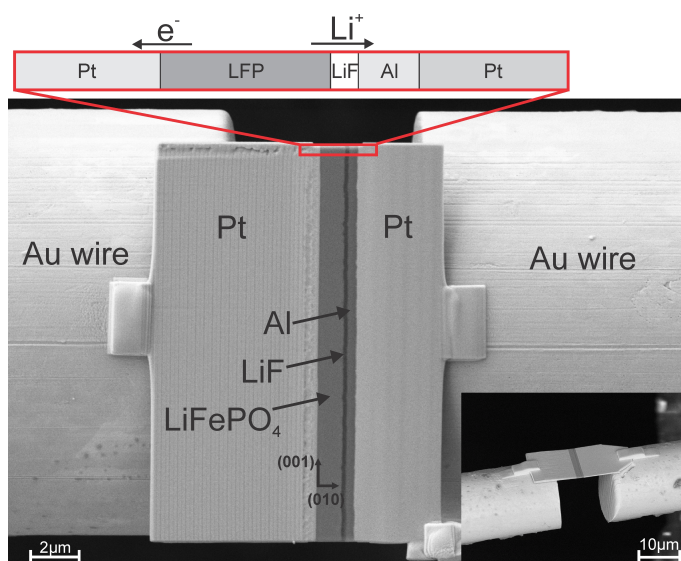
Figure 5.3: SEM image of the micrometer-sized battery. The all-solid-state thin film battery cell is fixed on the ends of two free-standing gold wires. During electrochemical delithiation of the LFP cathode, the electron is transported to the left platinum contact, while the Lithium ion is transported through the electrolyte to the aluminum anode, where it forms a lithium-aluminum alloy. The small inset picture shows a side view of a similar thin film battery cell. Reprinted from Ohmer et al. [198].

the stability of the structure and to provide a high transparency for X-rays in the 700 eV range used for the characterization via STXM. The micrometer-sized all-solid-

state thin film battery cell is then transferred back to the 4-axes micro manipulator, attached at the walls of the SEM-chamber. From here it is placed between the ends of two free-standing 17 µm thick gold wires, as shown in figure 5.3. A distance of several micrometers between the fixing points and the active battery part ensures that no Pt is deposited on the cathode, electrolyte and anode material while fixing the sample, maintaining a clean surface. Beforehand, the two free-standing and well aligned gold wires have been made by cutting a single gold wire, which has been earlier fixed on a 5x5 mm quartz glass over a 1x0.2 mm wide slit with conductive silver, using the FIB (compare figure 5.4). This quartz glass is again glued with a two-component glue on
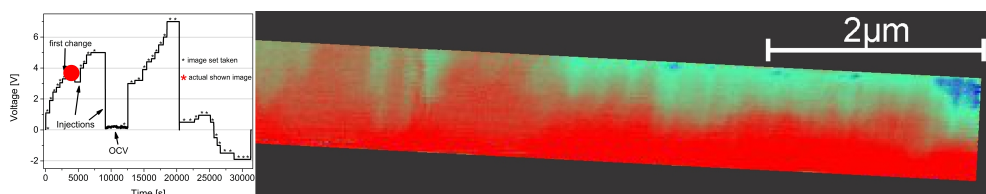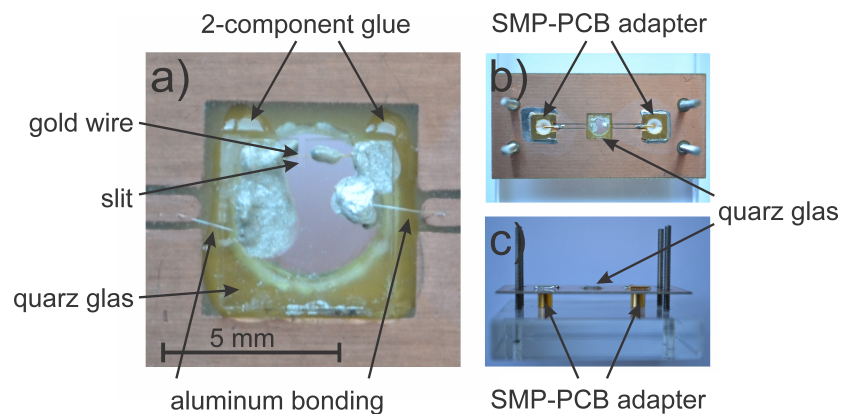
Figure 5.4: Sample holder with mounted micrometer-sized battery. The photographs show a conductor board with mounted sample. a) and b) show the top view of the sample holder, while c) provides the side view.

a conductor board, equipped with two SMP-PCB adapters to electrically contact the sample after using aluminum bonding to connect the two gold wires with the adapters. Figure 5.4 shows a conductor board with mounted sample. It can also be seen in that figure, that the slit in the quartz glass and the sample, respectively, is positioned over a hole in the conductor board, so that the sample can be analyzed by transmission X-ray microscopy. Between preparation and characterization the sample is kept in Ar atmosphere, apart from short periods of time needed for gluing and bonding.

5.2   Sample Characterization

Despite a thorough sample preparation, electronic pathways, most likely originating from Pt contamination, cause non-Faradayic by-pass currents during (dis)charging of the all-solid-state micro-sized thin film battery cell and reduce the OCV to values of $O(100 \text{ mV})$. However, this additional current flow can not influence the (de)lithiation mechanism and neither the mechanistic conclusions.

5.2.1   Electrode capacities

The capacities C_i of the LFP and Al thin film electrodes can be calculated from their volumes V_i, densities ρ_i and theoretical capacities $C_{theo,i}$ via $C_i = V_i \cdot \rho_i \cdot C_{theo,i}$. The volume of the LFP cathode material within the micro-sized battery is $V_{LFP} = 15 \cdot 1 \cdot 0.25 \ \mu m^3 = 3.75 \ \mu m^3$, its density $\rho_{LFP} \approx 3.5 \ \text{g/cm}^3$ and theoretical capacity $C_{theo,LFP} = 170 \ \text{mAh/g}$, resulting in a capacity of the LFP cathode of $C_{LFP} = 2.2$ pAh. The capacity of the aluminum anode calculates from $V_{Al} = 15 \cdot 0.4 \cdot 0.25 \ \mu m^3 = 1.5 \ \mu m^3$, $\rho_{Al} \approx 2.7 \ \text{g/cm}^3$ and a theoretical capacity of up to $C_{theo,Al} = 1 \ \text{Ah/g}$ forming Li_1Al_1 to be $C_{Al} = 4.0$ pAh. So the theoretical capacity of the anode is high enough to be cycled, upon full (de)lithiation of the LFP cathode, within the $(\alpha + \beta)$ two-phase region of the Li-Al phase diagram, which ranges at room temperature from close to 0 up to 50 at.% lithium [181, 182]. The $(\alpha + \beta)$ region is the one, where the Li-Al alloy is typically cycled, exhibiting a voltage plateau of about 350 mV vs. lithium metal [183].

5.2.2   Estimation of additional Joule heating

To determine the operating temperature of the battery cell during charging and discharging, a possible influence of the additional Joule heating on the sample temperature due to the non-Faradayic by-pass currents should be estimated. A safe upper bound for the power input is given by $\dot{Q} = 7 \ \text{V} \cdot 1 \ \mu A = 7 \ \mu W$. Note that the upper limit of the power input of the X-ray beam, estimated from the count rate without a sample
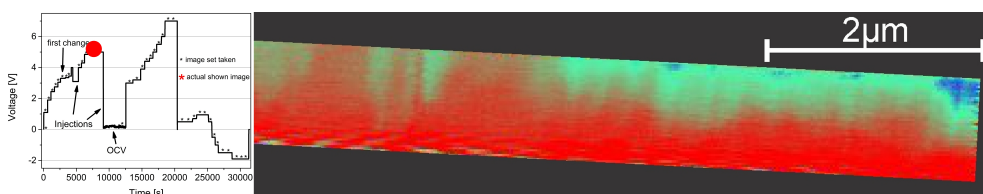
in the optical path ($\approx 10^6$) and the photon energy (700 eV), is only on the order of 10^{-10} W. The bottleneck for the dissipation of heat generated by joule heating is the transport through the approximately $2 \cdot d = 10$ µm long and 250 nm thick all-solid-state thin film battery cell, having a cross section area of $A \approx 15 \cdot 0.25$ µm$^2 = 3.75$ µm^2. Taken the thermal conductivities λ of the used materials $\lambda_{Pt} = 71.6$ W/m·K [199], $\lambda_{Al} = 237$ W/m·K [200], $\lambda_{LiF} = 14.2$ W/m·K [201], and $\lambda_{LFP} = 3.75$ W/m·K [202] into account, the simplified Fourier law of thermal conduction $\dot{Q} = \frac{\lambda}{d}A\Delta T$ is used to estimate the increase in temperature ΔT of the sample. Although the above-named thermal conductivities are for solid bulk materials and not for deposited thin films - especially the IBID-Pt should have a lower value than the cited one - a reliable lower bound of an averaged thermal conductivity over the hole length of the layered sample is given by λ_{LFP}. Hence, the temperature increase due to additional Joule heating is securely smaller than $\Delta T = 2.5$ K. Therefore, the additional current flow can neither influence the observed (de)lithiation mechanism, nor can it noticeable heat the sample above room temperature.

5.3 Results

Fe $L_{2,3}$ edge spectra are taken at the MPI-IS endstation "MAXYMUS", tracking the change in the iron oxidation state or rather local lithium concentration within the cathode material of the micrometer-sized all-solid-state thin film battery *in situ* upon electrochemical (de)lithiation. Both full absorption spectra at energies of 704-715 eV and area scans before the edge jump (704 eV) and at the centroids of the respective Fe^{2+} (708.7 eV) and Fe^{3+} (710.6 eV) Gaussian XANES contributions are recorded to visualize the phase evolution.

5.3.1 STXM mapping during (de)lithiation

All STXM measurements are performed at a pressure of $< 1 \cdot 10^{-7}$ mbar and the shift in the main absorption feature from around 708 to approximately 710 eV upon delithiation is used to fingerprint the change in the local state of charge as described in subsection 2.3.2. Charging and discharging of the all-solid-state micro-sized battery is

done potentiostatically by a stepwise change of the applied voltage using a Keithley 2634B System SourceMeter, which can reliably source and measure currents of 1 pA and smaller (voltage accuracy is in the micro-range) [191]. Figure 5.5 shows the time-voltage profile of one of the studied battery cells, whose (de)lithiation sequence will be further analyzed below. The black asterisks in figure 5.5 mark, where image sets
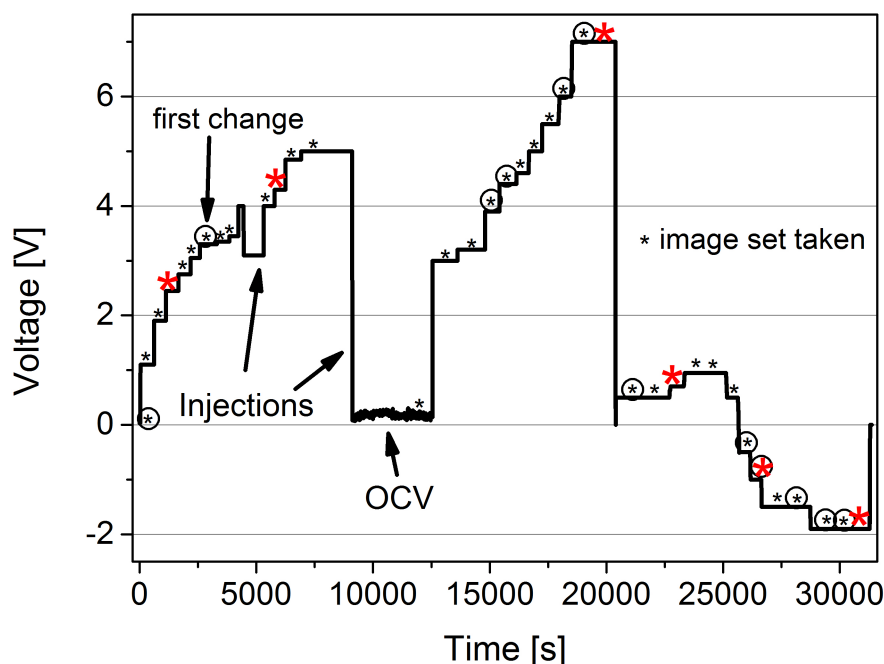

Figure 5.5: Time-voltage profile of charging and discharging the all-solid-state micro-sized battery cell. The black asterisks mark where an image set consisting of 3 images, taken at energies of 704, 708.7 and 710.6 eV is recorded. The red asterisks mark the image sets displayed in figure 5.6, while the image sets marked with a circle are used for the line scan analysis in figure 5.9. During delithiation the X-ray beam has been disrupted two times, while new electrons were injected into the storage ring. These times are marked by "Injections". Reprinted from Ohmer et al. [198].

of 3 images, taken at energies of 704, 708.7 and 710.6 eV, are recorded. The scans are done on a 7·2 μm^2 area with a 20 nm step size, a dwell time at each point of about 1 ms, a line delay (uni-directional scan) of 250 ms and a 30 nm focus of the X-ray beam. Together with other waiting times such as for the piezo motors and the monochromator to change the energy, the total time to acquire 1 set of images is about
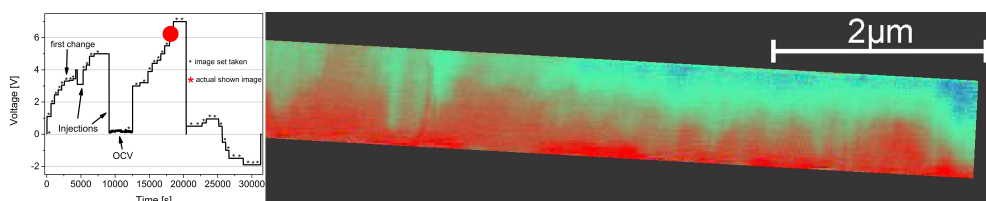
8 minutes. The first necessary step of data processing is to well-align these 3 images to each other, because of small shifts of the sample in the beam over time. Then the absorbance at each point of the sample is calculated for 708.7 and 710.6 eV according to $lg\left(\frac{I_{704}}{I_{708.7}}\right)$ and $lg\left(\frac{I_{704}}{I_{710.6}}\right)$, respectively. Dividing the two absorbances at each point of the sample by each other, the transition between the two oxidation states and therefore the (de)lithiation of LiFePO₄ can be followed unambiguously, analyzing the resulting images. During the (de)lithiation cycle shown in figure 5.5, 37 image sets are recorded, documenting the (de)lithiation process of the oriented single crystalline LFP cathode material along the fast (010) direction. The as-described processed image sets result in the images shown in the lower right corner of the pages of this chapter, to enable the reader to follow the charge and discharge process as a flip-book. A colour-coding is used in which the lithium content decreases from red (LFP) over green to blue (FP) (compare figure 5.6). Six out of these 37 processed image sets (red asterisks in figure 5.5) are also shown in figure 5.6 for a detailed analysis of the (de)lithiation process. Another 12 images (encircled image sets in figure 5.5) are chosen for the line scan analysis to study the mechanism and morphology of the evolving electroactive phases (compare figure 5.9), and are discussed in subsection 5.3.3.

It is obvious from the images shown in figure 5.6, that the sample has not been completely delithiated before reversal of the current (see remaining red areas). This is done due to the fact that at a voltage of 7 V a first crack is found in the sample encircled in figure 5.6 c) and shown in figure 5.7. Further delithiated micro-sized all-solid-state battery cells document the appearance of several cracks (compare figure 5.7). Therefore, to prevent an irreversible fragmentation of the sample, delithiation is stopped at this stage. The phenomena of crack formation will be further discussed in subsection 5.3.4. Besides area scans of the sample, also full absorption spectra are recorded at differently (de)lithiated positions of the sample. The absorption spectra shown in figure 5.6 are recorded at a fixed voltage along a line perpendicular to the LFP | FP phase front in intervals of 80 nm, illustrating the LFP delithiation along the (010) direction by presenting a constant increase in Fe^{3+} concentration. A typical parameter set performing full absorption spectra include an energy range from 704-726 eV with energy steps of 0.1 eV, a dwell time per energy step of 1000 ms and a
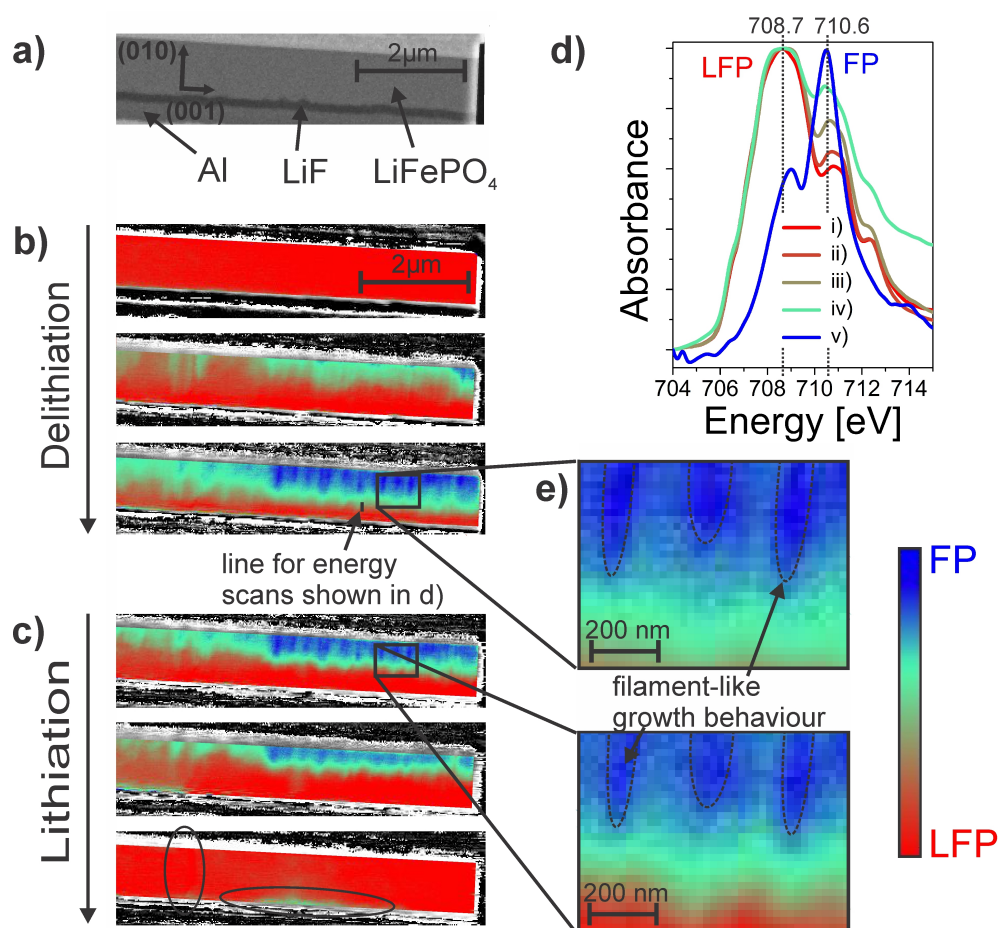
Figure 5.6: STXM images showing the filament-like growth behavior. a) SEM image of the analyzed region before performing STXM measurements. b,c) STXM images comparing the optical densities of the sample at 708.7 eV and 710.6 eV with each other during electrochemical delithiation (b) and lithiation (c). The region of interest is color-coded going from red (LiFePO$_4$) over green to blue (FePO$_4$). In the lowest image in c) the begin of a crack formation along the (001) plane as well as the reversal of the Li concentration gradient upon lithiation are encircled. d) Energy spectra taken across the borderline of the phase front along the (010) direction with i) being recorded in the still pure LiFePO$_4$ zone, while ii)-iv) are recorded in intervals of 80 nm across the phase front (indicated in the lowest image in b)) and v) showing an energy spectrum of a fully delithiated sample with the expected absorption features of FePO$_4$. The color-coding of the energy spectra are done according to the STXM images b) and c). e) Enlarged region of two STXM images to point out the filament-like growth behavior of FP in LFP (upper image) and the rather homogeneous receding of FP in LFP (lower image). Reprinted from Ohmer et al. [198].
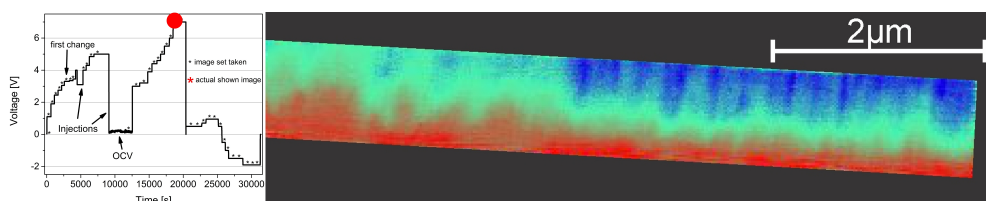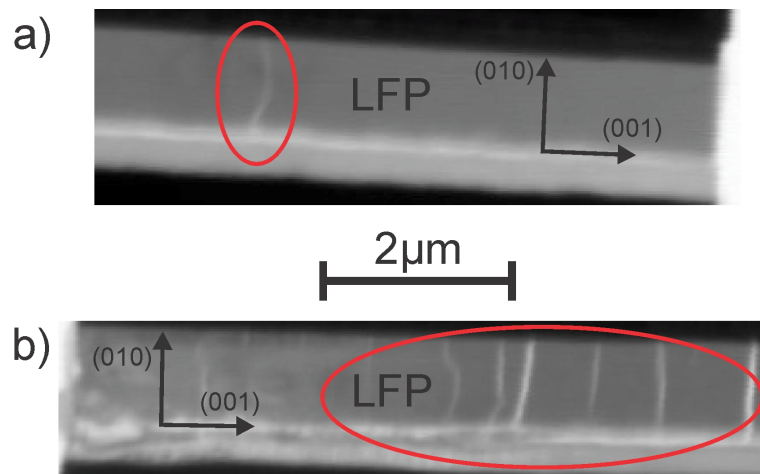
Figure 5.7: Crack formation. STXM images at 704 eV of a) the studied sample and b) a further delithiated sample of same orientation. The cracks are encircled in red and oriented along the (001) plane. Reprinted from Ohmer et al. [198].

defocus of the X-ray beam between 100 and 200 nm. The various energy spectra enable one to assign to the differently color-coded regions in figure 5.6, as well as to the line scans presented in figure 5.9, the averaged lithium concentrations along the direction of the X-ray beam. To do so, first absorption spectra of an as-prepared sample and a fully delithiated sample are taken as references. Then, after normalization, the absorption spectra recorded at different positions of the samples at different applied voltages are fitted by a linear combination procedure of the two reference spectra. Afterwards the corresponding averaged lithium concentrations are assigned to the positions on the sample where the absorption spectra have been recorded and are synchronized with the corresponding color-code. Thus, in the images shown in figure 5.6 and the ones in the lower right corners of the pages of this chapter, the red regions correspond to pure LFP, while green and blue areas are indicative for material of lower averaged lithium concentration (see color scale in figure 5.6).

The two main characteristics of any (de)lithiation process of a phase separating electrode material for lithium batteries can be seen in figure 5.6. First: the position of the sample where delithiation and, upon current reversal, lithiation starts. Second: the profile of the phase-front of the electroactive phases. FePO$_4$ forms upon delithiation at the current collector side, rather than at the electrode - electrolyte interface. The evolving FP phase does not form a homogeneous phase front over the whole length

of the sample but rather a morphology of a filament-like growth behaviour developing along (001) and growing along (010) and (100). Upon lithiation of the (partly) delithiated cathode, growing of the LiFePO₄ region starts at the electrolyte side under a homogeneous withdrawing of the FP phase. Before the growth morphology is studied in more detail in subsection 5.3.3 and a defect chemical analysis is presented in subsection 5.3.4 to understand why the (de)lithiation occurs in this way, it is shown in the next subsection that the growth time of the filaments is fast in comparison to the time resolution of the experiment and hence the response to the voltage steps is reflected by a quasi-stationary morphology.

5.3.2 Assessment of the growth time

Assuming a chemical transport behaviour, the lithium flux in the one-dimensional transport problem is given by $j = -\frac{1}{LF^2} \int \sigma^\delta d\mu_{Li}$ [203], neglecting interfacial and space charge effects. Together with the mass-balance expression $j = \frac{1}{V_m} \frac{dL}{dt}$ it follows that $\frac{dL}{dt} = -\frac{1}{L} \frac{V_m}{F^2} \int \sigma^\delta d\mu_{Li}$. Approximation of the ambipolar conductivity σ^δ, taking the transport of Li$^+$ through LFP and e$^-$ through FP into account, by the averaged conductivity, i.e. $\int \sigma^\delta d\mu_{Li} \rightarrow < \sigma^\delta > \Delta\mu_{Li}$, gives $\dot{L} = -\frac{1}{L} \frac{V_m}{F^2} < \sigma^\delta > \Delta\mu_{Li}$. The molar volume of FP is given by $V_m = 41$ cm³/mol [24] and approximation of $< \sigma^\delta >$ with the lower bound of the rate determining conductivity, given by the electron conductivity in LFP, results in $< \sigma^\delta > = 10^{-7}$ S/cm (taken from [58] for comparable Al doped LFP). For a voltage step of 1 V, $\Delta\mu_{Li}$ is on the order of 10^5 J/mol so that $\dot{L} = \kappa \cdot \frac{1}{L}$ with $\kappa \approx 4.1 \cdot 10^{-11}$ cm²/s. For a movement of the LFP - FP phase front of L = 100 nm the phase front motion is approximately $\dot{L} \approx 41$ nm/s. So the equilibration time for a voltage step of 1 V, inducing a movement of the phase front by 100 nm, is on the order of a few seconds. Certainly the growth process is more exactly a drift diffusion problem involving elastic fields. Hence, one might expect that the real growth time is even distinctly smaller and therefore out of time resolution of the experiment, which typically needs several minutes to record one set of images. Figure 5.8 illustrates the quasi-stationarity of the morphology at a given voltage step by comparing the absorbance
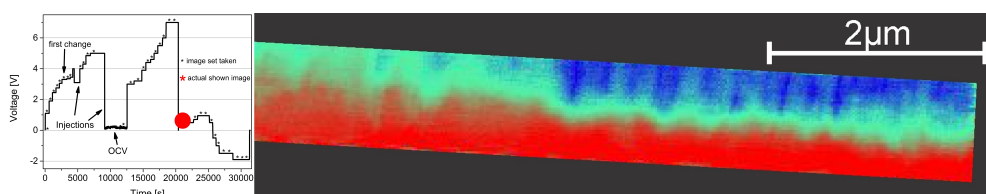
of the cathode material recorded at a first voltage step at 6 V with the absorbance of the sample at a second voltage step at 7 V and the change between two consecutively performed scans at 7 V.
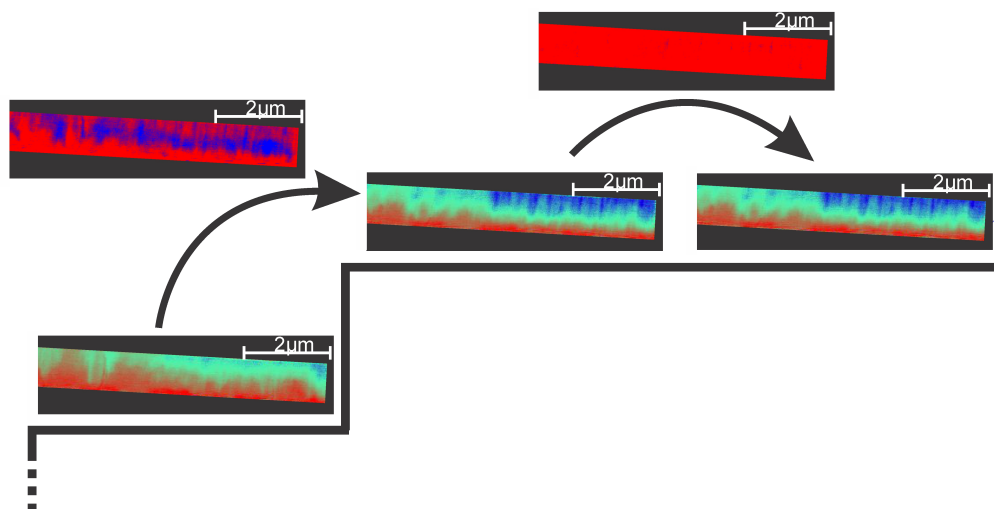

Figure 5.8: Quasi-stationarity of the growth morphology. STXM images comparing the optical densities of the sample at 708.7 eV and 710.6 eV with each other during electrochemical delithiation, recorded at constant voltages of 6 V (1 image) and 7 V (2 images), respectively. The pictures above the arrows are received by dividing the two succeeding STXM images by each other, whereby blue indicates a change in contrast and therefore in lithium content, illustrating the quasi-stationarity of the morphology at a given voltage step. Reprinted from Ohmer et al. [198].

Dividing each two succeeding STXM images by each other, resulting in the pictures above the arrows in figure 5.8, reveals a significant change between the absorbances recorded at 6 and 7 V (blue indicates a change in lithium concentration) and nearly no change between the two scans at the same voltage step of 7 V (red indicates no change in lithium concentration). Hence, the growth time of the filaments appears to be too fast to be able to record a more detailed transient response at a given voltage step.

5.3.3 Growth morphology of the evolving electroactive phases

In this subsection the growth morphology of one representative evolving FP filament is studied in terms of time and applied voltage steps, respectively. To do so, line scans have been taken along the evolving filament in several STXM images. The corresponding lithium concentrations along this filament during (de)lithiation are determined and shown in figure 5.9 a)-c). Before the line scans and the proposed corresponding cross
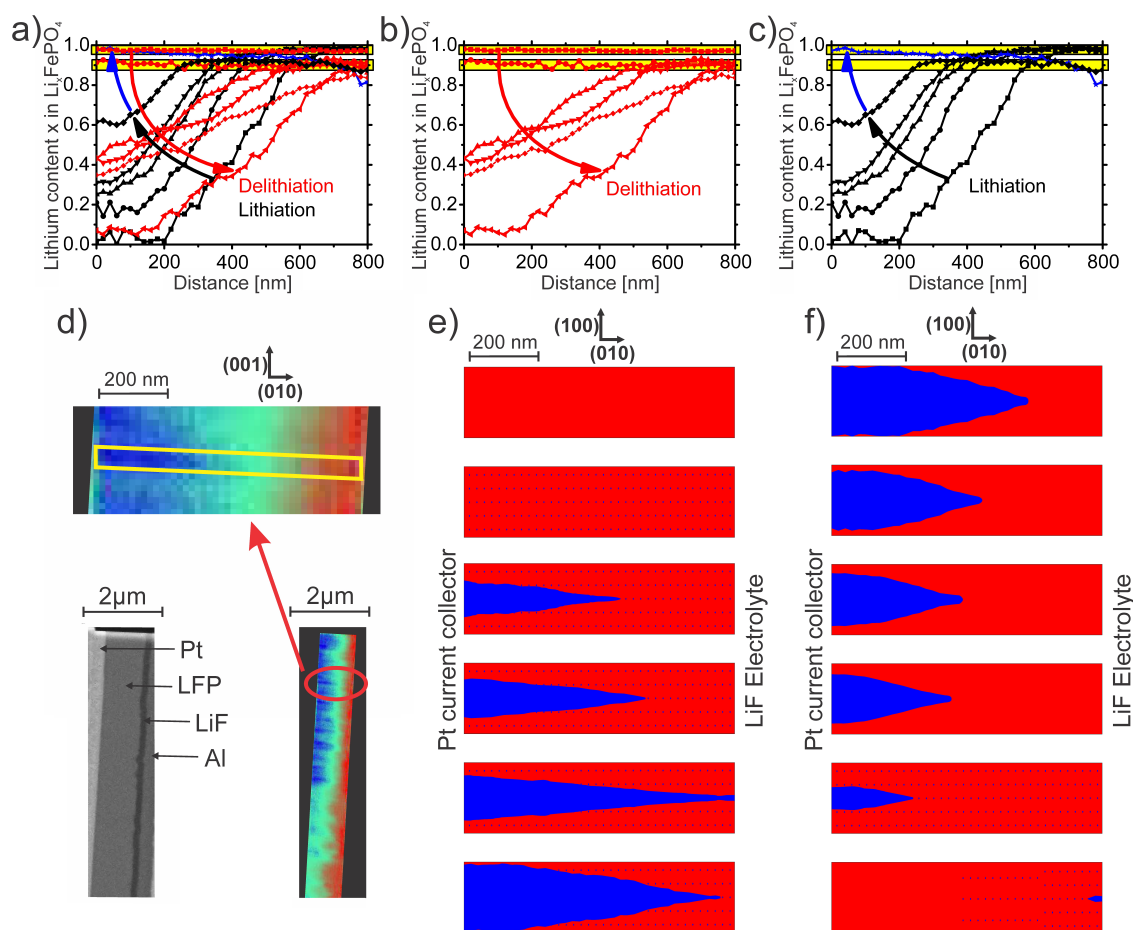
Figure 5.9: Growth morphology of a filament. a)-c) Line scans taken at the evolving filament shown in d), giving the lithium content of the sample along the filament during delithiation (red lines in a) and b)) and lithiation (black lines in a) and c), as well as the blue line showing the final state of the sample, including the reversal of the Li concentration gradient). e) and f) show cross sections of the sample at a given position of the (001) direction where the line scans have been performed (see d)). For simplicity a symmetric filament evolution along the (100) direction is assumed during delithiation e) and lithiation (f)). Red areas indicate LFP, blue areas FP, and the blue dots in the red areas dissolved FP. Reprinted from Ohmer et al. [198].

sections, shown in figure 5.9 e)-f), are further discussed, it should be pointed out again, that as a matter of principle no direct local information about the lithium distribution along the direction of the X-ray beam (**a** direction) are provided by the STXM measurements.

Following the line scan analysis in figure 5.9, the (de)lithiation process is subdivided into the following steps. First, the lithium concentration is lowered over the whole
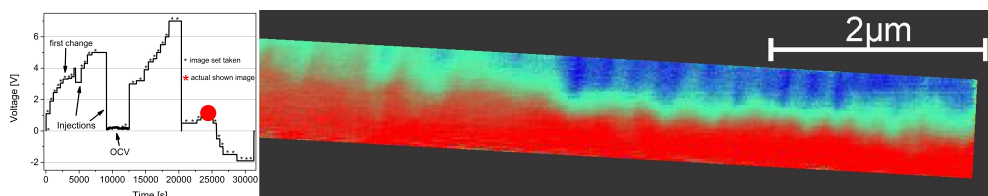
length of the cathode from 100 % to about 90 %. This two concentration-regions are marked in yellow in figure 5.9 a)-c). A measured average lithium concentration of 90 % is in agreement with the solubility limit of FP in LFP, which is reported to be up to 10 % at room temperature [13, 86, 89, 90, 91]. With increasing voltage, the FP filament starts to grow at the Platinum current collector side. The growth is targeted mainly along the (010) direction and becomes only more pronounced along (100) direction when it reaches the LiF electrolyte side, while the concentration of dissolved FePO$_4$ in the LiFePO$_4$ phase remains constant at about 10 %. This growth behaviour can well be understood by the different ionic conductivities along **a** and **b** direction [53, 55, 60], and is visualized by cross sections of the cathode material at the position along (001) where the line scans have been taken (see figure 5.9 e)). The red areas in figure 5.9 e) and f) indicate LiFePO$_4$, blue areas FePO$_4$, and the blue dots inside the LiFePO$_4$ phase dissolved FePO$_4$. The assumption of such an inhomogeneous lithium distribution along **a** is supported by the absence of pronounced kinks in the lithium concentration along **b**. For simplicity, the proposed cross sections in figure 5.9 e) and f) depict a symmetrical single-filament growth behaviour along **a** direction during (de)lithiation. Reaching 7 V and observing the first crack in the sample, the cathode is lithiated again. In the first step of lithiation as shown in figure 5.9 c) and f), the Li concentration in the LiFePO$_4$ phase increases to nominally 1 and the FP filament recedes again, starting at the LiF electrolyte side. As during delithiation, the extension of the FP filament changes again fast along **b** and slower along **a** direction. Before the whole cathode material is converted back to LiFePO$_4$, again about 10 % of FP is found to be dissolved along the entire length of the cathode material inside the LFP phase, and the last part of the FP filament appears to be dissolved in the LFP phase. After final lithiation a stoichiometry polarization is found in the cathode material. Obviously some of the removed lithium is still stored in the originally pure aluminum anode, forming upon cycling a LiAl alloy, known for its poor cycleability [204], preventing a complete reversible lithium transfer.

5.3.4 Defect chemical analysis and elastic effects

In this subsection the phase formation and growth morphology is discussed in terms of ionic and electronic transport properties of the involved electroactive phases as well as elastic effects. As is pictured in figure 5.10, it is the ionic ($\sigma_{ion}(LFP)$) and electronic ($\sigma_{eon}(LFP)$) conductivity in LFP and their ratio that determines on which side of the sample the FP phase formation starts.
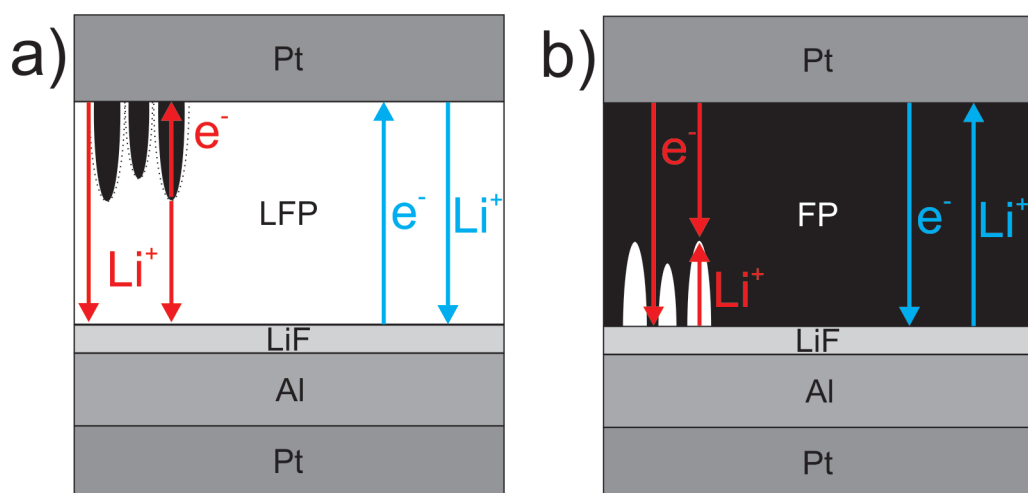

Figure 5.10: Illustration of the phase formation requirement. This figure shows a scheme for the delithiation of LFP (a) and lithiation of FP (b). The blue arrows in the images indicate that $\sigma_{eon}(\text{LFP})$ vs. $\sigma_{ion}(\text{LFP})$ (a) and $\sigma_{eon}(\text{FP})$ vs. $\sigma_{ion}(\text{FP})$ (b) determines on which side of the sample the (de)lithiation starts. The red arrows in both pictures clarify, that for a transport controlled (de)lithiation one would expect homogeneous growth of FP in LFP, while filament-like growth of LFP in FP, since $\sigma_{ion}(\text{LFP}) > \sigma_{eon}(\text{FP})$. Reprinted from Ohmer et al. [198].

For an ideal intrinsic material, where no anti-site defects are present, a faster ionic than electronic transport $\sigma_{ion}(\text{LFP}) > \sigma_{eon}(\text{LFP})$ is expected. Nevertheless, due to prevention of ideal channel transport by anti-site defects in realistic LFP materials (compare section 1.2), for the same LFP single crystal, the micro-sized battery cell is built of, a predominant electronic conduction has been measured along **b** at T > 400 K [15, 53, 205]. Hence upon delithiation the FP phase is expected to form at the electrode - electrolyte interface. Instead, the phase formation is observed at the electrode - current collector side, which indicates a faster ionic than electronic transport
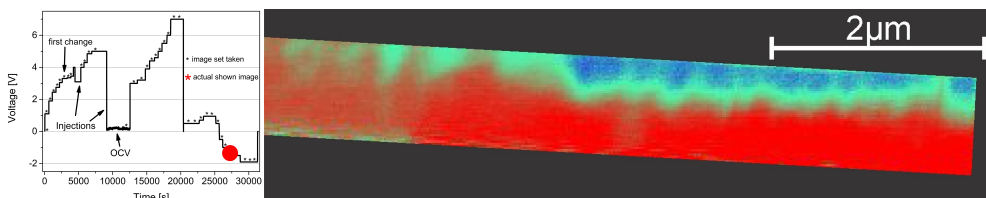
σ_{ion}(LFP) $> \sigma_{eon}$(LFP). Since the anti-site defect concentration of the starting LFP single crystal is about 2.5-3.0 % [53], the studied dimension of about 1 µm is well above the effective distance between two anti-site defects (compare figure 1.6 and reference [15]). Therefore the reason for the observed phase formation has to be sought in the nano-processing during sample preparation and the measurement conditions. Upon shaping the all-solid-state micro-sized battery cell with the FIB, the sample is doped with Gallium atoms from the beam. It should be mentioned here, that such an extrinsic effect does not undermine the significance of a defect chemical interpretation, but rather does good service in defining the defect chemical regime of the studied material. The Ga dopants act as donors regardless of sitting on an iron side ($Ga_{Fe}^{\cdot}$), lithium side ($Ga_{Li}^{\cdot}$) or an interstitial ($Ga_i^{\cdot\cdot\cdot}$). The effect of donor-doping a p-type electronic and Li-vacancy ionic conductor, such as LFP, on the different conductivities can be predicted by a look at the Kröger-Vink diagram, shown in figure 5.11. Increasing the donor
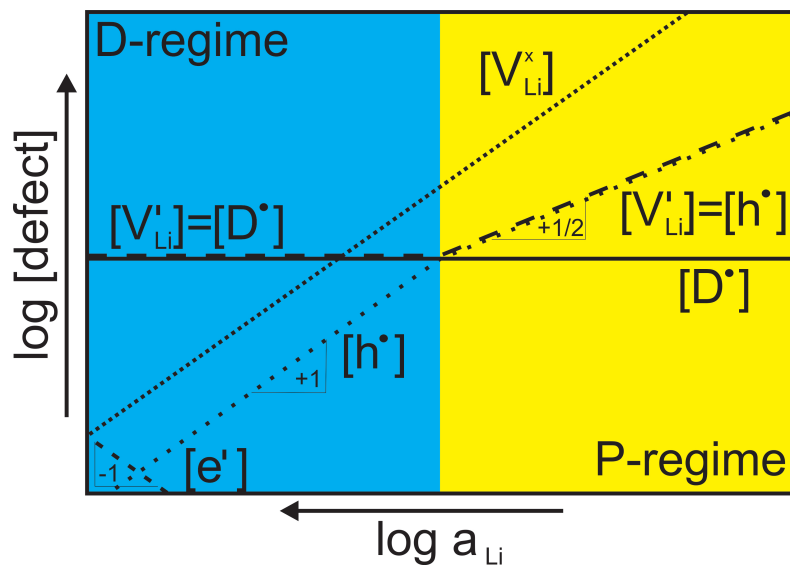
Figure 5.11: Kröger-Vink diagram. Illustration of the defect concentration as a function of lithium activity in LFP (according to [52]).

concentration, being equivalent to go further to the left in the Kröger-Vink diagram, decreases the hole concentration [$h^{\cdot}$], while the lithium vacancy concentration [V_{Li}'] is approximately fixed by the dopant, as already discussed in subsection 1.2.2. This behaviour results in an increased ionic and decreased electronic conductivity, as proven by Amin et al., measuring the different ionic and electronic conductivities of a 1 %

Al donor-doped LFP single crystal [57, 58]. Furthermore the predominant electronic conductivity in single crystalline LFP as determined by Amin et al. in [53] has been measured at T > 400 K, while the STXM measurements presented here have been carried out at around 300 K. The lower measurement temperature increases the trapping of holes by lithium vacancies, decreasing hole concentration and thereby electronic conductivity, while leaving the Li-vacancy type ionic conductivity nearly unchanged, since $[V'_{Li}]$ is fixed by the dopant concentration. Subsumed, the FP phase formation can be understood in terms of ionic and electronic conductivity in LFP, taken the defect chemical donor effect and measurement temperature into account.

As indicated by the blue arrows in figure 5.10 σ_{eon}(LFP) vs. σ_{ion}(LFP) determines the location of the FP phase formation in LFP, while σ_{eon}(FP) vs. σ_{ion}(FP) decides on the LFP phase formation in FP. As already discussed in subsection 1.2.2, while LFP is a p-type electronic and Li vacancy type ionic conductor, FP is a n-type electronic and Li-ion conductor. Hence, gallium doping further increases the electronic and decreases the ionic conductivity in FP, since Ga acts either as a donor $Ga_i^{··}$ or is not electrically active at all (Ga_{Fe}^x). Thus, the development of the LFP phase from the electrode - electrolyte side can also be understood in terms of ionic and electronic conductivity, this time in FP.

Even more interesting than the position of phase formation is the morphology of the evolving phases. As illustrated in figure 5.10 the criterion for a transport controlled growth morphology is formed by the ratio of ionic to electronic conductivity in the two different phases LFP and FP (σ_{ion}(LFP) / σ_{eon}(FP)). According to literature [53, 54] and the previous considerations the ionic conductivity along the b-axis in LiFePO₄ is expected to exceed the electronic conductivity in FePO₄, resulting in a homogeneous growth of FP in LFP if transport controlled. Surprisingly, upon delithiation the FP grows filament-like along the fast (010) direction. Although small non-uniformities of the sample and of the local driving force, respectively, can not completely be excluded, the lattice parameter change upon delithiation and the elastic effects, originating in this context, provide a straight forward explanation. As summarized in subsection 1.2.1,
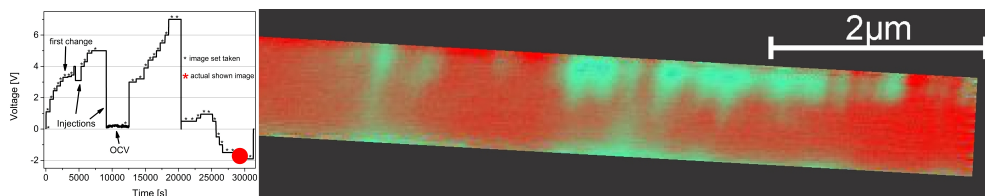
the lattice parameters of LFP in the Pnma space group change from a = 10.334 Å, b = 6.008 Å, and c = 4.693 Å, upon delithiation to FP to a = 9.821 Å, b = 5.792 Å, and c = 4.788 Å[24]. Obviously, the LFP lattice shrinks upon delithiation along **a** and **b** direction, while it expands along **c**. Since sample expansion is restricted along **c** (compare figure 5.3), elastic effects favor an exclusion zone around the forming FP nuclei, preventing further FP phase formation within the vicinity and hence causing a growth pattern characterized by almost regularly spaced filaments. Due to the elastic strain, further increasing upon delithiation of the cathode material, the overvoltage necessary for continuing FP phase propagation increases to values well beyond what is expected from a pure change of the electrical resistance. Therefore, this increase in elastic strain is the reason for reaching the quasi-stationarity of the morphology at given voltage steps, documented in figure 5.8, as well as the increased stress causes crack formation as shown in figure 5.7. Such a crack formation is consistent with the reported irreversible phase fragmentation in large LFP single crystals [68]. Further-more, the observed spacing between single filaments of about 200 nm is in the same dimension at which Boesenberg et al. reported the appearance of mechanical failure in single crystalline LFP cathode material upon cycling [206] and can be seen as the reason for the often observed performance increase during cycling due to a kind of self-optimization of the microstructure upon particle disintegration [207]. Finally, the observed spacing between single filaments is on the same order of magnitude as the reported and simulated domain sizes in hydrothermally grown plate-like $Li_{0.5}FePO_4$ crystals [80]. Hence, the filament-like growth behaviour and phase propagation of FP in LFP is not dictated by transport properties, but can well be understood in terms of elastic interactions within the sample, being the reason for several already earlier in literature reported phenomena.

To prevent an irreversible fragmentation of the cathode material, delithiation is stopped at an applied voltage of 7 V and the cathode material is lithiated again. While the position of the LFP phase formation is in line with the ratio of electronic to ionic conductivity in FP (σ_{eon}(FP) / σ_{ion}(FP)) and can therefore be understood in terms of defect chemistry, the growth morphology can again only be understood by taking elastic interactions into account. As illustrated in figure 5.10 the criterion for a transport

controlled growth of LFP in FP is given by the ratio of ionic conductivity in LFP to electronic conductivity in FP (σ_{ion}(LFP) / σ_{eon}(FP)). Since it is σ_{ion}(LFP) $> \sigma_{eon}$(FP), a filament-like growth of LFP is expected, but instead a rather homogeneous receding of FP is observed (compare figure 5.6). This is due to the already described elastic interactions, also hindering a preferred lithiation in between two FP filaments, resulting in the observed homogeneous motion of the LFP - FP phase front.

Summarizing this point: while the comparison of the respective electronic and ionic conductivities predicts correctly at which interface lithiation and delithiation occur, the growth patterns do not follow the prediction for a transport controlled process, but they turn out to be elastically dominated, which allows one to give an upper grain size limit for a stationary particle morphology without phase separation in the order of 200 nm.
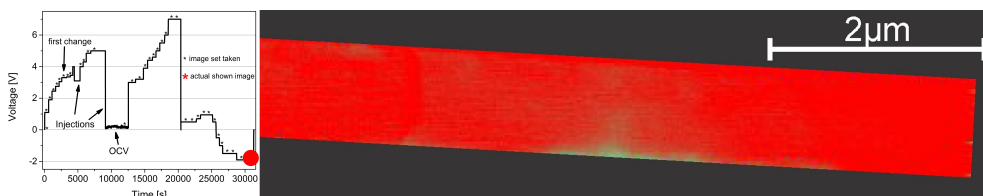
Chapter 6

Summary and Conclusions

In situ STXM measurements on LFP thin films and single crystals reveal the importance of mechanical interactions on the overall phase evolution upon cycling. While Meethong et al. already reported on the role of nanomechanics on the battery performance in terms of rate capability [208] and Dreyer et al. modeled the influence of mechanical interactions on the corresponding charge and discharge curves (compare figure 4.15 in subsection 4.4.5) [192], the overall importance of these mechanical phenomena for the mechanism of phase transformation seems to be largely underestimated and plays only a marginal role when it comes to models for the LFP phase transformation mechanism in literature. In contrast, for the studied micrometer-sized LFP single crystal the growth pattern is found to be dominated by elastic effects, while for the LFP thin film mechanical interactions seem even to be responsible for a change in phase evolution from a particle by particle and phase separating to a concurrent and solid solution mechanism.

The main results of the three parts of this thesis are briefly summarized in the following sections.

6.1 LFP Powder

A combination of integral and lateral resolved methods is used to study a full LFP multi-particle electrode, with hydrothermally grown LFP as active material, at different states of charge to shed some light on the (de)lithiation mechanism within a real

electrode. XRD and XANES measurements are used as integral methods, recording the overall LFP/FP phase and lithium distribution within the electrode, respectively, whereat a combination of FY and TEY measurements allows one to distinguish between lithium concentration in the bulk and at the surface of the particles. EELS and HRTEM measurements are performed on differently sized particles to differentiate between the cycling behaviour of larger and only some ten nanometer big particles.

XRD measurements reveal that the majority of large particles participates in the charge-discharge process and the unit cell parameters, obtained from Rietveld analysis, confirm a 2-phase mechanism. The results obtained from X-ray absorption, reflect both the SEI formation on the lithium anode upon charging, as well as a core-shell mechanism in the particles upon cycling of the electrode. EELS spectra indicate that particles smaller than 100 nm show a deviant cycling behaviour and seem not to participate in the charging process, despite their higher lithium chemical potential. A comparative study of these particles with larger particles by HRTEM identifies a turbostratic stacking of layers in the small particles as the origin of this loss in practical capacity, due to a disturbance and eventually blocking of the 1-dimensional lithium transport channels and an impair of lithium transport along the other directions in the olivine structure. This study reveals the importance of optimizing the synthesis conditions for LFP electrode materials not only in terms of particle size, morphology and phase purity, but also in terms of a possible formation of size-dependent higher dimensional defective structures, to obtain high reversible capacities.

6.2   LFP Thin Film

An all-solid-state thin film battery cell with a lateral design concept is developed and realized by PLD and thermal evaporation techniques, using shadow masks to sequentially deposit the LFP cathode, LVSO electrolyte and LiAl anode material at the predefined locations. Deposited on a X-ray transparent Si_3N_4 membrane, the LFP thin film electrode is studied *in situ* by synchrotron-based energy resolved STXM during electrochemical charging of the battery. The lithiation mechanism is followed by performing absorption measurements at the Fe L_3 edge, using the shift in the main

absorption feature upon lithium exchange to identify areas containing Fe^{2+} and Fe^{3+} and the corresponding local state of charge with a lateral resolution of 30 nm.

The observed initial lithiation process does not follow the classical particle by particle mechanism, described by Dreyer et al. [99] and confirmed for multi-particle LFP powder samples [98], but instead a rather simultaneous, although inhomogeneous lithiation prevails. The reason for this change in mechanism, compared to multi-particle powder electrodes, to a largely concurrent mechanism with alternating active regions for the lithiation is found in mechanical interactions within the LFP thin film. These interactions, originating from the volume expansion of the individual grains upon lithium uptake and the associated formation of high energy surfaces, lead to a tipping of the lithium chemical potential in each individual grain during the lithiation process to a monotone form, making it energetically unfavorable to sequentially completely lithiate single grains within the thin film. In other words, the shape of the single particle chemical potential is changed to a monotone form, leading i.a. to an expected charge-discharge profile without a pronounced hysteresis loop and hence to a higher battery efficiency. It furthermore implies, that the lithiation of the LFP thin film and the individual particles (grains) therein, is also changed from a two-phase to a single phase mechanism during lithiation, minimizing the occuring mechanical stress. These findings are rather general and applicable to all kind of thin films of phase separating intercalation materials, undergoing a volume change upon lithium exchange.

6.3   LFP Single Crystal

Using SEM/FIB, a micrometer-sized all-solid-state battery is built, exhibiting a defect-chemically well characterized and oriented LFP single crystal as cathode, LiF as electrolyte and Al as anode material. The reversible electrochemical delithiation of LFP and lithiation of FP is followed *in situ* on a micrometer scale with a lateral resolution of 30 nm along the fast (010) direction by energy resolved STXM. The known defect chemistry and orientation of the used LFP cathode enables one not only to follow the phase evolution on a single-particle level, but also to interpret the observations in terms of the significance of ionic and electronic conductivities as well as elastic effects,

leading to an overall understanding of the materials behaviour.

An initial solubility of FP in LFP of about 10 % is observed within the whole single crystalline cathode before phase separation occurs, being in line with reported solubility limits. The starting point of phase transformation is found to be determined by the ionic and electronic conductivities in LFP, reflecting the defect chemical situation. Meanwhile, the filament-like growth pattern of FP in LFP, as well as the homogeneous receding of the FP phase upon lithiation, is found to be dominated by elastic effects instead of being transport-controlled. This conclusion is of universal character and widely independent of the defect-chemical details of the LFP cathode. Furthermore, these investigations disclose the importance of elastic interactions on the (de)lithiation mechanism not only for the studied micro-sized battery, but also for full battery electrode materials. From the filament-like pattern observed, a particle size of not much more than around 200 nm seems suitable to avoid microcracking and possible associated loss in capacity and decrease in rate performance. Finally, the presented experimental approach is also very well suited for studying the phase formation mechanisms in other single and multi-particle battery materials in detail.

Abbreviations

AEY	Auger Electron Yield
APD	Avalanche Photo-Detector
BESSY	Berlin Electron Storage Ring Society for Synchrotron Radiation
CV	Cyclic Voltammetry
DMC	Dimethyl Carbonate
DOS	Density of States
EC	Ethylene Carbonate
EELS	Electron Energy Loss Spectroscopy
ELNES	Energy Loss Near Edge Structure
EMF	Electromotive Force
EXAFS	Extended X-ray Absorption Fine Structure
EXELFS	Extended Energy Loss Fine Structure
FIB	Focused Ion Beam
FOV	Field Of View
FP	Iron(III) Phosphate, $FePO_4$
FY	Fluorescence Yield
GFIS	Gas Field Ion Sources
GIXRD	Grazing Incidence X-ray Diffraction
HRTEM	High Resolution Transmission Electron Microscopy
ICP-OES	Inductively Coupled Plasma - Optical Emission Spectrometry
IBID-Pt	Ion Beam Induced Deposition of Platinum (IBID-Pt)
ISISS	Innovative Station for *In Situ* Spectroscopy
LCO	Lithium Cobalt Oxide, $LiCoO_2$

LFP	Lithium Iron Phosphate, $LiFePO_4$
LIB	Lithium Ion Battery
LiPON	Nitrogen doped Lithium Phosphate
LMIS	Liquid Metal Ion Source
LVSO	Lithium Vanadium Silicon Oxide, Li_2O-V_2O_5-SiO_2 (here: $Li_{3.5}V_{0.5}Si_{0.5}O_4$)
MBE	Molecular Beam Epitaxy
NEXAFS	Near Edge X-ray Absorption Fine Structure
NMP	N-Methylpyrrolidone
OCV	Open Circuit Voltage
PGM	Plane-Grating Monochromator
PLD	Pulsed Laser Deposition
PVDF	Polyvinylidene Difluoride
SEI	Solid Electrolyte Interphase
SEM	Scanning Electron Microscopy
SIMS	Secondary Ion Mass Spectrometry
STO	Strontium Titanate, $SrTiO_3$
STXM	Scanning Transmission X-ray Microscopy
TEM	Transmission Electron Microscopy
TEY	Total Electron Yield
THF	Tetrahydrofuran
ToF-SIMS	Time-of-flight Secondary Ion Mass Spectrometry
TXM	Transmission X-ray Microscope
UHV	Ultra High Vacuum
XANES	X-ray Absorption Near Edge Structure
XAS	X-ray Absorption Spectroscopy
XPS	X-ray Photoelectron Spectroscopy
XRD	X-ray Diffraction

List of Figures

References

[1] A. Volta, "On the electricity excited by the mere contact of conducting substances of different kinds," *Philosophical Transactions of the Royal Society of London*, pp. 403–431, MDCCC.

[2] M. Planté, "Note sur la polarisation voltaique," *Comptes rendus hebdomadaires des séances de l'Académie des sciences*, vol. 7, pp. 402–405, 1859.

[3] M. Whittingham, "Electrical Energy Storage and Intercalation Chemistry," *Science*, vol. 192, no. 4244, pp. 1126–1127, 1976.

[4] J.B. Goodenough, K. Mizushima, and P.J. Wiseman, "European Patent - EP17400B1," 1979.

[5] K. Mizushima, P.C. Jones, P.J. Wiseman, and J.B. Goodenough, "Li_xCoO_2 (0<x<1): A new cathode material for batteries of high energy density," *Materials Research Bulletin*, vol. 15, pp. 783–789, 1980.

[6] R. Yazami, and Ph. Touzain, "A reversible graphite-lithium negative electrode for electrochemical generators," *Journal of Power Sources*, vol. 9, no. 3, pp. 365–371, 1983.

[7] D. Aurbach, E. Zinigrad, Y. Cohen, and H. Teller, "A short review of failure mechanisms of lithium metal and lithiated graphite anodes in liquid electrolyte solutions," *Solid State Ionics*, vol. 148, no. 3-4, pp. 405–416, 2002.

[8] J.-M. Tarascon, and M. Armand, "Issues and challenges facing rechargeable lithium batteries," *Nature*, vol. 414, pp. 359–367, 2001.

[9] B. Dunn, H. Kamath, and J.-M. Tarascon, "Electrical Energy Storage for the Grid: A Battery of Choices," *Science*, vol. 334, no. 6058, pp. 928–935, 2011.

[10] X. Liu, Y. Zhang, D. Ge, J. Zhao, Y. Li, and F. Endres, "Three-dimensionally ordered macroporous silicon films made by electrodeposition from an ionic liquid," *Physical Chemistry Chemical Physics*, vol. 14, pp. 5100–5105, 2012.

[11] Y.-G. Guo, Y.-S. Hu, W. Sigle, and J. Maier, "Superior Electrode Performance of Nanostructured Mesoporous TiO_2 (Anatase) through Efficient Hierarchical Mixed Conducting Networks," *Advanced Materials*, vol. 19, no. 16, pp. 2087–2091, 2007.

[12] C. Zhu, X. Mu, P.A. van Aken, Y. Yu, and J. Maier, "Single-Layered Ultrasmall Nanoplates of MoS_2 Embedded in Carbon Nanofibers with Excellent Electrochemical Performance for Lithium and Sodium Storage," *Angewandte Chemie International Edition*, vol. 53, no. 8, pp. 2152–2156, 2014.

[13] N. Meethong, H.Y.S. Huang, W.C. Carter, and Y.-M. Chiang, "Size-Dependent Lithium Miscibility Gap in Nanoscale $Li_{1-x}FePO_4$," *Electrochemical and Solid-State Letters*, vol. 10, no. 5, pp. A134–A138, 2007.

[14] J. Wu, G.K.P. Dathar, C. Sun, M. G Theivanayagam, D. Applestone, A.G. Dylla, A. Manthiram, G. Henkelman, J.B. Goodenough, and K.J. Stevenson, "In situ Raman spectroscopy of $LiFePO_4$: size and morphology dependence during charge and self-discharge," *Nanotechnology*, vol. 24, no. 42, p. 424009, 2013.

[15] R. Malik, D. Burch, M. Bazant, and G. Ceder, "Particle Size Dependence of the Ionic Diffusivity," *Nano Letters*, vol. 10, no. 10, pp. 4123–4127, 2010.

[16] X. Li, and X.A. Sun, "Nitrogen-doped carbons in Li-S batteries: materials design and electrochemical mechanism," *Frontiers in Energy Research*, vol. 2, no. 49, 2014.

[17] J. Maier and R. Amin, "Defect Chemistry of $LiFePO_4$," *Journal of The Electrochemical Society*, vol. 155, no. 4, pp. A339–A344, 2008.

[18] J.-Y. Shin, D. Samuelis, and J. Maier, "Defect chemistry of lithium storage in TiO_2 as a function of oxygen stoichiometry," *Solid State Ionics*, vol. 225, no. 0, pp. 590–593, 2012. Solid State Ionics 18 Proceedings of the 18th International Conference on Solid State Ionics Warsaw, Poland, July 3 -8, 2011.

[19] N.A. Kaskhedikar, and J. Maier, "Lithium Storage in Carbon Nanostructures," *Advanced Materials*, vol. 21, pp. 2664–2680, 2009.

[20] E. Ferg, R.J. Gummow, A. de Kock, and M.M. Thackeray, "Spinel Anodes for Lithium Ion Batteries," *Journal of The Electrochemical Society*, vol. 141, no. 11, pp. L147–L150, 1994.

[21] J. Wolfenstine, J.L. Allen, J. Read, and D. Foster, "Chemistry and Structure of Sony's Nexelion Li-ion Electrode Materials," Tech. Rep. ARL-TN-0257, Army Research Laboratory, 2006.

[22] N. Yabuuchi and T. Ohzuku, "Novel lithium insertion material of $LiCo_{1/3}Ni_{1/3}Mn_{1/3}O_2$ for advanced lithium-ion batteries," *Journal of Power Sources*, vol. 119-121, no. 0, pp. 171–174, 2003. Selected papers presented at the 11th International Meeting on Lithium Batteries.

[23] M.M. Thackeray, W.I.F. David, P.G. Bruce, and J.B. Goodenough, "Lithium insertion into manganese spinels," *Materials Research Bulletin*, vol. 18, no. 4, pp. 461–472, 1983.

[24] A.K. Padhi, K.S. Nanjundaswamy, and J.B. Goodenough, "Phospho-olivines as Positive-Electrode Materials for Rechargeable Lithium Batteries," *The Journal of the Electrochemical Society*, vol. 144, no. 4, pp. 1188–1194, 1997.

[25] B. Scrosati and J. Garche, "Lithium batteries: Status, prospects and future," *Journal of Power Sources*, vol. 195, no. 9, pp. 2419–2430, 2010.

[26] S. Zhang, "A review on electrolyte additives for lithium-ion batteries," *Journal of Power Sources*, vol. 162, no. 2, pp. 1379–1394, 2006. Special issue including selected papers from the International Power Sources Symposium 2005 together with regular papers.

[27] A.J. Bhattacharyya, M. Dollé, and J. Maier, "Improved Li-Battery Electrolytes by Heterogeneous Doping of Nonaqueous Li-Salt Solutions," *Electrochemical and Solid-State Letters*, vol. 7, no. 11, pp. A432–A434, 2004.

[28] G. Jo, H. Jeon, and M.J. Park, "Synthesis of Polymer Electrolytes Based on Poly(ethylene oxide) and an Anion-Stabilizing Hard Polymer for Enhancing Conductivity and Cation Transport," *ACS Macro Letters*, vol. 4, no. 2, pp. 225–230, 2015.

[29] G.H. Lane, P.M. Bayley, B.R. Clare, A.S. Best, D.R. MacFarlane, M. Forsyth, and A.F. Hollenkamp, "Ionic Liquid Electrolyte for Lithium Metal Batteries: Physical, Electrochemical, and Interfacial Studies of N-Methyl-N-butylmorpholinium Bis(fluorosulfonyl)imide," *The Journal of Physical Chemistry C*, vol. 114, no. 49, pp. 21775–21785, 2010.

[30] P. Arora and Z.J. Zhang, "Battery Separators," *Chemical Reviews*, vol. 104, no. 10, pp. 4419–4462, 2004. PMID: 15669158.

[31] C.M. Julien, A. Mauger, K. Zaghib, and H. Groult, "Comparative Issues of Cathode Materials for Li-Ion Batteries," *Inorganics*, vol. 21, pp. 132–154, 2014.

[32] M. Whittingham, "Lithium Batteries and Cathode Materials," *Chemical Reviews*, vol. 104, no. 10, pp. 4271–4302, 2004. PMID: 15669156.

[33] S. Goriparti, E. Miele, F. De Angelis, E. Di Fabrizio, R. Proietti Zaccaria, and C. Capiglia, "Review on recent progress of nanostructured anode materials for Li-ion batteries," *Journal of Power Sources*, vol. 257, no. 0, pp. 421–443, 2014.

[34] K. Xu, "Nonaqueous Liquid Electrolytes for Lithium-Based Rechargeable Batteries," *Chemical Reviews*, vol. 104, no. 10, pp. 4303–4418, 2004. PMID: 15669157.

[35] J. Maier, "Size effects on mass transport and storage in lithium batteries," *Journal of Power Sources*, vol. 174, no. 2, pp. 569–574, 2007. 13th International Meeting on Lithium Batteries.

[36] M. Whittingham, "The role of ternary phases in cathode reactions," *Journal of The Electrochemical Society*, vol. 123, no. 3, pp. 315–320, 1976.

[37] J. Maier, "Mass storage in space charge regions of nano-sized systems (Nano-ionics. Part V)," *Faraday Discuss.*, vol. 134, pp. 51–66, 2007.

[38] J. Maier, "Nanoionics: ionic charge carriers in small systems," *Physical Chemistry Chemical Physics*, vol. 11, pp. 3011–3022, 2009.

[39] L. Fu, C.-C. Chen, D. Samuelis, and J. Maier, "Thermodynamics of Lithium Storage at Abrupt Junctions: Modeling and Experimental Evidence," *Physical Review Letteers*, vol. 112, p. 208301, May 2014.

[40] A. Kumar, R. Thomas, N.K. Karan, J.J. Saavedra-Arias, M.K. Singh, S.B. Majumder, M.S. Tomar, and R.S. Katiyar, "Structural and Electrochemical Characterization of Pure $LiFePO_4$ and Nanocomposite $C-LiFePO_4$ Cathodes for Lithium Ion Rechargeable Batteries," *Journal of Nanotechnology*, no. 176517, 2009.

[41] P. G. Bruce, B. Scrosati, and J.-M. Tarascon, "Nanomaterials for Rechargeable Lithium Batteries," *Angewandte Chemie International Edition*, vol. 47, no. 16, pp. 2930–2946, 2008.

[42] A.K. Padhi, K.S. Nanjundaswamy, C. Masquelier, S. Okada, and J.B. Goodenough, "Effect of Structure on the Fe^{3+}/Fe^{2+} Reclox Couple in Iron Phosphates," *The Journal of the Electrochemical Society*, vol. 144, no. 5, pp. 1609–1613, 1997.

[43] D. Jugovic, N. Cvjeticanin, M. Mitric, and S. Mentus, "Comparison between Different $LiFePO_4$ Synthesis Routes," *Materials Science Forum*, vol. 555, pp. 225–230, Sep 2007.

[44] K.-F. Chiu, H.-Y Tang, and B.-S. Lin, "High Conductivity $LiFePO_4$ / C Composite Thin Films with Ti Underlayers Deposited by Radio Frequency Sputtering," *Journal of The Electrochemical Society*, vol. 154, no. 4, pp. A364–A368, 2007.

[45] S.-X. Zhao, H. Ding, Y.-C. Wang, B.-H. Li, and C.-W. Nan, "Improving rate performance of $LiFePO_4$ cathode materials by hybrid coating of nano-Li_3PO_4 and carbon," *Journal of Alloys and Compounds*, vol. 566, no. 0, pp. 206–211, 2013.

[46] C. Zhu, Y. Yu, L. Gu, K. Weichert, and J. Maier, "Electrospinning of Highly Electroactive Carbon-Coated Single-Crystalline LiFePO$_4$ Nanowires," *Angewandte Chemie*, vol. 123, no. 28, pp. 6402–6406, 2011.

[47] K. Tang, X. Yu, J. Sun, H. Li, and X. Huang, "Kinetic analysis on LiFePO4 thin films by CV, GITT, and EIS," *Electrochimica Acta*, vol. 56, no. 13, pp. 4869–4875, 2011.

[48] D. Samuelis and J. Maier, *Chemical Energy Storage - Batteries: Concepts and Systems*. Berlin: De Gruyter, 2013.

[49] T. Maxisch and G. Ceder, "Elastic properties of olivine Li$_x$FePO$_4$ from first principles," *Physical Review B*, vol. 73, p. 174112, May 2006.

[50] B.L. Ellis, K.T. Lee, and L.F. Nazar, "Positive Electrode Materials for Li-Ion and Li-Batteries," *Chemistry of Materials*, vol. 22, no. 3, pp. 691–714, 2010.

[51] A.S Andersson, B. Kalska, L. Häggström, and J.O. Thomas, "Lithium extraction/insertion in LiFePO$_4$: an X-ray diffraction and Mössbauer spectroscopy study," *Solid State Ionics*, vol. 130, pp. 41–52, 2000.

[52] M. Gaberscek, J. Jamnik, K. Weichert, D. Samuelis, and J. Maier, *Nano Materials for Lithium-Ion Batteries – Fundamentals and Applications*. Pan Stanford Series on Nanotechnology and Nanoscience, Pan Stanford Publishing Pte. Ltd., 2013.

[53] R. Amin, J. Maier, P. Balaya, D.P. Chen, and C.T. Lin, "Ionic and electronic transport in single crystalline LiFePO$_4$ grown by optical floating zone technique," *Solid State Ionics*, vol. 179, pp. 1683–1687, 2008.

[54] C. Zhu, K. Weichert, and J. Maier, "Electronic Conductivity and Defect Chemistry of Heterosite FePO$_4$," *Advanced Functional Materials*, vol. 21, no. 10, pp. 1917–1921, 2011.

[55] R. Amin, P. Balaya, and J. Maier, "Anisotropy of Electronic and Ionic Transport in LiFePO$_4$ Single Crystals," *Electrochemical and Solid-State Letters*, vol. 10, 2007.

[56] M.S Islam, D.J. Driscoll, C.A.J. Fisher, P.R. Slater, "Atomic-Scale Investigation of Defects, Dopants, and Lithium Transport in the $LiFePO_4$ Olivine-Type Battery Material," *Chemistry of Materials*, vol. 17, no. 20, pp. 5085–5092, 2005.

[57] R. Amin, C. Lin, and J. Maier, "Aluminium-doped $LiFePO_4$ single crystals Part II. Ionic conductivity diffusivity and defect model," *Physical Chemistry Chemical Physics*, vol. 10, pp. 3524–3529, 2008.

[58] R Amin, C. Lin, and J. Maier, "Aluminium-doped $LiFePO_4$ single crystals Part I. Growth characterization and total conductivity," *Physical Chemistry Chemical Physics*, vol. 10, pp. 3519–3523, 2008.

[59] R. Amin, C. Lin, J. Peng, K. Weichert, T. Acartürk, U. Starke, and J. Maier, "Silicon-Doped $LiFePO_4$ Single Crystals: Growth, Conductivity Behavior, and Diffusivity," *Advanced Functional Materials*, vol. 19, no. 11, pp. 1697–1704, 2009.

[60] D. Morgan, A. Van Der Ven, G. Ceder, "Li conductivity in Li_xMPO_4 (M = Mn, Fe, Co, Ni) olivine materials," *Electrochemical and Solid-State Letters*, vol. 7, no. 2, pp. A30–A32, 2004.

[61] S.-I Nishimura, G. Kobayashi, K. Ohoyama, R. Kanno, M. Yashima, and A. Yamada, "Experimental visualization of lithium diffusion in Li_xFePO_4," *Nature Materials*, vol. 7, pp. 707–711, SEP 2008.

[62] D.P. Chen, A. Maljuk, and C.T. Lin, "Floating zone growth of lithium iron (II) phosphate single crystals," *Journal of Crystal Growth*, vol. 284, no. 1-2, pp. 86–90, 2005.

[63] A.V. Churikov, A.V. Ivanishchev, I.A. Ivanishcheva, V.O. Sycheva, N.R. Khasanova, and E.V. Antipov, "Determination of lithium diffusion coefficient in $LiFePO_4$ electrode by galvanostatic and potentiostatic intermittent titration techniques," *Electrochimica Acta*, vol. 55, no. 8, pp. 2939–2950, 2010.

[64] J. Come, P.L. Taberna, S. Hamelet, C. Masquelier, and P. Simon, "Electrochemical Kinetic Study of $LiFePO_4$ Using Cavity Microelectrode," *Journal of The Electrochemical Society*, vol. 158, no. 10, pp. A1090–A1093, 2011.

[65] X.-C. Tang, L.-X. Li, Q.-L. Lai, X.-W. Song, and L.-H. Jiang, "Investigation on diffusion behavior of Li^+ in $LiFePO_4$ by capacity intermittent titration technique (CITT)," *Electrochimica Acta*, vol. 54, no. 8, pp. 2329–2334, 2009.

[66] L.-X. Yuan, Z.-H. Wang, W.-X. Zhang, X.-L. Hu, J.-T. Chen, Y.H. Huang, and J.B. Goodenough, "Development and challenges of $LiFePO_4$ cathode material for lithium-ion batteries," *Energy & Environmental Science*, vol. 4, pp. 269–284, 2011.

[67] A.S. Andersson, J.O. Thomas, B. Kalska, and L. Häggström, "Thermal Stability of $LiFePO_4$ - based Cathodes," *Electrochemical and Solid-State Letters*, vol. 3, no. 2, pp. 66–68, 2000.

[68] K. Weichert, W. Sigle, P.A. van Aken, J. Jamnik, C. Zhu, R. Amin, T. Acartürk, U. Starke, and J. Maier, "Phase Boundary Propagation in Large $LiFePO_4$ Single Crystals on Delithiation," *Journal of the American Chemical Society*, vol. 134, no. 6, pp. 2988–2992, 2012.

[69] S. Okada, S. Sawa, M. Egashira, J.-I. Yamaki, M. Tabuchi, H. Kageyama, T. Konishi, and A. Yoshino, "Cathode properties of phospho-olivine $LiMPO_4$ for lithium secondary batteries," *Journal of Power Sources*, vol. 97-98, no. 0, pp. 430–432, 2001. Proceedings of the 10th International Meeting on Lithium Batteries.

[70] M. Park, X. Zhang, M. Chung, G.B. Less, and A.M. Sastry, "A review of conduction phenomena in Li-ion batteries," *Journal of Power Sources*, vol. 195, no. 24, pp. 7904–7929, 2010.

[71] N. Ravet, J.B. Goodenough, S. Besner, M. Simoneau, P. Hovington, and M. Armand vol. 99-2, (Honolulu, Hi), ECS Meeting, October 1999.

[72] J. Wang and X. Sun, "Understanding and recent development of carbon coating on $LiFePO_4$ cathode materials for lithium-ion batteries," *Energy & Environmental Science*, vol. 5, pp. 5163–5185, 2012.

[73] Y. Wang, Y. Wang, E. Hosono, K. Wang, and H. Zhou., "The Design of a $LiFePO_4$/Carbon Nanocomposite With a Core-Shell Structure and Its Synthesis

by an In Situ Polymerization Restriction Method," *Angewandte Chemie International Edition*, vol. 47, no. 39, pp. 7461–7465, 2008.

[74] Y.-S. Hu, Y.-G. Guo, R. Dominko, M. Gaberscek, J. Jamnik, and J. Maier, "Improved Electrode Performance of Porous LiFePO$_4$ Using RuO$_2$ as an Oxidic Nanoscale Interconnect," *Advanced Materials*, vol. 19, pp. 1963–1966, 2007.

[75] H. Zhou, D. Li, M. Hibino, and I. Honma, "A Self-Ordered, Crystalline–Glass, Mesoporous Nanocomposite for Use as a Lithium-Based Storage Device with Both High Power and High Energy Densities," *Angewandte Chemie International Edition*, vol. 44, no. 5, pp. 797–802, 2005.

[76] B. Kang and G. Ceder, "Battery materials for ultrafast charging and discharging," *Nature*, vol. 458, pp. 190–193, 2009.

[77] S.-Y. Chung, J.T. Bloking, and Y.-M. Chiang, "Electronically conductive phospho-olivines as lithium storage electrodes," *Nature Materials*, vol. 1, pp. 123–128, 2002.

[78] N. Ravet, A. Abouimrane, and M. Armand, "From our readers: On the electronic conductivity of phospho-olivines as lithium storage electrodes," *Nature Materials*, vol. 2, no. 11, p. 702, 2003.

[79] P.S. Herle, B. Ellis, N. Coombs, and L.F. Nazar, "Nano-network electronic conduction in iron and nickel olivine phosphates," *Nature Materials*, vol. 3, no. 3, pp. 147–152, 2003.

[80] G. Chen, X. Song, and T.J. Richardson, "Electron Microscopy Study of the LiFePO$_4$ to FePO$_4$ Phase Transition," *Electrochemical and Solid-State Letters*, vol. 9, no. 6, pp. A295–A298, 2006.

[81] L. Laffont, C. Delacourt, P. Gibot, M.Y. Wu, P. Kooyman, C. Masquelier, and J.M. Tarascon, "Study of the LiFePO$_4$/FePO$_4$ Two-Phase System by High-Resolution Electron Energy Loss Spectroscopy," *Chemistry of Materials*, vol. 18, no. 23, pp. 5520–5529, 2006.

[82] C. Delmas, M. Maccario, L. Croguennec, F. Le Cras, and F. Weill, "Lithium deintercalation in LiFePO$_4$ nanoparticles via a domino-cascade model," *Nature Materials*, vol. 7, pp. 665–671, 2008.

[83] V. Srinivasan, J. Newman, "Existence of Path-Dependence in the LiFePO$_4$ Electrode," *Electrochemical and Solid-State Letters*, vol. 9, no. 3, pp. A110–A114, 2006.

[84] J.L. Allen, T.R. Jow, J. Wolfenstine, "Analysis of the FePO$_4$ to LiFePO$_4$ phase transition," *Journal of Solid State Electrochemistry*, vol. 12, no. 7-8, pp. 1031–1033, 2008.

[85] R. Malik, F. Zhou, and G. Ceder, "Kinetics of non-equilibrium lithium incorporation in LiFePO$_4$," *Nature Materials*, vol. 10, pp. 587–590, 2011.

[86] M. Wagemaker, D.P. Singh, W.J.H. Borghols, U. Lafont, L. Haverkate, V.K. Peterson, and F.M. Mulder, "Dynamic Solubility Limits in Nanosized Olivine LiFePO$_4$," *Journal of the American Chemical Society*, vol. 133, no. 26, pp. 10222–10228, 2011.

[87] J.L. Dodd, R. Yazami, and B. Fultz, "Phase Diagram of Li$_x$FePO$_4$," *Electrochemical and Solid-State Letters*, vol. 9, no. 3, pp. A151–A155, 2006.

[88] R. Malik, A. Abdellahi, G. Ceder, "A Critical Review of the Li Insertion Mechanisms in LiFePO$_4$ Electrodes," *Journal of The Electrochemical Society*, vol. 160, no. 5, pp. A3179–A3197, 2013.

[89] V. Srinivasan and J. Newman, "Discharge Model for the Lithium Iron-Phosphate Electrode," *Journal of The Electrochemical Society*, vol. 151, no. 10, pp. A1517–A1529, 2004.

[90] A. Yamada, H. Koizumi, N. Sonoyama, R. Kanno, "Phase Change in Li$_x$FePO$_4$," *Electrochemical and Solid-State Letters*, vol. 8, no. 8, pp. A409–A413, 2005.

[91] A. Yamada, H. Koizumi, S. Nishimura, N. Sonoyama, R. Kanno, M. Yonemura, T. Nakamura, and Y. Kobayashi, "Room-temperature miscibility gap in Li$_x$FePO$_4$," *Nature Materials*, vol. 5, pp. 357–360, 2006.

[92] N. Meethong, Y.-H. Kao, M. Tang, H.-Y. Huang, W.C. Carter, and Y.-M. Chiang, "Electrochemically Induced Phase Transformation in Nanoscale Olivines $Li_{1-x}MPO_4$ (M = Fe, Mn)," *Chemistry of Materials*, vol. 20, no. 19, pp. 6189–6198, 2008.

[93] J. Wang, Y.-C.K. Chen-Wiegart, and J. Wang, "In operando tracking phase transformation evolution of lithium iron phosphate with hard X-ray microscopy," *Nature Communications*, vol. 5, no. 4570, 2014.

[94] C.V. Ramana, A. Mauger, F. Gendron, C.M. Julien, and K. Zaghib, "Study of the Li-insertion/extraction process in $LiFePO_4/FePO_4$," *Journal of Power Sources*, vol. 187, no. 2, pp. 555–564, 2009.

[95] L Gu,C. Zhu, H. Li, Y. Yu, C.Li, S.Tsukimoto, J. Maier, Y. Ikuhara, "Direct Observation of Lithium Staging in Partially Delithiated $LiFePO_4$ at Atomic Resolution," *Journal of the American Chemical Society*, vol. 133, no. 13, pp. 4661–4663, 2011.

[96] Y. Orikasa,T. Maeda, Y. Koyama, H. Murayama, K. Fukuda, H. Tanida, H. Arai, E. Matsubara, Y. Uchimoto, Z. Ogumi, "Direct Observation of a Metastable Crystal Phase of Li_xFePO_4 under Electrochemical Phase Transition," *Journal of the American Chemical Society*, vol. 135, no. 15, pp. 5497–5500, 2013.

[97] C. Zhu, L. Gu, L. Suo, J. Popovic, H. Li, Y. Ikuhara, and J. Maier., "Size-Dependent Staging and Phase Transition in $LiFePO_4/FePO_4$," *Advanced Functional Materials*, vol. 24, no. 3, pp. 312–318, 2014.

[98] W.C. Chueh, F. El Gabaly, J.D. Sugar, N.C. Bartelt, A.H. McDaniel, K.R. Fenton, K.R. Zavadil, T. Tyliszczak, W. Lai, K.F. McCarty, "Intercalation Pathway in Many-Particle $LiFePO_4$ Electrode Revealed by Nanoscale State-of-Charge Mapping," *Nano Letters*, vol. 13, no. 3, pp. 866–872, 2013.

[99] W. Dreyer, J. Jamnik, C. Guhlke,R. Huth, J. Moskon, and M. Gaberscek, "The thermodynamic origin of hysteresis in insertion batteries," *Nature Materials*, vol. 9, pp. 448–453, 2010.

[100] Y. Li, F.E. Gabaly, T.R. Ferguson, R.B. Smith, N.C. Bartelt, J.D. Sugar, K.R. Fenton, D.A. Cogswell, A.L.D. Kilcoyne, T. Tyliszczak, M.Z. Bazant, and W.C. Chueh, "Current-induced transition from particle-by-particle to concurrent intercalation in phase-separating battery electrodes," *Nature Materials*, vol. 13, pp. 1149–1156, 2014.

[101] L. Spiess, G. Teichert, R. Schwarzer, H. Behnken, and C. Genzel, *Moderne Röntgenbeugung: Röntgendiffraktometrie für Materialwissenschaftler, Physiker und Chemiker*. Vieweg+Teubner, 2. ed., 2009.

[102] J.R. Ferraro, K. Nakamoto, and C.W. Brown, *Introductory Raman Spectroscopy*. Academic Press, 2. ed., 2002.

[103] D.B. Williams and C.B. Carter, *Transmission Electron Microscopy: Basics I*. Plenum Press, 1996.

[104] D.B. Williams and C.B. Carter, *Transmission Electron Microscopy: Diffraction II*. Plenum Press, 1996.

[105] D.B. Williams and C.B. Carter, *Transmission Electron Microscopy: Imaging III*. Springer, 1996.

[106] D.B. Williams and C.B. Carter, *Transmission Electron Microscopy: Spectrometry IV*. Plenum Press, 1996.

[107] J.C. Vickerman, A.A. Brown, and N.M. Reed, *Secondary ion mass spectrometry: principles and applications*. International Series of Monographs on Chemistry Series, Clarendon Press, 1989.

[108] J. Nolte, *ICP Emissionsspektrometrie für Praktiker: Grundlagen, Methodenentwicklung, Anwendungsbeispiele*. Wiley-VCH, 1. ed., 2003.

[109] M.A. Herman and H. Sitter, *Molecular Beam Epitaxy*, vol. 7 of *Springer Series in Materials Science 7*. Springer, 2. ed., 1996.

[110] J. Mahan, *Physical Vapor Deposition of Thin Films*. Wiley & Sons, 1. ed., 2000.

[111] J. Heinze, "Cyclovoltammetrie — die "Spektroskopie" des Elektrochemikers," *Angewandte Chemie*, vol. 96, no. 11, pp. 823–840, 1984.

[112] D. Mattox, *Handbook of physical vapor deposition (PVD) processing.* Elsevier, 2. ed., 2010.

[113] D.B. Chrisey and G.K. Hubler, *Pulsed Laser Deposition of Thin Films.* A Wiley interscience publication, Wiley, 1994.

[114] N. Kuwata, J. Kawamura, K. Toribami, T. Hattori, and N. Sata, "Thin-film lithium-ion battery with amorphous solid electrolyte fabricated by pulsed laser deposition," *Electrochemistry Communications*, vol. 6, no. 4, pp. 417–421, 2004.

[115] M. Morcrette, P. Barboux, A. Laurent, and J. Perrire, "Growth and characterization of nasicon thin films by the laser ablation method," *Solid State Ionics*, vol. 93, pp. 283–290, 1997.

[116] O. Guillot Noël, R. Gomez San Roman, J. Perrière, J. Hermann, V. Craciun, L. Boulmer Leborgne, and P. Barboux, "Growth of apatite films by laser ablation: Reduction of the droplet areal density," *Journal of Applied Physics*, vol. 80, no. 3, pp. 1803–1808, 1996.

[117] C. Kisielowski, B. Freitag, M. Bischoff, H. van Lin, S. Lazar, G. Knippels, P. Tiemeijer, M. van der Stam, S. von Harrach, M. Stekelenburg, M. Haider, S. Uhlemann, H. Müller, P. Hartel, B. Kabius, D. Miller, I. Petrov, E.A. Olson, T. Donchev, E.A. Kenik, A.R. Lupini, J. Bentley, S.J. Pennycook, I.M. Anderson, A.M. Minor, A.K. Schmid, T. Duden, V. Radmilovic, Q.M. Ramasse, M. Watanabe, R. Erni, E.A. Stach, P. Denes, and U. Dahmen, "Detection of Single Atoms and Buried Defects in Three Dimensions by Aberration-Corrected Electron Microscope with $0.5\mathring{A}$ Information Limit," *Microscopy and Microanalysis*, vol. 14, pp. 469–477, 10 2008.

[118] N. Ohmer, "Investigations on yttria-stabilized zirconia by SEM, AFM and Controlled Atmosphere High Temperature Scanning Probe Microscopy," diploma thesis, Carl von Ossietzky University of Oldenburg, Mai 2008.

[119] S.L. Flegler, J.W. Heckman, and K.L. Klomparens, *Elektronenmikroskopie: Grundlagen - Methoden - Anwendungen.* Spektrum Akademischer Verlag, 1995.

[120] W.H. Escovitz, T.R. Fox, R. Levi-Setti, "Scanning transmission ion microscope with a field ion source," *Proceedings of the National Academy of Sciences*, vol. 72, no. 5, pp. 1826–1828, 1975.

[121] A. Dixon, "The energy spread of metal ions drawn from their liquid," *Journal of Physics D: Applied Physics*, vol. 12, no. 6, p. L77, 1979.

[122] H.M. Wu, L.A. Stern, J.H. Chen, M. Huth, C.H. Schwalb, M. Winhold, F. Porrati, C.M. Gonzalez, R. Timilsina, and P.D. Rack, "Synthesis of nanowires via helium and neon focused ion beam induced deposition with the gas field ion microscope," *Nanotechnology*, vol. 24, no. 17, p. 175302, 2013.

[123] M.T. Postek and A.E. Vladár, "Helium ion microscopy and its application to nanotechnology and nanometrology," *Scanning*, vol. 30, no. 6, pp. 457–462, 2008.

[124] D. Winston, J. Ferrera, L. Battistella, A.E. Vladár, K.K. Berggren, "Modeling the Point-Spread Function in Helium-Ion Lithography," *Scanning*, vol. 34, no. 2, pp. 121–128, 2012.

[125] P.F.A. Alkemade, E.M. Koster, E. van Veldhoven, and D.J. Maas, "Imaging and Nanofabrication With the Helium Ion Microscope of the Van Leeuwenhoek Laboratory in Delft," *Scanning*, vol. 34, no. 2, pp. 90–100, 2012.

[126] P. Buseck, J. Cowley, and L. Eyring, *High-Resolution Transmission Electron Microscopy and Associated Techniques.* New York: Oxford University Press, 1989.

[127] R. F. Egerton, *Electron energy loss spectroscopy in the electron microscope.* New York: Springer, 3rd ed., 2011.

[128] A. Einstein, "Über einen die Erzeugung und Verwandlung des Lichtes betreffenden heuristischen Gesichtspunkt," *Annalen der Physik*, vol. 17, pp. 132–148, 1905.

[129] D. Meschede, *Gerthsen Physik.* Springer, 22 ed., 2004.

[130] D.E. Sayers, F.W. Lytle, and E.A. Stern, *Point Scattering Theory of X-ray Absorption Fine Structure, in Advances in X-Ray Analysis*, vol. 13. Plenum Press, 1970.

[131] E. Stern, "Theory of the extended x-ray-absorption fine structure," *Physical Review B*, vol. 10, pp. 3027–3037, Oct 1974.

[132] E.. Vass, M. Hävecker, S. Zafeiratos, D. Teschner, A. Knop-Gericke, and R. Schlögl, "The role of carbon species in heterogeneous catalytic processes: an in situ soft x-ray photoelectron spectroscopy study," *Journal of Physics: Condensed Matter*, vol. 20, no. 18, p. 184016, 2008.

[133] "www.helmholtz-berlin.de."

[134] R. Follath, J. S. Schmidt, M. Weigand, and K. Fauth, "The X-ray microscopy beamline UE46-PGM2 at BESSY," *AIP Conference Proceedings*, vol. 1234, p. 323, 2010.

[135] D. Nolle, M. Weigand, P. Audehm, E. Goering, U. Wiesemann, C. Wolter, E. Nolle, G. Schütz, "Note: Unique characterization possibilities in the ultra high vacuum scanning transmission x-ray microscope (UHV-STXM) "MAXYMUS" using a rotatable permanent magnetic field up to 0.22 T," *Review of Scientific Instruments*, vol. 83, no. 4, 2012.

[136] H. Rarback, D. Shu, S.C. Feng, H. Ade, C. Jacobsen, J. Kirz, I. McNulty, Y. Vladimirsky, D. Kern, P. Chang, "The Stony Brook/NSLS Scanning Microscope," in *X-Ray Microscopy II* (D. Sayre, J. Kirz, M. Howells, and H. Rarback, eds.), vol. 56 of *Springer Series in Optical Sciences*, pp. 194–200, Springer Berlin Heidelberg, 1988.

[137] J. Kirz, H. Ade, C. Jacobsen, C.-H. Ko, S. Lindaas, I. McNulty, D. Sayre, S. Williams, X. Zhang, M. Howells, "Soft X-ray microscopy with coherent X-rays," *Review of Scientific Instruments*, vol. 63, no. 1, pp. 557–563, 1992.

[138] J. Kirz and C. Jacobsen, "The history and future of X-ray microscopy," *Journal of Physics: Conference Series*, vol. 186, 2009.

[139] "www.lightsources.org."

[140] A.L.D. Kilcoyne, T. Tyliszczak, W.F. Steele, S. Fakra, P. Hitchcock, K. Franck, E. Anderson, B. Harteneck, E.G. Rightor, G.E. Mitchell, A.P. Hitchcock, L. Yang, T. Warwick, and H. Ade, "Interferometer-controlled scanning transmission X-ray microscopes at the Advanced Light Source," *Journal of Synchrotron Radiation*, vol. 10, pp. 125–136, Mar 2003.

[141] K.V. Kaznatcheev, Ch. Karunakaran, U.D. Lanke, S.G. Urquhart, M. Obst, and A.P. Hitchcock, "Soft X-ray spectromicroscopy beamline at the CLS: Commissioning results," *Nuclear Instruments and Methods in Physics Research Section A: Accelerators, Spectrometers, Detectors and Associated Equipment*, vol. 582, no. 1, pp. 96–99, 2007. Proceedings of the 14th National Conference on Synchrotron Radiation Research 2007.

[142] T. Ohigashi, H. Arai, T. Araki, N. Kondo, E. Shigemasa, A. Ito, N. Kosugi, and M. Katoh, "Construction of the Scanning Transmission X-ray Microscope Beamline at UVSOR," *Journal of Physics: Conference Series*, vol. 463, no. 1, p. 012006, 2013.

[143] M. Salomé, M. Cotte, R. Baker, R. Barrett, N. Benseny-Cases, G. Berruyer, D. Bugnazet, H. Castillo-Michel, C. Cornu, B. Fayard, E. Gagliardini, R. Hino, J. Morse, E. Papillon, E. Pouyet, C. Rivard, V.A. Solé, J. Susini, G. Veronesi, "The ID21 Scanning X-ray Microscope at ESRF," *Journal of Physics: Conference Series*, vol. 425, no. 18, p. 182004, 2013.

[144] J. Raabe, G. Tzvetkov, U. Flechsig, M. Böge, A. Jaggi, B. Sarafimov, M.G.C. Vernooij, T. Huthwelker, H. Ade, D. Kilcoyne, T. Tyliszczak, R.H. Fink, C. and Quitmann., "PolLux: A new facility for soft X-ray spectromicroscopy at the Swiss Light Source," *Review of Scientific Instruments*, vol. 79, no. 11, 2008.

[145] H.-J. Shin, Y. Chung, and B. Kim, "The first undulator beamline at the Pohang Light Source for high-resolution spectroscopy and spectromicroscopy," *Journal of*

Electron Spectroscopy and Related Phenomena, vol. 101-103, no. 0, pp. 985–989, 1999.

[146] C. Xue, Y. Wang, Z. Guo, Y. Wu, X. Zhen, M. Chen, J. Chen, S. Xue, Z. Peng, Q. Lu, R. Tai, "High-performance soft x-ray spectromicroscopy beamline at SSRF," *Review of Scientific Instruments*, vol. 81, no. 10, 2010.

[147] B. Kaulich, D. Bacescu, J. Susini, C. David, E. Di Fabrizio, G. R. Morrison, P. Charalambous, J. Thieme, T. Wilhein, J. Kovac, D. Cocco, M. Salome, O. Dhez, T. Weitkamp, S. Cabrini, D. Cojoc, A. Gianoncelli, U. Vogt, M. Podnar, M. Zangrando, M. Zacchigna and M. Kiskinova, "TwinMic - A European Twin X-ray Microscopy Station Commissioned at ELETTRA," *Proc. 8th Int. Conf. X-ray Microscopy*, vol. IPAP Conf. Series 7, pp. 22–25, 2006.

[148] "www.diamond.ac.uk."

[149] H. Motz, "Applications of the Radiation from Fast Electron Beams," *Journal of Applied Physics*, vol. 22, no. 5, pp. 527–535, 1951.

[150] R. Follath, F. Senf, W. Gudat, "Plane-grating monochromator at BESSY II using collimated light," *Journal of Synchrotron Radiation*, vol. 5, pp. 769–771, May 1998.

[151] W. Chao, J. Kim, S. Rekawa, P. Fischer, and E.H. Anderson, "Demonstration of 12 nm Resolution Fresnel Zone Plate Lens based Soft X-ray Microscopy," *Optics Express*, vol. 17, pp. 17669–17677, Sep 2009.

[152] W. Hoppe, "Beugung im inhomogenen Primärstrahlwellenfeld. I. Prinzip einer Phasenmessung von Elektronenbeungungsinterferenzen," *Acta Crystallographica Section A*, vol. 25, pp. 495–501, Jul 1969.

[153] M. Dierolf, A. Menzel, P. Thibault, P. Schneider, C.M. Kewish, R. Wepf, O. Bunk, and F. Pfeiffer, "Ptychographic X-ray computed tomography at the nanoscale," *Nature*, vol. 467, pp. 436–439, 2010.

[154] J.M. Rodenburg, and R.H.T. Bates., "The Theory of Super-Resolution Electron Microscopy Via Wigner-Distribution Deconvolution," *Philosophical Transactions*

of the Royal Society of London. Series A: Physical and Engineering Sciences, vol. 339, no. 1655, pp. 521–553, 1992.

[155] X.-J. Wang, C. Jaye, K.-W. Nam, B. Zhang, H.Y. Chen, J. Bai, H. Li, X. Huang, D.A. Fischer, X.-Q. Yang, "Investigation of the structural changes in $Li_{1-x}FePO_4$ upon charging by synchrotron radiation techniques," in *Journal of Materials Chemistry* [98], pp. 11406–11411.

[156] J. Niu, A. Kushima, X. Qian, L. Qi, K. Xiang, Y.-M. Chiang, and J. Li., "In Situ Observation of Random Solid Solution Zone in $LiFePO_4$ Electrode," *Nano Letters*, vol. 14, no. 7, pp. 4005–4010, 2014. PMID: 24823479.

[157] J. Hong, C. Wang, N.J. Dudney, M.J. Lance, "Characterization and Performance of $LiFePO_4$ Thin-Film Cathodes Prepared with Radio-Frequency Magnetron-Sputter Deposition," *Journal of The Electrochemical Society*, vol. 154, no. 8, pp. A805–A809, 2007.

[158] A. Augustsson, G.V. Zhuang, S.M. Butorin, L.M. Osorio-Guillen, C.L. Dong, R. Ahuja, C.L. Chang, P.N. Ross, J. Nordgren, J.-H. Guo, "Electronic structure of phospho-olivines Li_xFePO_4(x=0,1) from soft-x-ray-absorption and -emission spectroscopies," in *The Journal of Chemical Physics* [98], pp. 866–872.

[159] S. Yang, D. Wang, G. Liang, Y.M. Yiu, J. Wang, L. Liu, X. Sun, T.-K. Sham, "Soft X-ray XANES studies of various phases related to $LiFePO_4$ based cathode materials," in *Energy & Environmental Science* [98], pp. 7007–7016.

[160] "http://libgroup.net/."

[161] J. Popovic, R. Demir-Cakan, J. Tornow, M. Morcrette, D.S. Su, R. Schlögl, M. Antonietti, M.-M. Titirici, "$LiFePO_4$ Mesocrystals for Lithium-Ion Batteries," *Small*, vol. 7, no. 8, pp. 1127–1135, 2011.

[162] J. Randles, "A cathode ray polarograph. Part II.-The current-voltage curves," *Transactions of the Faraday Society*, vol. 44, pp. 327–338, 1948.

[163] A. Sevcik, "Oscillographic polarography with periodical triangular voltage," *Collection of Czechoslovak Chemical Communications*, vol. 13, pp. 349–377, 1948.

[164] K. Oldham, "Analytical expressions for the reversible Randles-Sevcik function," *Journal of Electroanalytical Chemistry and Interfacial Electrochemistry*, vol. 105, no. 2, pp. 373–375, 1979.

[165] R.S. Nicholson and I. Shain, "Theory of Stationary Electrode Polarography. Single Scan and Cyclic Methods Applied to Reversible, Irreversible, and Kinetic Systems.," *Analytical Chemistry*, vol. 36, no. 4, pp. 706–723, 1964.

[166] A. MacLeod, "A note on the Randles-Sevcik function from electrochemistry," *Applied Mathematics and Computation*, vol. 57, pp. 305–310, 1993.

[167] M.E. Schuster, D. Teschner, J. Popovic, N. Ohmer, F. Girgsdies, J. Tornow, M.G. Willinger, D. Samuelis, M.-M. Titirici, J. Maier, R. Schlögl, "Charging and Discharging Behavior of Solvothermal $LiFePO_4$ Cathode Material Investigated by Combined EELS/NEXAFS Study," *Chemistry of Materials*, vol. 26, no. 2, pp. 1040–1047, 2014.

[168] G. S. Team. Digital Micrograph, 2003.

[169] W. Sigle, R.I. Amin, K. Weichert, P.A. van Aken, and J. Maier, "Delithiation Study of $LiFePO_4$ Crystals Using Electron Energy-Loss Spectroscopy," *Electrochemical and Solid-State Letters*, vol. 12, no. 8, pp. A151–A154, 2009.

[170] N. Kuwata, R. Kumar, K. Toribami, T. Suzuki, T. Hattori, and J. Kawamura, "Thin film lithium ion batteries prepared only by pulsed laser deposition," *Solid State Ionics*, vol. 177, no. 26-32, pp. 2827–2832, 2006. Solid State Ionics 15: Proceedings of the 15th International Conference on Solid State Ionics, Part II.

[171] N. Kuwata, N. Iwagami, Y. Matsuda, Y. Tanji, J. Kawamura, "Thin Film Batteries with Li_3PO_4 Solid Electrolyte Fabricated by Pulsed Laser Deposition," *ECS Transactions*, vol. 16, no. 26, pp. 53–60, 2009.

[172] N. Kuwata, N. Iwagami, Y. Tanji, Y. Matsuda, J. Kawamura, "Characterization of Thin-Film Lithium Batteries with Stable Thin-Film Li_3PO_4 Solid Electrolytes Fabricated by ArF Excimer Laser Deposition," *Journal of The Electrochemical Society*, vol. 157, no. 4, pp. A521–A527, 2010.

[173] F. Sauvage, E. Baudrin, M. Morcrette, and J.M. Tarascon, "Pulsed Laser Deposition and Electrochemical Properties of LiFePO$_4$ Thin Films," *Electrochemical and Solid-State Letters*, vol. 7, no. 1, pp. A15–A18, 2004.

[174] H. Ohtsuka and J.-I. Yamaki, "Electrical characteristics of Li$_2$O-V$_2$O$_5$-SiO$_2$ thin films," *Solid State Ionics*, vol. 35, pp. 201–206, 1989.

[175] H. Ohtsuka and J.-I. Yamaki, "Preparation and Electrical Conductivity of Li$_2$O-V$_2$O$_5$-SiO$_2$ Thin Films," *Japanese Journal of Applied Physics*, vol. 28, no. 11R, p. 2264, 1989.

[176] V. Palomares, I.R. de Larramendi, J. Alonso, M. Bengoechea, A. Goni, O. Miguel, T. Rojo, "LiFePO$_4$ thin films grown by pulsed laser deposition: Effect of the substrate on the film structure and morphology," *Applied Surface Science*, vol. 256, pp. 2563–2568, FEB 1 2010.

[177] W. Umrath, R. Bahnen, T. Dreifert, H.-U. Haefner, R. Hölzer, F. Kadi, E. Mossolff, H. Litterscheid, R. Rey, H. Rottländer, W. Scheer, F. Schönborn, and G. Voß, *Grundlagen der Vakuumtechnik*. Oerlikon - Leybold Vacuum, 2009.

[178] K. Tang, J. Sun, X. Yu, H. Li, and X. Huang, "Electrochemical performance of LiFePO$_4$ thin films with different morphology and crystallinity," *Electrochimica Acta*, vol. 54, no. 26, pp. 6565–6569, 2009.

[179] J. Kawamura, N. Kuwata, K. Toribami, N. Sata, O. Kamishima, and T. Hattori, "Preparation of amorphous lithium ion conductor thin films by pulsed laser deposition," *Solid State Ionics*, vol. 175, pp. 273–276, 2004. Fourteenth International Conference on Solid State Ionics.

[180] S. Zhao and Q. Qin, "LVSO thin film electrolyte for all-solid-state Li-ion battery," *Journal of Power Sources*, vol. 122, no. 2, pp. 174–180, 2003.

[181] J.F. Smith and Z. Moser, "Thermodynamic properties of binary lithium systems - A review," *Journal of Nuclear Materials*, vol. 59, no. 2, pp. 158–174, 1976.

[182] B. Hallstedt and O. Kim, "Thermodynamic assessment of the Al-Li system," *International Journal of Materials Research*, vol. 98, no. 10, pp. 961–969, 2007.

[183] H.J. Bang, S. Kim, and J. Prakash, "Electrochemical investigations of lithium-aluminum alloy anode in Li/polymer cells," *Journal of Power Sources*, vol. 92, pp. 45–49, 2001.

[184] K.-F. Chiu, "Optimization of Synthesis Process for Carbon-Mixed LiFePO$_4$ Composite Thin-Film Cathodes Deposited by Bias Sputtering," *Journal of The Electrochemical Society*, vol. 154, no. 2, pp. A129–A133, 2007.

[185] W. Paraguassu, P. T. C. Freire, V. Lemos, S. M. Lala, L. A. Montoro and J. M. Rosolen, "Phonon calculation on olivine-like LiMPO$_4$ (M = Ni, Co, Fe) and Raman scattering of the iron-containing compound," *Journal of Raman Spectroscopy*, vol. 36, pp. 213–220, 2005.

[186] C. Z. M. GmbH, "Product Information: ZEISS Crossbeam 340 and Crossbeam 540," 08 2013.

[187] C. Z. M. GmbH, "Product Information: MERLIN Series," 07 2012.

[188] J. Xie, N. Imanishi, T. Zhang, A. Hirano, Y. Takeda, and O. Yamamoto, "Li-ion diffusion kinetics in LiFePO$_4$ thin film prepared by radio frequency magnetron sputtering," *Electrochimica Acta*, vol. 54, no. 20, pp. 4631–4637, 2009.

[189] J. Shirakawa, M. Nakayama, M. Wakihara, and Y. Uchimoto, "Changes in Electronic Structure upon Li Insertion Reaction of Monoclinic Li$_3$Fe$_2$(PO$_4$)$_3$," *The Journal of Physical Chemistry B*, vol. 110, no. 36, pp. 17743–17750, 2006. PMID: 16956257.

[190] C. Delacourt, P. Poizot, J.-M. Tarascon, and C. Masquelier, "The existence of a temperature-driven solid solution in Li$_x$FePO$_4$ for 0 less than or equal to x less than or equal to 1," *Nature Materials*, vol. 4, pp. 254–260, 2005.

[191] "www.keithley.de."

[192] W. Dreyer, C. Guhlke, and R. Huth, "The behaviour of a many particle cathode in a lithium-ion battery," *WIAS preprint*, vol. 1423, 2009.

[193] T. Sasaki, Y. Ukyo, and P. Novak, "Memory effect in a lithium-ion battery," *Nature Materials*, vol. 12, pp. 569–575, 2012.

[194] A.M. Möller, *Study of the Mechanism of Lithium Insertion and Depletion in Lithium Iron Phosphate Thin Films.* PhD thesis, Justus-Liebig-Universität Gießen, 2014.

[195] G. Kobayashi, S.-I. Nishimura, M.-S. Park, R. Kanno, M. Yashima, T. Ida, and A. Yamada, "Isolation of Solid Solution Phases in Size-Controlled Li_xFePO_4 at Room Temperature," *Advanced Functional Materials*, vol. 19, pp. 395–403, 2009.

[196] C. Zhu, *Size Effects on Lithium Storage and Phase Transition in $LiFePO_4/FePO_4$ System.* PhD thesis, University of Stuttgart, 2013.

[197] J.C. Andrews, E. Almeida, M.C.H. van der Meulen, J.S. Alwood, C. Lee, Y. Liu, J. Chen, F. Meirer,M. Feser,J. Gelb,J. Rudati, A. Tkachuk, W. Yun, and P. Pianetta., "Nanoscale X-Ray Microscopic Imaging of Mammalian Mineralized Tissue," *Microscopy and Microanalysis*, vol. 16, pp. 327–336, 6 2010.

[198] N. Ohmer, B. Fenk, D. Samuelis, C.-C. Chen, J. Maier, M. Weigand, E. Goering, and G. Schütz, "Phase evolution in single-crystalline $LiFePO_4$ followed by in-situ scanning X-ray microscopy of a micrometer-sized battery," *Nature Communications*, vol. 6, no. 6045, 2015.

[199] "http://en.wikipedia.org/wiki/platinum."

[200] "http://en.wikipedia.org/wiki/aluminium."

[201] "www.mateck.de."

[202] K.-I. Horai, "Thermal Conductivity of Rock-Forming Minerals," *Journal of geophysical research*, vol. 76, no. 5, pp. 1278–1308, 1971.

[203] C. Wagner, "Beitrag zur Theorie des Anlaufvorgangs," *Zeitschrift für Physikalische Chemie, Abteilung B: Chemie der Elementarprozesse, Aufbau der Materie*, vol. B21, pp. 25–41, 1933.

[204] X.-F. Lei and J.-X. Ma, "Synthesis and electrochemical performance of aluminum based composites," *Journal of the Brazilian Chemical Society*, vol. 21, pp. 209–213, 00 2010.

[205] C.A.J. Fisher, V.M. Hart Prieto, and M.S. Islam, "Lithium Battery Materials LiMPO$_4$ (M = Mn, Fe, Co, and Ni): Insights into Defect Association, Transport Mechanisms, and Doping Behavior," *Chemistry of Materials*, vol. 20, no. 18, pp. 5907–5915, 2008.

[206] U. Boesenberg, F. Meirer, Y. Liu, A.K. Shukla, R. Dell'Anna, T. Tyliszczak, G. Chen, J.C. Andrews, T.J. Richardson, R. Kostecki, J. Cabana, "Mesoscale Phase Distribution in Single Particles of LiFePO$_4$ following Lithium Deintercalation," *Chemistry of Materials*, vol. 25, no. 9, pp. 1664–1672, 2013.

[207] S.S. Zhang, J.L. Allen, K. Xu, and T.R. Jow, "Optimization of reaction condition for solid-state synthesis of LiFePO$_4$-C composite cathodes," *Journal of Power Sources*, vol. 147, no. 1-2, pp. 234–240, 2005.

[208] N. Meethong, H.-Y.S. Huang, S.A. Speakman, W.C. Carter, and Y.-M. Chiang, "Strain Accommodation during Phase Transformations in Olivine-Based Cathodes as a Materials Selection Criterion for High-Power Rechargeable Batteries," *Advanced Functional Materials*, vol. 17, no. 7, pp. 1115–1123, 2007.

Acknowledgements

First, I would like to thank Prof. Dr. Joachim Maier for giving me all the freedom, resources and support one needs to conduct and independently work on a PhD thesis and for being, besides a great scientist, a sympathetic and humorous boss.

I am grateful to Prof. Dr. Guido Schmitz and Prof. Dr. Rainer Niewa for being on my examination committee and Sofia Weiglein for her administrative support and kindness.

I want to especially thank Dr. Dominik Samuelis for supervising me during my thesis, initiating collaborations with other groups, sharing his knowledge and motivation and giving me enough freedom and scientific advice to work on my own ideas, as well as for participating in beam times and sharing some self-made liquors during dinners.

Furthermore, I would like to thank all of my colleagues from the Maier department and members of both Max-Planck-Institutes in Stuttgart contributing to this work, of whom I will mention here only a few by name: Bernhard Fenk for his motivation and persistence in developing and building the micrometer-sized thin film batteries with me and especially for spending days, nights and weekends with me in front of the SEM/FIB. Chia-Chin Chen for growing LiF thin films for the micrometer-sized batteries and spending several nights together with me at the MAXYMUS beamline. Yvonne Link and Stephan Schmid for depositing thin aluminum anode layers for the micrometer-sized batteries. Dr. Chengtian Lin for growing the LFP single crystals and Anette Zechmeister for helping me to orient and cut them into useable pieces. Dr. Jelena Popovic for the synthesis of hydrothermally grown LFP powder. In addition, I want to thank Georg Christiani and Benjamin Stuhlhofer from the Technology Group for teaching me how to operate the PLD machines on my own and for support in maintaining the PLD systems. Gabriele Götz and Gerd Maier as well as Albrecht Meyer